HIGHWAY RESEARCH RECORD

Number 74

Soil Stresses

3 Reports

Foundation Settlement

1 Report

Caisson Stability

1 Report

Presented at the
43rd ANNUAL MEETING
January 13-17, 1964

HIGHWAY RESEARCH BOARD
of the
Division of Engineering and Industrial Research
National Academy of Sciences—
National Research Council
Washington, D. C.
1965

Department of Soils, Geology and Foundations

Eldon J. Yoder, Chairman
Joint Highway Research Project
Purdue University, Lafayette, Indiana

COMMITTEE ON STRESS DISTRIBUTION IN EARTH MASSES
(As of December 31, 1963)

H. Bolton Seed, Chairman
Department of Civil Engineering
University of California, Berkeley

Richard G. Ahlvin, Chief Engineer, Special Projects Section, Waterways Experiment Station, Vicksburg, Mississippi
E. S. Barber, Consulting Engineer, Soil Mechanics and Foundations, Arlington, Virginia
B. E. Colley, Portland Cement Association, Skokie, Illinois
Melvin T. Davisson, University of Illinois, Urbana
Lawrence A. DuBose, Testing Service Corporation, Lombard, Illinois
Austin H. Emery, Associate Soils Engineer, Bureau of Soil Mechanics, New York State Department of Public Works, Albany
Jacob Feld, Consulting Engineer, New York, New York
F. N. Finn, Technical Director, Products Engineering, Golden Bear Oil Company, Bakersfield, California
Hamilton Gray, Chairman, Department of Civil Engineering, Ohio State University, Columbus
Milton E. Harr, Associate Professor of Soil Mechanics, School of Civil Engineering, Purdue University, Lafayette, Indiana
R. G. Hennes, Department of Civil Engineering, University of Washington, Seattle
W. S. Housel, University of Michigan, Ann Arbor
T. F. McMahon, U. S. Bureau of Public Roads, Washington, D. C.
Robert L. McNeill, Supervisor, Soil Dynamics Shock Tube Laboratory, University Station, Alburquerque, New Mexico
Carl L. Monismith, University of California, Berkeley
J. O. Osterberg, Civil Engineering Department, Northwestern University, Evanston, Illinois
F. E. Richart, Jr., University of Michigan, Ann Arbor
Robert L. Schiffman, Soil Engineering Division, Massachusetts Institute of Technology, Cambridge
Werner E. Schmid, Assistant Professor, Department of Civil Engineering, Princeton University, Princeton, New Jersey
F. H. Scrivner, Pavement Research Engineer, Texas Transportation Institute, A & M College of Texas, College Station

Contents

Department of Materials and Construction

John H. Swanberg, Chairman
Chief Engineer, Minnesota Department of Highways, St. Paul

CONSTRUCTION DIVISION

R. L. Peyton, Chairman
Assistant State Highway Engineer
State Highway Commission of Kansas, Topeka

H. W. Humphres, Vice Chairman
Assistant Construction Engineer
Washington Department of Highways, Olympia

COMMITTEE ON CONSTRUCTION PRACTICES—STRUCTURES
(As of December 31, 1963)

K. R. Scurr, Chairman
Bridge Consultant, South Dakota Department of Highways, Pierre

Randle B. Alexander, American Concrete Pipe Association, Austin, Texas
Leo F. Beckett, Assistant to Chief Engineer, Missouri State Highway Commission, Jefferson City
H. B. Britton, Senior Structural Specifications Writer, New York State Department of Public Works, Albany
W. E. Crum, Bridge Design and Plans Engineer, South Carolina State Highway Department, Columbia
L. C. Dillard, Bridge Construction Engineer, North Carolina State Highway Commission, Raleigh
Eric L. Erickson, Chief, Bridge Division, Office of Engineering, U. S. Bureau of Public Roads, Washington, D. C.
Albert L. Grubb, Chief, Bureau of Bridges, Maryland State Roads Commission, Baltimore
John G. Hendrickson, Jr., Director of Engineering Research, American Concrete Pipe Association, Chicago, Illinois
John J. Hogan, Consulting Structural Engineer, Portland Cement Association, New York, New York
I. O. Jahlstrom, Bridge Engineer, Operations, California Division of Highways, Sacramento
Fred Kellam, Regional Bridge Engineer, U. S. Bureau of Public Roads, Chicago, Illinois
Norman L. Scott, Executive Secretary, Prestressed Concrete Institute, Chicago, Illinois
M. G. Spangler, Iowa State University, Ames
H. L. White, Chief Sales Engineer, Armco Drainage and Metal Products, Inc., Middletown, Ohio

Normal Stresses at the Tire-Soil Interface In Yielding Soils

D. R. FREITAG, A. J. GREEN and N. R. MURPHY, JR.
Respectively, Chief, Engineer, and Mathematician, Mobility Section, Mobility and Environmental Division, U. S. Army Engineer Waterways Experiment Station, CE, Vicksburg, Miss.

Small diaphragm-type pressure-sensitive cells were set flush with the outer surface of a smooth pneumatic tire. Tests were run to determine the magnitude and distribution of normal pressures at the tire-soil interface of a driven and a towed tire at several loads and inflation pressures.

Tests were conducted on both cohesive and noncohesive soils. The test soils were carefully prepared to a consistency that would allow the soil to yield under the applied load. In the tests reported, the different combinations of test variables produced ruts that ranged from a fraction of an inch to several inches in depth. Tire deflection measurements were made to determine the shape of the deformed tire and thereby to locate the position of the cells.

It was found that the pressure-distribution patterns that occur in the two soil types are different. Typical patterns are shown and some general relations between the patterns observed and the test variables are presented.

•THE U. S. Army Engineer Waterways Experiment Station at Vicksburg, Miss., is conducting systematic studies that will provide information on factors which influence vehicle mobility in deformable soils. The ultimate purpose of these studies is to develop rational means of designing military vehicles that will provide specified levels of performance in off-road conditions.

A study of the stresses at the interface of a moving pneumatic tire and the medium upon which it travels is one such study. Freitag and Green (1) gave results of a pilot study (conducted in the fall of 1961) to determine the distribution of stresses under pneumatic tires on an unyielding surface. Following this study, an extensive program was initiated to investigate and evaluate the factors that influence magnitude and distribution of the normal stresses between a pneumatic tire and deformable soils. While the objective of these studies is primarily military, the results will be applicable in many other fields. For instance, the development of knowledge pertaining to the stresses and strains or deformation at the tire-soil interface is important to the agricultural researcher who tries to minimize the compaction effect of pneumatic tires, and to the construction engineer who in many instances must depend on the kneading action of pneumatic tires to help compact a fill or subgrade material.

This paper describes the results of tests made to measure the distribution of stresses at the tire-soil interface under some representative test conditions. Two soils, a sand and a clay, carefully placed in a test pit, were used in the program. Each soil was tested at three different levels of strength. Only one tire at one test load was employed, but stresses were measured at several different inflation pressures. Tests were conducted with the wheel powered and with it towed.

Paper sponsored by Committee on Stress Distribution in Earth Masses.

TEST SOILS

Description

The sand used was a medium-to-fine sand, subangular in shape, poorly graded, and classified as SP according to the Unified Soil Classification System (USCS). The clay, taken from an alluvial deposit in the Vicksburg, Miss., area was classified as CH under the USCS. The gradation and classification data for both soils are shown in Figure 1.

Preparation

Sand. —The sand was placed in an open pit that had been lined with a waterproof membrane. This pit was approximately 4½ ft wide, 100 ft long, and 3½ ft deep.

After the pit was filled and subsequently after each test, the sand was loosened by tilling and then recompacted in place before the next test. Tilling was done with a simple multitooth scarifier that was pulled back and forth through the section until the sand was adequately loosened. The maximum depth of tillage possible with this equipment was 36 in. The actual depth of tillage and the amount of compaction necessary varied, depending on the soil strength desired and on the strength that had resulted from previous traffic on the section. The equipment used for tilling and compacting (scarifier and vibrator) was attached to the test carriage (described later) and towed at a uniform rate of speed (about 1.0 fps). The goal of the soil processing work was to obtain a test section in which the strength increased uniformly with depth and was consistent along the length of the test lane.

Cone index measurements were made to evaluate the effectiveness of the processing for each test. Cone index, an index of soil strength, is the force per unit area required to push a 30-deg right circular cone into the soil at a rate of 72 in. per min (2).

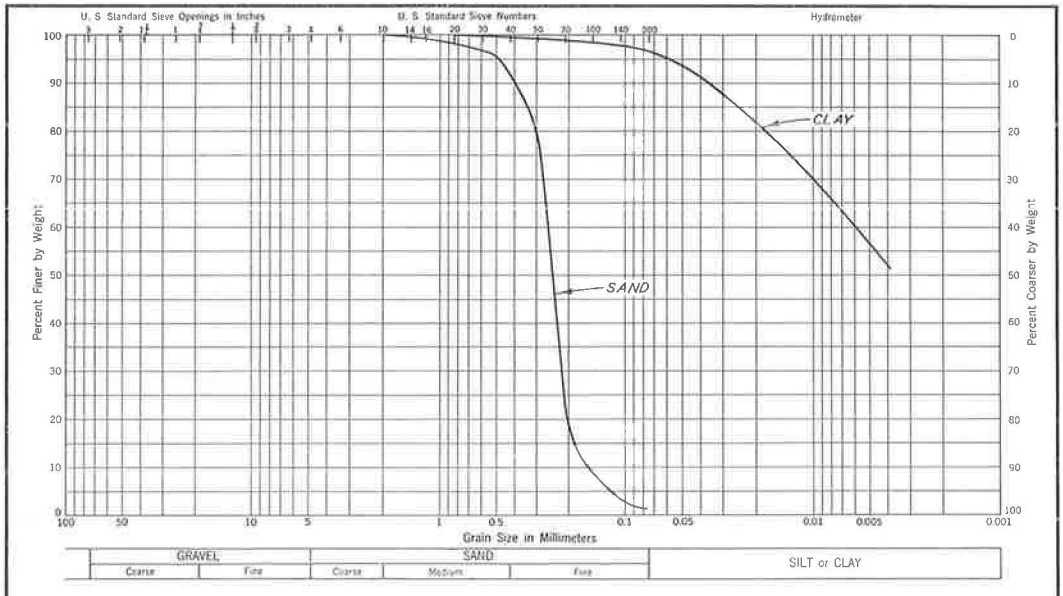

Number	Depth	Natural Moisture	L. L.	P. L.	P. I.	Classification	Density
						FINE SAND (SP)	MAX 106.1 LB/CU FT
							MIN 87.4 LB/CU FT
			64	22	42	HEAVY CLAY (CH)	

Figure 1. Gradation and classification data.

Clay. —A stockpile of natural clay was turned and worked until it had been air-dried to about 8 percent moisture content. The clay was then fed through a conveyor system that metered the soil into the hopper of a disintegrator. Here the lumps of soil were broken into smaller sizes and dropped into a roller crusher. The crusher broke the clods down to a maximum diameter of $\frac{1}{8}$ in. and fed them into a pug mill. A preselected quantity of water was metered into the pug mill and blended into the soil to provide uniform texture and the desired water content. The prepared soil issued continuously from the end of the pug mill and dropped into a truck. It was then transported to the test pit. The soil was dumped into the test pit in sufficient quantity to produce layers approximately 6 in. thick. Each layer was tilled with a pulvimixer and compacted by a pneumatic-tired roller. The compacted 6-in. layer was scarified to a depth of approximately $1\frac{1}{2}$ in. before the next soil layer was placed. The surface of each layer was moistened during construction to compensate for the loss in moisture due to evaporation. This procedure was continued until the top of the section was 1 to 2 in. above the desired grade. The excess material was then sliced off by a section of grader blade mounted on the test carriage, and the soil was allowed to "cure" for one or more days to insure a uniform moisture content throughout the section. In this case the goals of the soil processing were to obtain a strength profile that showed little or no increase in strength with depth, and to achieve a degree of saturation of 95 percent or greater in order to minimize the effects of traffic on soil strength.

Cone index measurements and moisture-density determinations were made to determine the effectiveness of the processing procedures. When a group of tests was conducted at a single soil strength, the fine-grained soil was reprocessed in place. This was done by backfilling the rut left by previous traffic, compacting the surface with pneumatic-tired and smooth-drum rollers, and then leveling the section. It was found that by sprinkling the surface of the section frequently and keeping it covered between actual test runs, the original strength of the material could be maintained for periods up to 60 days.

TEST APPARATUS

Test Carriage

Tests were conducted with a single-wheel test carriage that can accommodate wheels up to 56 in. in diameter and 26 in. in width. The carriage controls the path and alignment of the test wheel and is designed to isolate and measure the resultant horizontal and vertical forces and the torque at the wheel. Devices for determining degrees of tire rotation, forward travel of the carriage, and vertical movement of the hub of the test wheel are part of the system. Figure 2 is an overall view of this test carriage.

Instrumented Tire

Tire. —An 11.00-20, 12-ply rating, military tire from which all tread had been removed by buffing was used in this program. In buffing the tire, only the thickness of the lugs was removed so that the thickness and shape of the tire carcass were very nearly those of the original. Deflection gages were mounted inside the tire to determine changes in cross-sectional shape in the tire contact area. Stress cells, mounted in the tire so that their diaphragms were flush with the tire's outer surface, were used to measure normal stresses at the tire-soil interface during the operation.

Stress Cells. —Sever stress cells, 0.75 in. in diameter and 0.25 in. in height, were mounted in the face of the tire. On the basis of the type of construction (deflecting diaphragm) and the calibration procedures used, these cells are considered to measure stresses normal to their diaphragms. A protective steel cup around the cell prevents the tire from exerting pressure on the cell's sidewall, as such a pressure would cause the diaphragm to deflect and thus invalidate the pressure cell measurements. The walls and bottom of the cup are $\frac{1}{16}$ in. thick, and the inside radius of the cup is $\frac{1}{32}$ in. larger than that of the cell. A semiconductor strain gage constitutes the pressure-sensitive element of each cell, and resistors are used to complete a full Wheatstone bridge circuit. Figure 3 illustrates graphically the electrical circuit from the pressure cell to

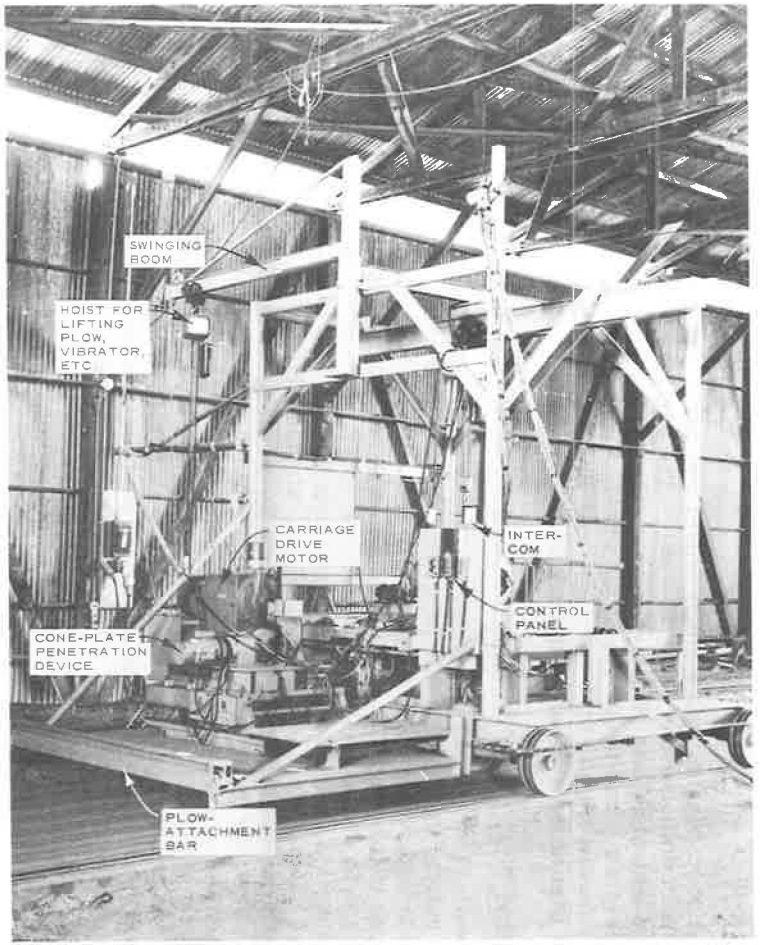

Figure 2. Rear view of large test rig.

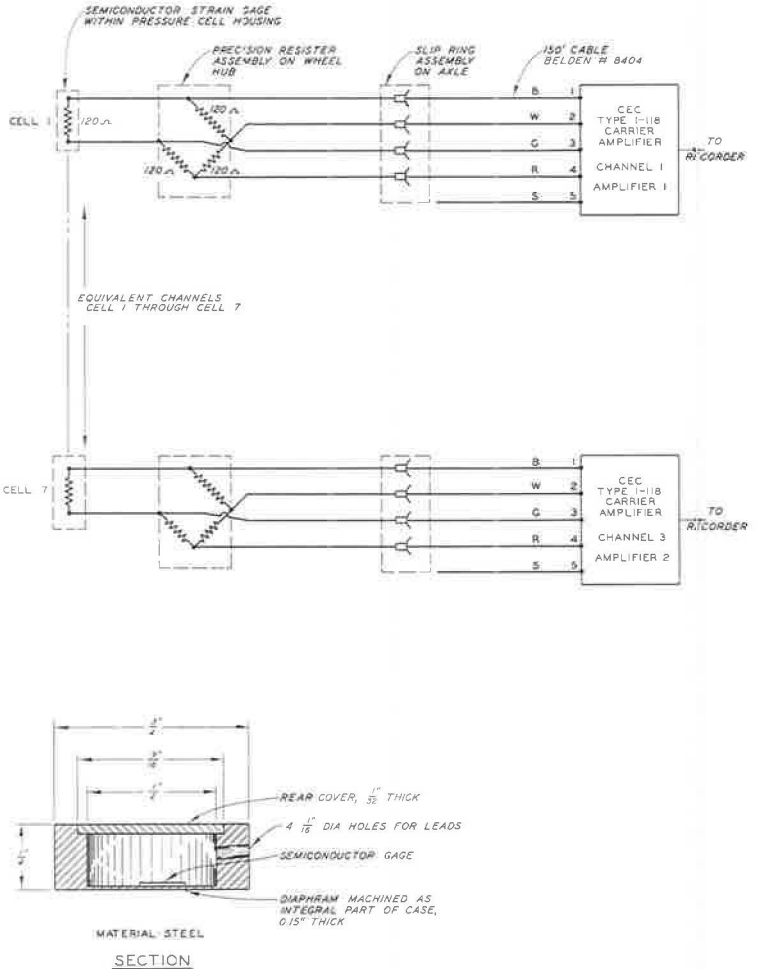

Figure 3. Electrical schematic drawing of WES pressure cell amplifier.

the recorder. The use of semiconductors permits the construction of a more durable gage, becuase they are much more sensitive than ordinary foil strain gages.

Seven holes, each large enough to accommodate a cell and cup as described in the preceding paragraph, were cut in the outer surface of the tire, and slits were cut leading from the holes to accommodate the conductor wires of each cell. The seven cells were installed along a diagonal line across the face of the tire (Fig. 4) to avoid serious weakening of the tire in the single cross-sectional plane. The total depth of the cell and cup was approximately equal to the thickness of the rubber over the outermost layer of cord, and for this reason extreme care had to be taken when cutting the tire to avoid damage to the cords. The bottom of the cup was bonded to the tire with a latex-adhesive. The area between the outer walls of the cup and the tire was backfilled with a pliable rubber-base compound that did not adhere to the tire or the cup. The cell was fastened to the cup with a thin layer of bituminous

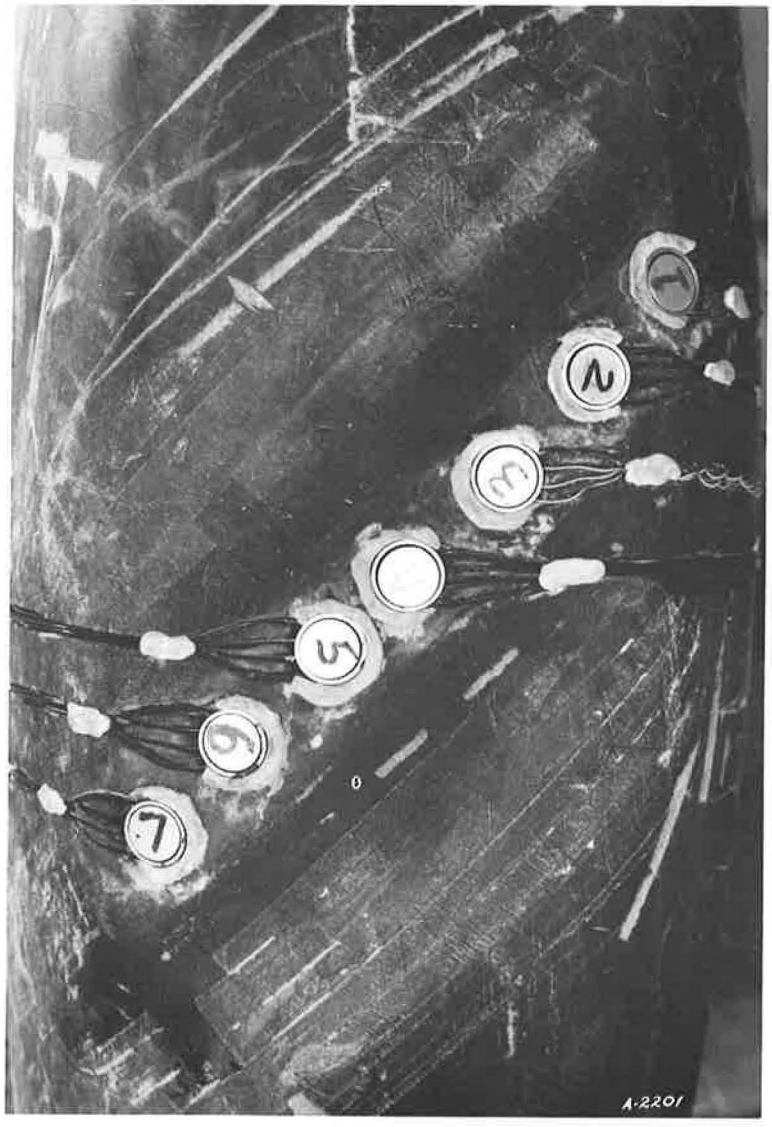

Figure 4. Cells in the tire carcass.

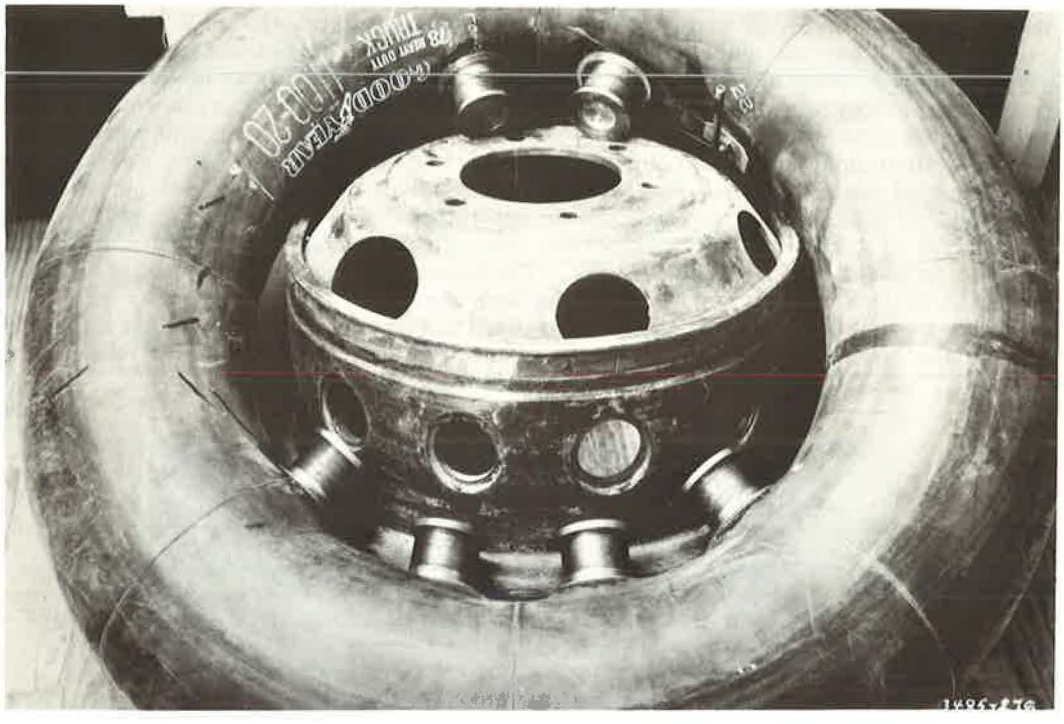

Figure 5. Deflection gage ports in 11.00-20 tube.

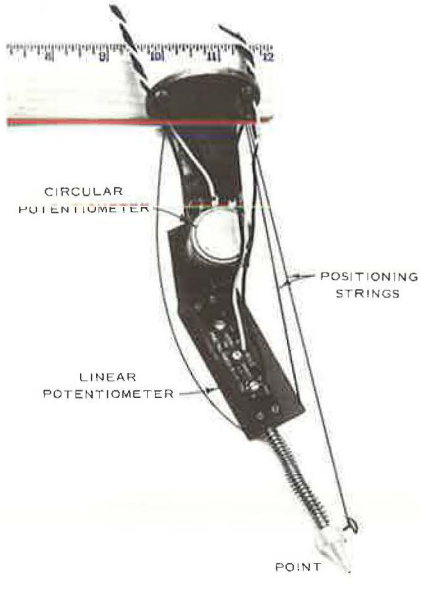

Figure 6. Deflection gage.

adhesive so that the cell would stay in place during traffic, but could be easily removed for calibration or repair. A strip of thin rubber membrane was used to cover the entire cell area to prevent damage to the diaphragm of the cell and to prevent sand from getting in the area between the cup and the wall of the cell. The membrane was fastened to the tire with a thin plastic adhesive tape that could deform as the tire carcass did without providing additional strength to the tire carcass.

Deflection Gages. —Commercially available linear and circular potentiometers were used to measure deflections inside the tire. A linear and a circular potentiometer were combined to make one gage and inserted through a port in the rim and tube (Fig. 5). A pointed brass tip attached to the end of the potentiometer shaft was held firmly against a point inside the tire by a spring. Movements of this point in line with the potentiometer shaft and in an arc around the center of rotation of the circular potentiometer were recorded. Five gages were employed, each positioned to record movements at a different point on the left-hand side of the tire. Because it was not physically possible to place more than one gage in the same cross-

section, they were placed in separate cross-sections normal to the plane of rotation of the tire. The gages were rotated to the desired angular position while outside the tire, and the circuit that included the circular potentiometer was balanced at that position. The gage was then placed in the port, and the base was tightened in position. After this had been done, the positioning strings (Fig. 6) were used to rotate the gage until the circular potentiometer circuit for that gage was rebalanced, indicating that the gage was in the desired position.

TEST CONDITIONS

Both towed- and powered-wheel tests have been conducted in sand, but to date only towed tests have been conducted in clay. Various combinations of load, inflation pressure, and soil strength were studied in the towed tests; during the powered-wheel tests, slip also was a controlled variable.

METHODS USED IN ANALYSIS OF TEST RESULTS

Data Reduction

In the form in which they are first obtained, the data are merely simultaneous records of the measurements. At each instant of time, data are recorded that describe the angular position of a stress cell relative to the wheel axle, the position of the cell or the deflected tire, the vertical movement of the wheel axle, and the registration of the stress cell. All these data must be considered simultaneously to arrive at the proper value of a stress at a given point on the tire-soil interface.

In the reduction of the test data for this study, the shape of the deflected tire cross-section was determined at 5-deg intervals of rotation. The positions of the stress cells were then located on each cross-section. From these plots the circumferential position for each cell was determined. Each of the cell registrations, which represent the stress variation over the length of the tire contact area at a particular distance from the center line of the tire, was then properly oriented relative to the deflected tire. These registrations were readily converted to stresses by means of the cell calibrations, and as such, when projected on a horizontal plane, represented longitudinal sections of the total

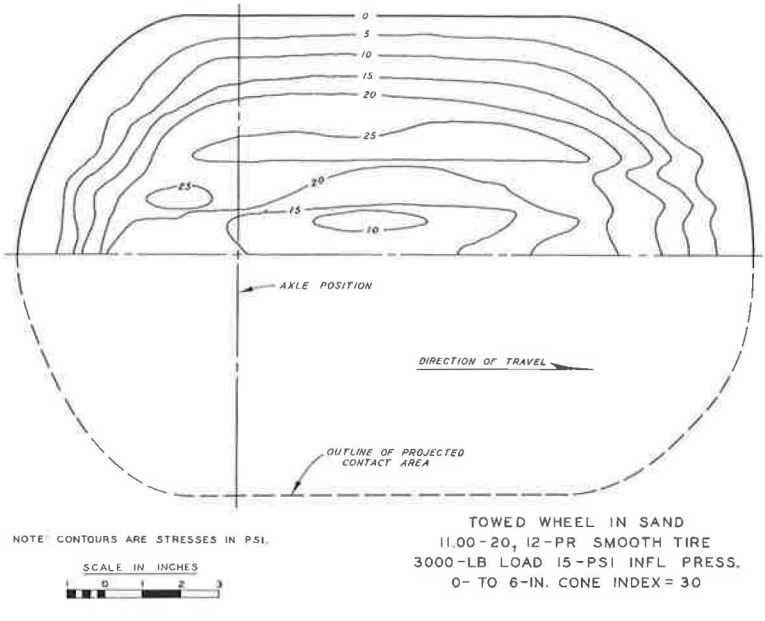

Figure 7. Distribution of normal stresses projected on horizontal plane.

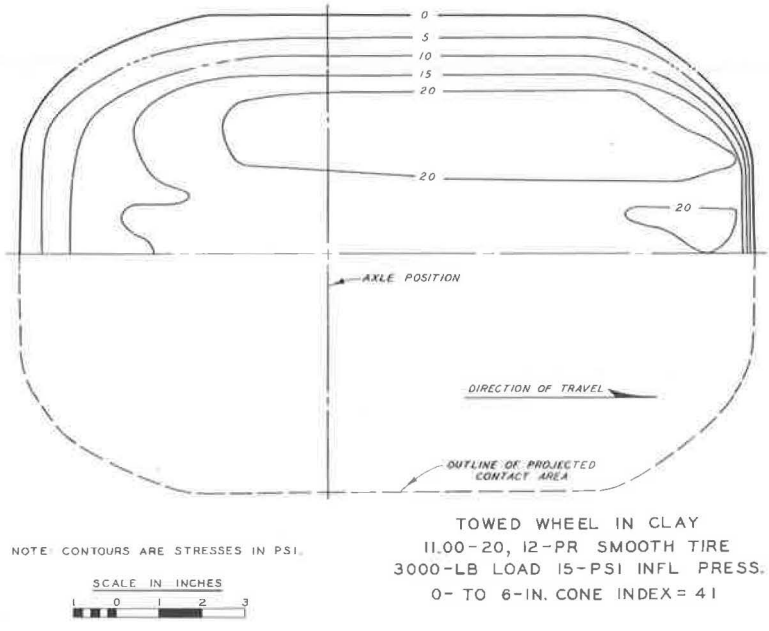

Figure 8. Distribution of normal stresses projected on horizontal plane.

stress pattern. From the longitudinal sections and the recorded distance that each cell was offset from the center line of the tire, a plan of the dynamic tire-contact patch was drawn and on it a map of equal stress lines was constructed.

Stress-Distribution Maps

Figures 7 and 8 show typical stress maps developed from the test data. These maps show measured normal stresses on the projection of the three-dimensional curved interface on a horizontal plane. Because the stress cells are considered to register pressures normal to their surface, the components are obtained by locating the cell positions on the appropriate projection and plotting the accompanying stress magnitude at that point. The maps in Figures 7 and 8 show the distribution of interface stresses beneath the 11.00-20 tire with a 3,000-lb wheel load at an inflation pressure of 15 psi in soft sand and in clay, respectively.

The average cone index in the top 6 in. was greater for the clay. The clay had a cohesive strength of 3.3 psi and its friction angle was 0. The sand at a cone index of 30 had a friction angle of approximately 31 deg and was essentially cohesionless. An effort was made to select a pair of tests in which the maximum "in-soil" deflection was of the same order of magnitude, because this would reflect about equal resistance to displacement and the extent of tire distortion would be about the same in each test. It can be seen that the stresses were most uniformly distributed in the clay, and the high stress zone near the edge of the contact area was not as pronounced as in the sand. The projected contact area was smaller for the clay, indicating that average contact pressure was greater.

Resolution of Resultant Forces

To resolve the normal stresses acting at the tire-soil interface into a single resultant force, the stresses registered by each cell are first plotted normal to a circumference of the deflected tire—the circumference taken at the same offset from the center line of the cross-section of the tire as the cell registering the stresses. Figure 9 is an example of such a plot, showing in this case the circumference of the deflected tire at

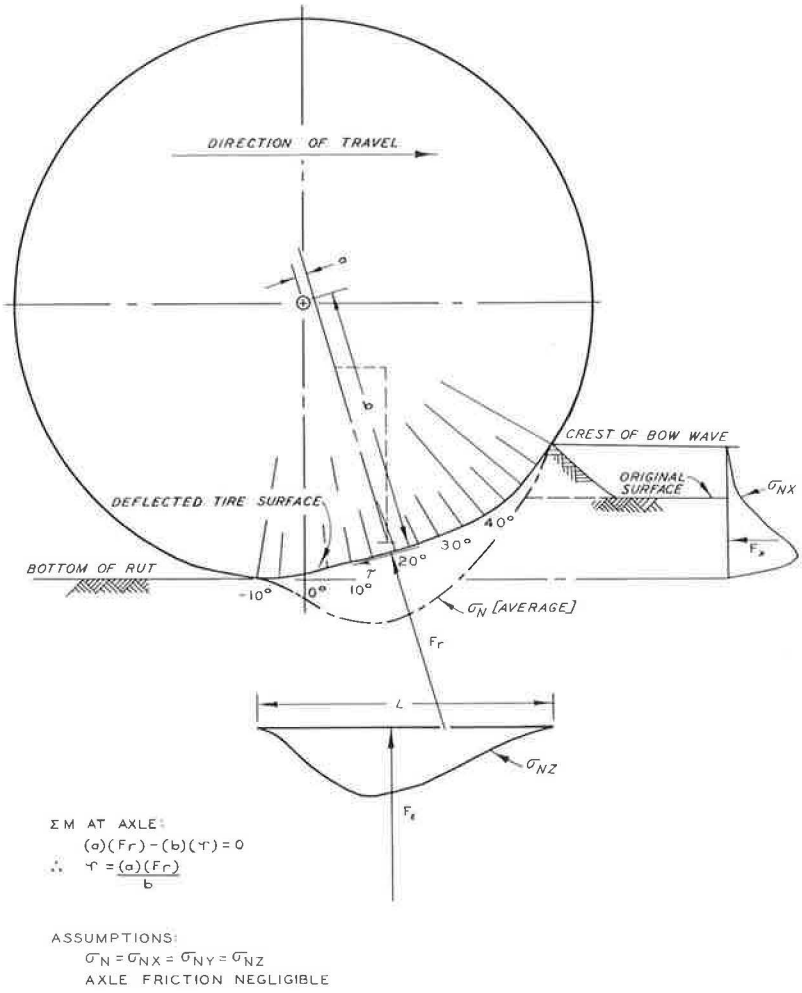

Figure 9. Normal and tangential forces on a towed pneumatic tire in soft soils.

the center line of the cross-section of the tire. The normal stresses registered by a cell at the center line of the tire have been plotted normal to the deflected surface and projected into vertical and horizontal planes. By assuming that the stresses at each point are uniform over some narrow strip whose width is determined by the lateral spacing between the cells, the magnitude and locations of the resultants of the vertical and horizontal components of the normal forces on each strip can be computed. Once this has been done, the magnitudes and the locations of the resultant of the horizontal and vertical components of all the measured normal stresses can be determined and these can be resolved into a single resultant if desired; i. e., the resultant of the normal stresses.

The general validity of the stress cell data and of this approach can be demonstrated to a certain degree for towed tests by comparing the measured horizontal and vertical forces to the computed values. This comparison is good (Table 1).

The computation using the data gathered in this program indicates that the resultant of all the normal stresses at the tire-soil interface appears to intersect the center of the axle for both towed and powered tests. Of 25 towed tests and 7 powered tests analyzed, the resultant normal force always passed within 0.5 in. of the axle center line. In only six instances was the distance (a, Fig. 9) more than 0.2 in. In all cases where

TABLE 1

COMPARISON OF COMPUTED AND MEASURED FORCES

Average 0- to 6-In. Cone Index	Inflation Pressure (psi)	Applied Wheel Load (lb)	Measured Towing Force (lb)	Computed	
				Wheel Load (lb)	Towing Force (lb)
(a) Sand					
16	15	3,000	870	2,950	862
15	30	3,000	1,028	2,961	1,098
16	60	3,000	1,115	2,914	1,142
24	15	3,000	760	3,230	703
30	15	3,000	609	3,104	563
27	60	3,000	1,000	3,032	1,124
57	15	3,000	166	3,130	187
54	60	3,000	943	3,147	1,083
(b) Clay					
41	15	3,000	405	3,028	412
47	30	3,000	712	3,260	765
45	60	3,000	755	3,323	797
28	15	3,000	1,020	2,990	1,220
29	30	3,000	1,135	2,986	1,365
28	60	3,000	1,180	2,980	1,208

the resultant, F_r did not intersect the center of the axle, it passed forward of the center line of the axle.

If the resultant of the normal force passes through the axle, it creates no moment about the axle. This suggests that the resultant of the tangential stress must be zero, or very nearly so, for a towed test. However, negative slip is known to occur in a towed test (i.e., the wheel skids slightly), and slip must be accompanied by some tangential forces. Therefore, a tangential force acting in the direction opposite to the slip-induced force must be set up at the interface. Apparently this counterbalancing force is produced by the formation of a bow wave of soil in front of the wheel. By the same token it appears that in powered-wheel tests the resultant of the tangential stresses is directly related to the torque input and the deflected radius of the tire.

Stress Patterns

To give some indication of the distribution of stresses at the tire-soil interface without showing complete stress maps, the stresses measured by a cell at the center line of the tire's cross-section and a cell at an offset of 3.75 in. are shown in Figures 10 through 15. The drawings of the deflected tire and the location of the soil surfaces shown in these figures refer only to the center line of the tire.

RESULTS OF TESTS IN SAND

Towed Tire

Analysis of the results of the towed tire tests in sand indicated that the general shape of the stress patterns tends to be different for each of the three different tire deflections studied. The drawings in Figure 10 are intended to illustrate the three different general types of stress-distribution patterns that could be distinguished in these tests.

The stress patterns shown in plot a of Figure 10 are typical of those from tests in which the in-soil tire deflection was small, usually less than 10 percent. These patterns are identified by the single-peaked curves, both at the center line and at the offset. Tests in which the in-soil tire deflection was greater than about 20 percent usually produced curves of the type shown in plot c of Figure 10. For these tests, the center-line cell always exhibited two maxima in the stress wave, and the cell at the 3.75-in. offset

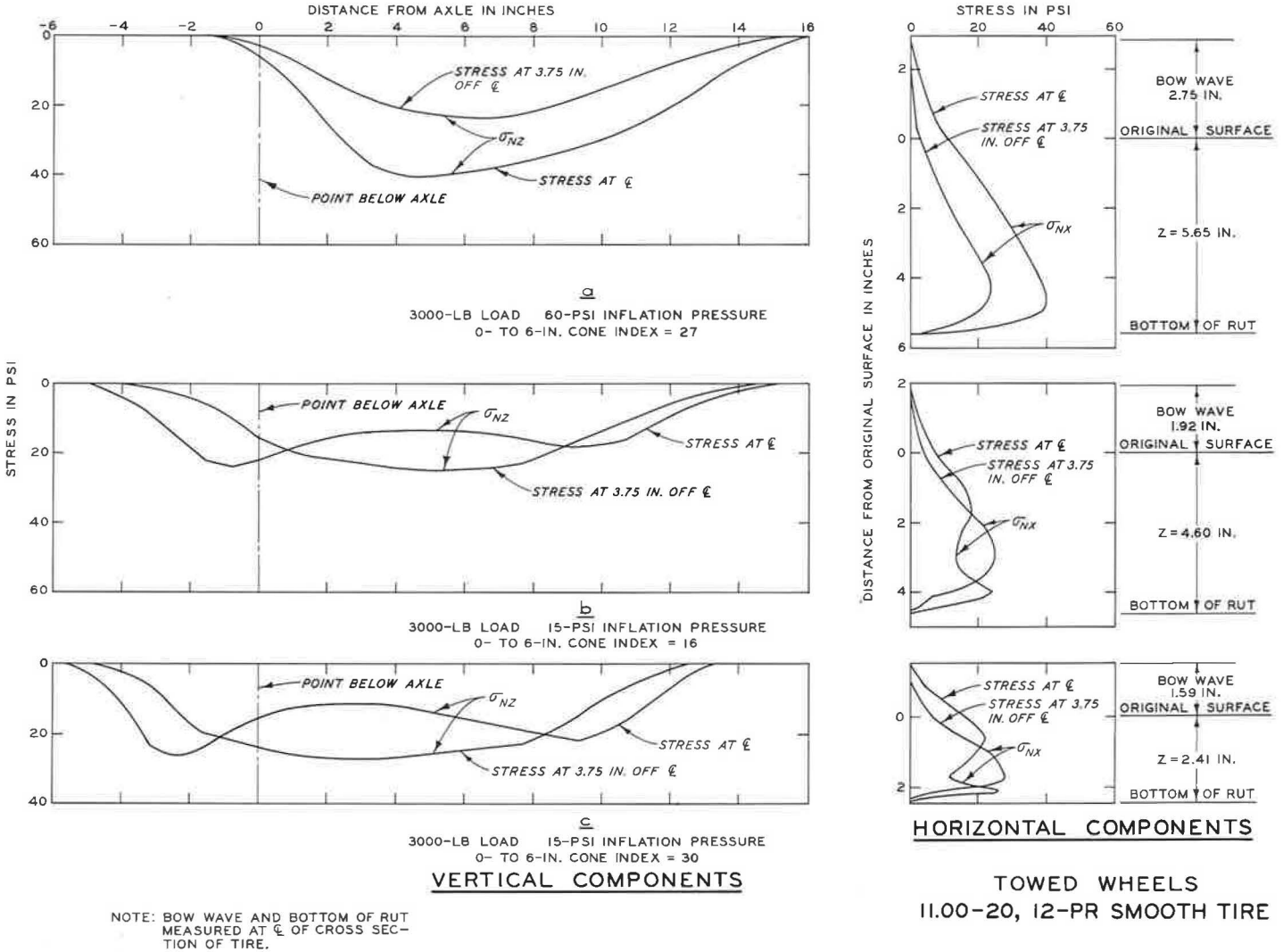

NOTE: BOW WAVE AND BOTTOM OF RUT MEASURED AT ℄ OF CROSS SECTION OF TIRE.

Figure 10. Normal stresses at tire surface in sand.

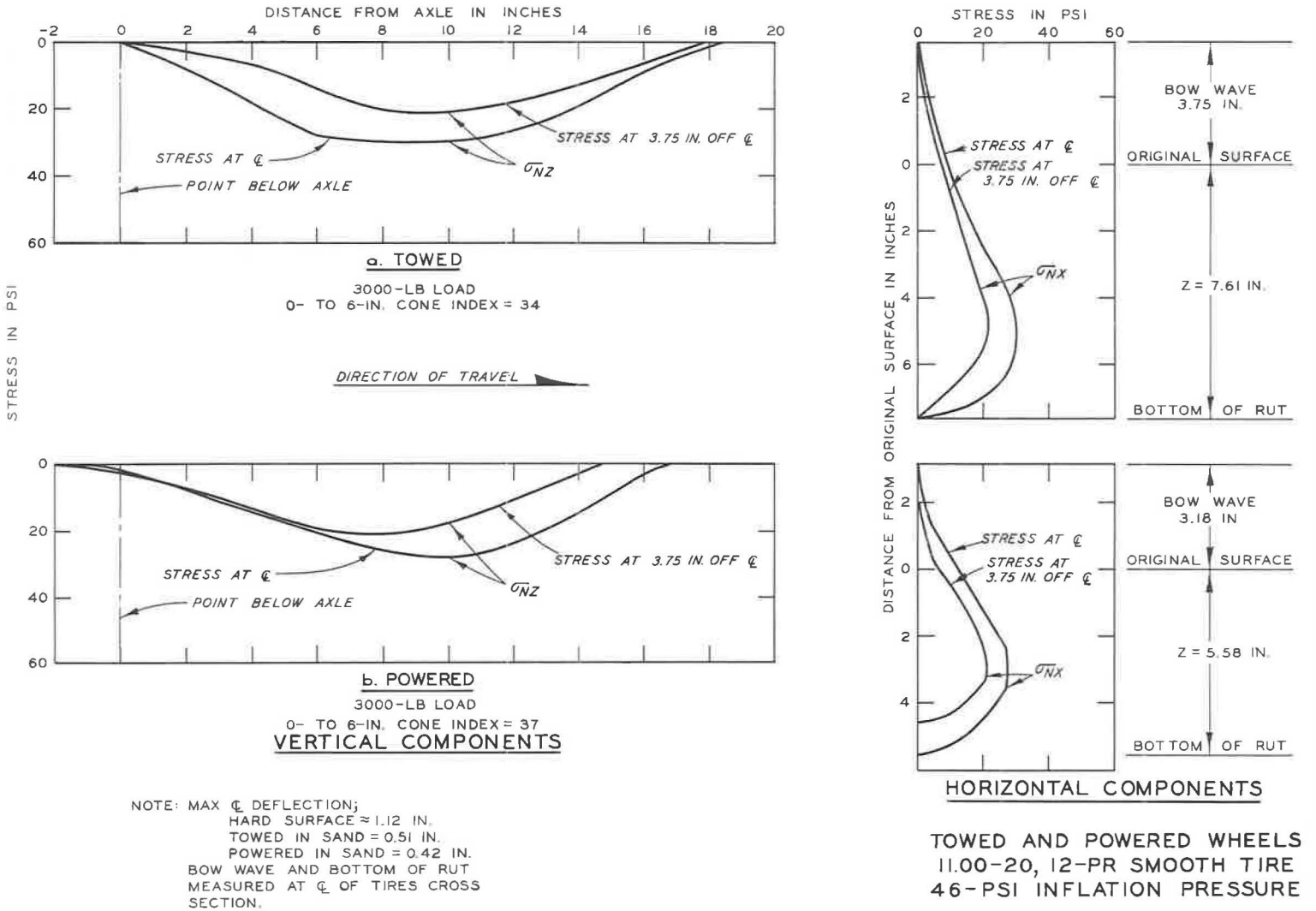

NOTE: MAX ℄ DEFLECTION;
HARD SURFACE ≈ 1.12 IN.
TOWED IN SAND = 0.51 IN.
POWERED IN SAND = 0.42 IN.
BOW WAVE AND BOTTOM OF RUT MEASURED AT ℄ OF TIRES CROSS SECTION.

TOWED AND POWERED WHEELS
11.00-20, 12-PR SMOOTH TIRE
46-PSI INFLATION PRESSURE

Figure 11. Normal stresses at tire surface in sand.

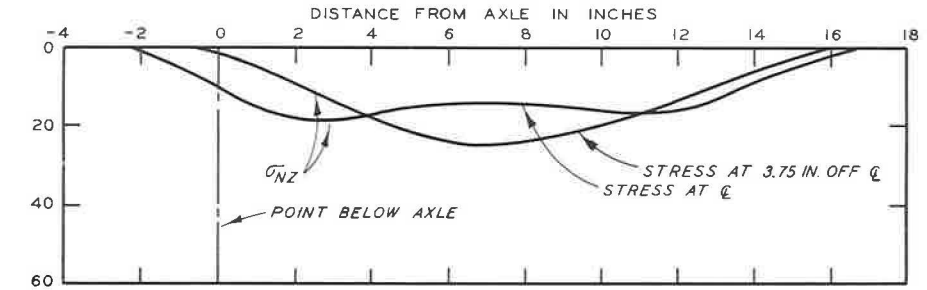

a. TOWED

3000-LB LOAD
0- TO 6-IN. CONE INDEX = 34

DIRECTION OF TRAVEL

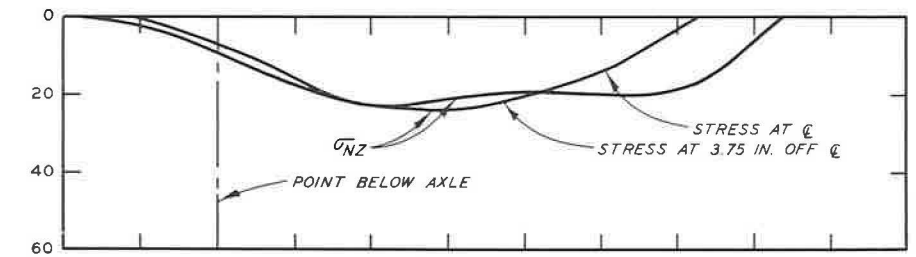

b. POWERED

3000-LB LOAD
0- TO 6-IN. CONE INDEX = 36

VERTICAL COMPONENTS

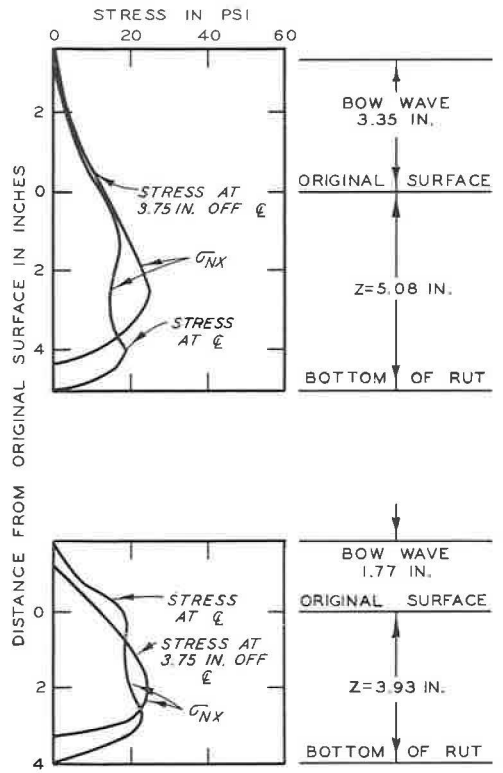

HORIZONTAL COMPONENTS

TOWED AND POWERED WHEELS
11.00-20, 12-PR SMOOTH TIRE
19-PSI INFLATION PRESSURE

NOTE: MAX ℄ DEFLECTION:
HARD SURFACE ≈ 2.1 IN.
TOWED IN SAND = 1.48 IN.
POWERED IN SAND = 1.42 IN.
BOW WAVE AND BOTTOM OF RUT MEASURED AT ℄ OF TIRES CROSS SECTION

Figure 12. Normal stresses at tire surface in sand.

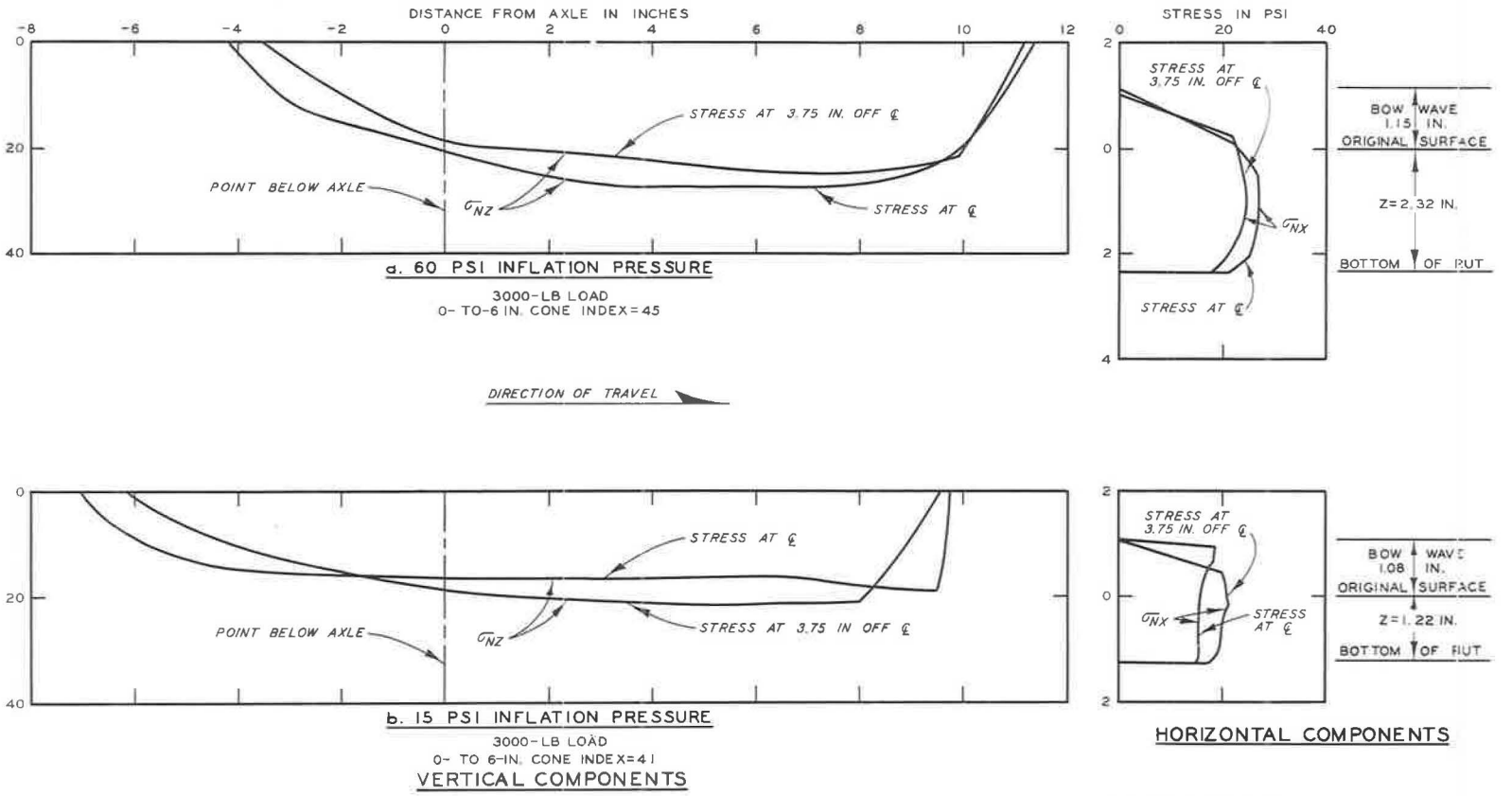

Figure 13. Normal stresses at tire surface in clay.

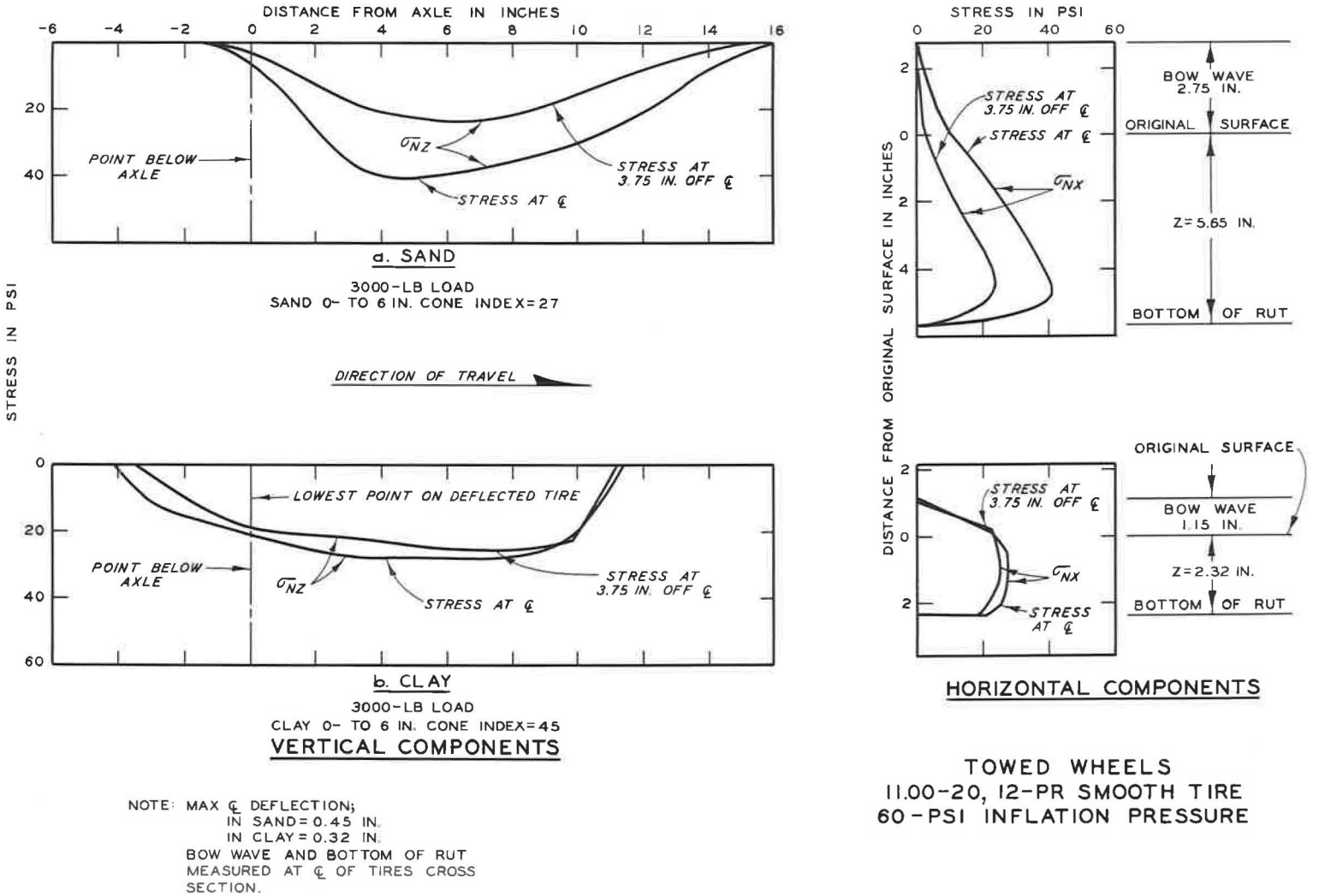

Figure 14. Normal stresses at tire surface in sand and clay.

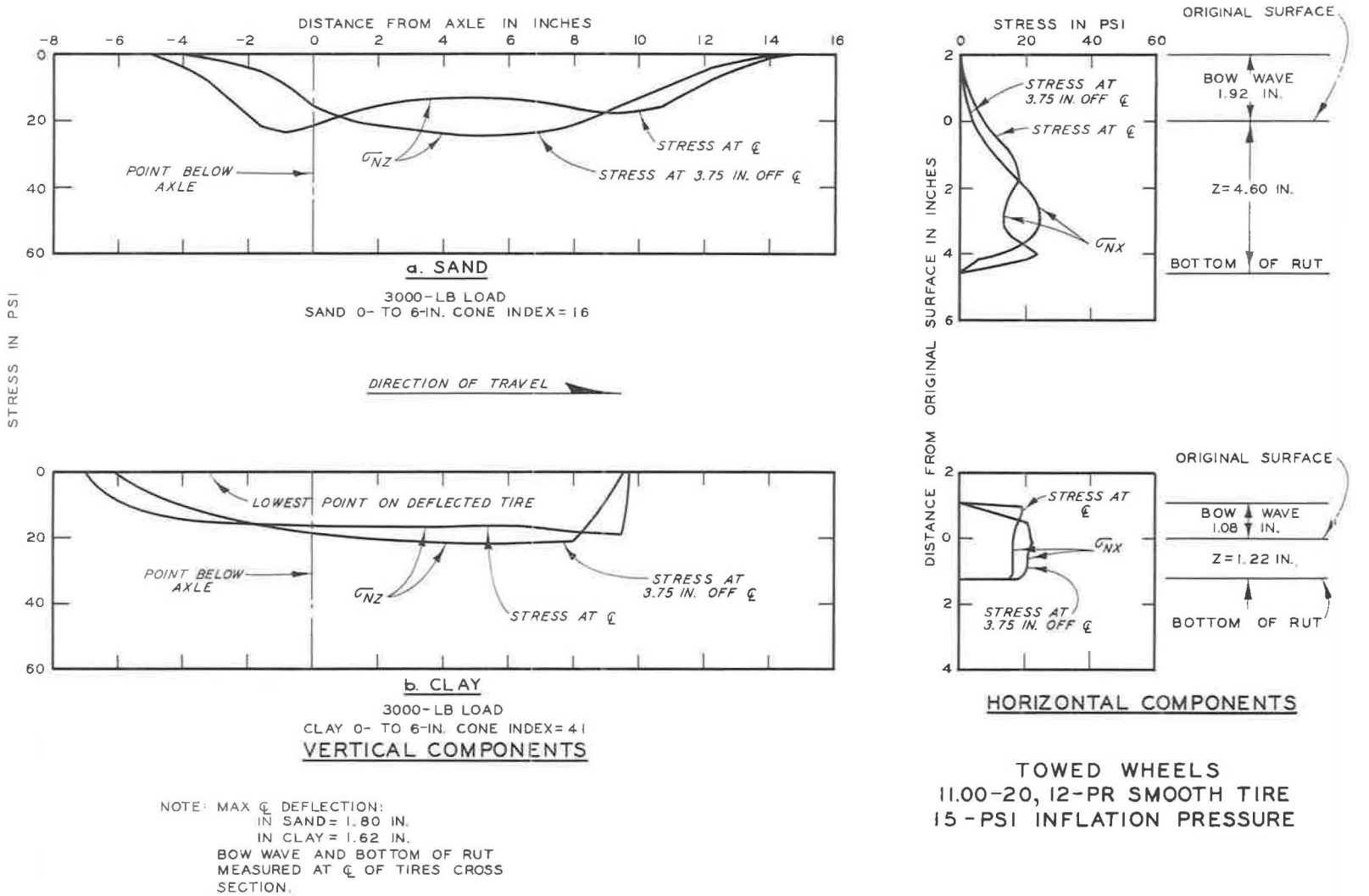

NOTE: MAX ℄ DEFLECTION:
IN SAND = 1.80 IN.
IN CLAY = 1.62 IN.
BOW WAVE AND BOTTOM OF RUT MEASURED AT ℄ OF TIRES CROSS SECTION.

Figure 15. Normal stresses at tire surface in sand and clay.

produced single-peaked stress waves. The third pattern, shown in plot b of Figure 10, represents the intermediate case between the two just described. The tire deflection usually is between about 10 and 20 percent. The center-line cells and the offset cells tend to show a relatively constant stress for a significant portion of the stress wave; and if the curves produced by all cells are averaged, the average stress at any cross-section is about the same for the major portion of the contact length.

Towed- Versus Powered-Wheel Tests

Figures 11 and 12 display comparisons of results of towed- and powered-wheel tests in sand showing the distribution of stresses on the horizontal and vertical projections of the contact areas. The wheel load was 3,000 lb, and inflation pressures were adjusted to produce hard-surface deflections (percent reduction in carcass section height) of 15 and 25 percent, respectively.

In both figures certain observations can be made. The towed wheel produced a deeper rut than the powered wheel under similar conditions of load, deflection, and soil. Stresses produced by the bow wave were greater during the powered tests, and although the exact positions are not shown, it is apparent that the centroid of the vertical component of the normal stresses was a greater distance forward of the axle during the powered tests. Although the stress patterns are somewhat different, the general appearance is the same for towed and powered tests at similar conditions and the peak stress values are of the same order of magnitude. In each pair of tests, the maximum center-line deflection is slightly greater for the towed tire.

RESULTS OF TOWED-WHEEL TESTS IN CLAY

Results of tests at a wheel load of 3,000 lb and inflation pressures of 60 and 15 psi are represented in Figure 13. This figure shows the distribution of stresses on the horizontal and vertical projections of the contact area. This particular pair of tests was chosen to illustrate the fact that the stresses remain uniformly distributed for a wide range of deflections. Maximum center-line deflection during the 60-psi test was approximately 3.5 percent, and during the 15-psi test it was approximately 18 percent. The stresses in the center portion of the contact area were higher than those at the offset position during the 60-psi test; the reverse was true during the 15-psi test. Apparently, in this soft, cohesive material a plastic flow condition develops in the soil beneath the tire and thus reduces the possibility that zones of higher stresses may develop at the tire-soil interface as they do during tests in sand.

A COMPARISON OF TOWED TESTS IN SAND AND CLAY

In Figures 14 and 15, the distribution of the components of the normal stresses on the horizontal and vertical projections of the contact areas is shown. The wheel load was 3,000 lb and the inflation pressures were 60 and 15 psi, respectively. To make this comparison, pairs of tests were chosen in which the maximum in-soil deflection was of the same order of magnitude. As previously mentioned, this indicates that the total resistance to displacement and the extent of the tire distortion were about the same in both the sand and the clay tests.

In both figures the following points are obvious: (a) The interface stresses are more evenly distributed during the tests in clay, and the peak stress values recorded are slightly less than those recorded for the tests in sand. (b) At the front of the contact areas, the stresses increase in magnitude at a faster rate during the clay tests, probably because the bow wave in a cohesive material remains an integral part of the soil mass, having about the same cohesive strength as the mass itself, even though it is being deformed, whereas the bow wave in sand is a disturbed material in a very loose condition. (c) The contact lengths and sinkages are larger for the tests conducted in sand when the maximum deflection of the tire in sand and in clay is of the same order of magnitude.

The position of the lowest point on the deflected tire is indicated in Figures 14 and 15. It is seen that rebound of the clay soil produces normal stresses to the rear of the

lowest point on the deflected circumference, which always fell at, or beyond, a point directly beneath the axle. The approximate amount of rebound estimated from the tire-deflection plot for the two tests shown in 0.2 in.

CONCLUSIONS

On the basis of the data presented in this paper, conclusions are as follows:

1. The line of the resultant of the normal stresses at the tire-soil interface passes through the center line of the wheel axle for towed and powered wheels.
2. In sand, the shape of the stress-distribution pattern is related to the magnitude of the maximum in-soil deflection of the moving tire as measured at the center line of the tire cross-section.
3. Interface stresses are more evenly distributed when the tire is operating in a soft clay soil than when it is operating in sand; i.e., zone of higher stresses is not as pronounced and the peak stress values reached are slightly less than those recorded during a sand test.

REFERENCES

1. D. R. Freitag and A. J. Green. Distribution of Stresses on an Unyielding Surface Beneath Pneumatic Tires. Highway Research Board Bull. 342, pp. 14-23, 1962.
2. U. S. Army Engineer Waterways Experiment Station, CE, Trafficability of Soils, A Summary of Trafficability Studies Through 1955. Tech. Memo. 3240, 14th Suppl., Vicksburg, Miss., Dec. 1956.

An Experimental Study of Lateral Pressures on Abutment Retaining Walls

O. D. RICHARD and D. A. LINGER
Respectively, Valparaiso University and The University of Arizona

This paper presents the results of an experimental study of the lateral pressures transmitted through the soil to an abutment retaining wall. The lateral pressures were the result of concentrated surface wheel loads and were measured in the soil backfill and at the soil-structure interface.

The first portion of the study was an evaluation of the effect of variations in the type of soil used in the backfill on the pressure distribution. This was accomplished by using two different types of soil: well-graded granular soil with considerable fines, and a uniformly graded medium sand. The results show the variation in pressure attributed to the difference in soil characteristics.

The second portion of the study was an evaluation of the effect of the relative rigidity of an abutment retaining wall on the magnitude and distribution of soil pressure. For this study two types of abutment retaining walls were used and compared.

In each phase of the investigation, the resulting experimental pressures are compared with the theoretical Boussinesq solution of lateral pressures transmitted through an elastic, homogeneous, isotropic, semi-infinite media. The results indicate that the pressures at the soil-wall interface are larger than the pressures measured in the soil. This increase in pressure is due to the discontinuity in the soil mass resulting from presence of the abutment retaining wall. The results also indicate the effect of flexibility of the wall on the lateral pressure at the soil-wall interface.

•THE PROBLEM investigated concerns the transmittal of lateral pressure through a soil backfill to an abutment retaining wall structure. The lateral pressure was the result of a concentrated wheel load on the surface of the backfill material.

M. G. Spangler (8) in 1938 reported one of the first experimental results concerning this problem. The objective of his study was to determine the magnitude and distribution of lateral forces transmitted to a retaining wall through a gravel backfill by a concentrated wheel load applied on the backfill surface. He found the measured pressures were distributed in accordance with the Boussinesq theory of distribution of pressures through an elastic medium due to a concentrated load. The magnitudes of the pressures were two to three times as great as those calculated by the Boussinesq equations. In his investigations, one type of soil was used with one type of wall construction. Deflection of the wall was not investigated.

L. White and G. Paaswell (14) in 1939 discussed the application of the Boussinesq equation for soils from a theoretical viewpoint. It was generally agreed that the Boussinesq equation would be a closer approximation than the usual rule of thumb. This rule utilizes an additional depth of backfill in the calculations of lateral pressure due to surcharge loads. Their findings, as well as the experimental evidence of Spangler, showed that the intensity of pressure due to a surface load is maximum near the surface and diminishes rapidly in intensity with depth. This observation is quite in contradiction to the usual method of analyzing surcharge loads.

Paper sponsored by Committee on Stress Distribution in Earth Masses.

W. Weiskopf (13) in 1945 proposed a theory concerning the pressure created against a rigid wall. His theory assumed that an imaginary load P′ would induce a lateral pressure against the vertical plane. This value would be equal to the lateral pressure exerted by the actual load P on that plane in the unrestrained soil mass, and would combine with this load. Therefore, the actual pressure, which would be measured at the wall, would be double the lateral pressure exerted by the actual load.

Relatively little work has been done with the problem of lateral pressure created by surcharge loads. There is little evidence, in the literature, of work presently being done on the subjects of comparison of pressures created with different soils, and the effect of the movement of the retaining wall under pressure.

The first objective of the investigation was to determine the variation of lateral pressure distribution resulting from different types of soil under wheel loads. The second objective was the comparison of pressure distribution due to the relative rigidity of the wall construction.

To accomplish these objectives, a special test abutment was constructed incorporating the essential study features which were the walls of the abutment. One wall of the abutment was relatively flexible, whereas the other was rigid. A number of pressure sensing devices were placed in the backfill and the backfaces of the walls. These pressure sensing elements provided measurement of lateral pressure in the soil mass and on the walls.

In the investigation of variation of pressures due to different soil types, the main problem was to study the pressure bulbs created. The objective was to determine if the soil characteristics would have any influence on the pressure bulbs developed. To obtain a complete picture of the pressures created, the pressures were measured both in the soil away from the wall and at the soil-wall interface. The two soils used were different in their gradation characteristics.

The pressure bulbs created for both soils were compared with the theoretical Boussinesq solution for pressure distribution. The comparisons were made both in the horizontal and vertical planes thus illustrating the complete pressure bulb as it was developed throughout the soil to the wall.

The second objective was to determine the effect of wall movement on pressure created. The slab of the abutment was on rollers at the flexible wall which allowed the wall to deflect when pressure was applied. The wall deflections were measured as well as the applied pressures both at the flexible wall and at the rigid wall. These pressures were also compared with the theoretical Boussinesq solution.

THEORY OF LATERAL PRESSURE

Application of Elastic Theory

In 1885, J. Boussinesq derived equations for the stresses on a boundary of a semi-infinite body using the theory of elasticity. Boussinesq's stress distribution theory was for the simplest case of loading of a solid which was considered to be a homogeneous, elastic, isotropic, semi-infinite medium. This would be the case of a single, vertical, concentrated load applied at a point on the horizontal surface.

The application of a concentrated load on the ground surface would result in a lateral stress distribution as shown in Figure 1. The equation for lateral stress derived by Boussinesq is as follows:

$$\sigma_X = \frac{P}{2\pi}\left[\frac{3X^2Z}{R^5} - (1 - 2\mu)\left(\frac{X^2 - Y^2}{R^2r^2(R + Z)} + \frac{Y^2Z}{R^3r^2}\right)\right] \tag{1}$$

in which μ = Poisson's ratio, and all other symbols have the meanings indicated in Figure 1. For the complete derivation of Eq. 1, see S. Timoshenko (11). Poisson's ratio for soil has always been very difficult to ascertain. The range of Poisson's ratio varies from $\mu = 0$ to $\mu = 0.5$. It can be said that the order of magnitude of Poisson's ratio for soil must be closer to the upper limit of 0.5 than to the lower limit of zero. Eq. 1 would then be simplified and results in:

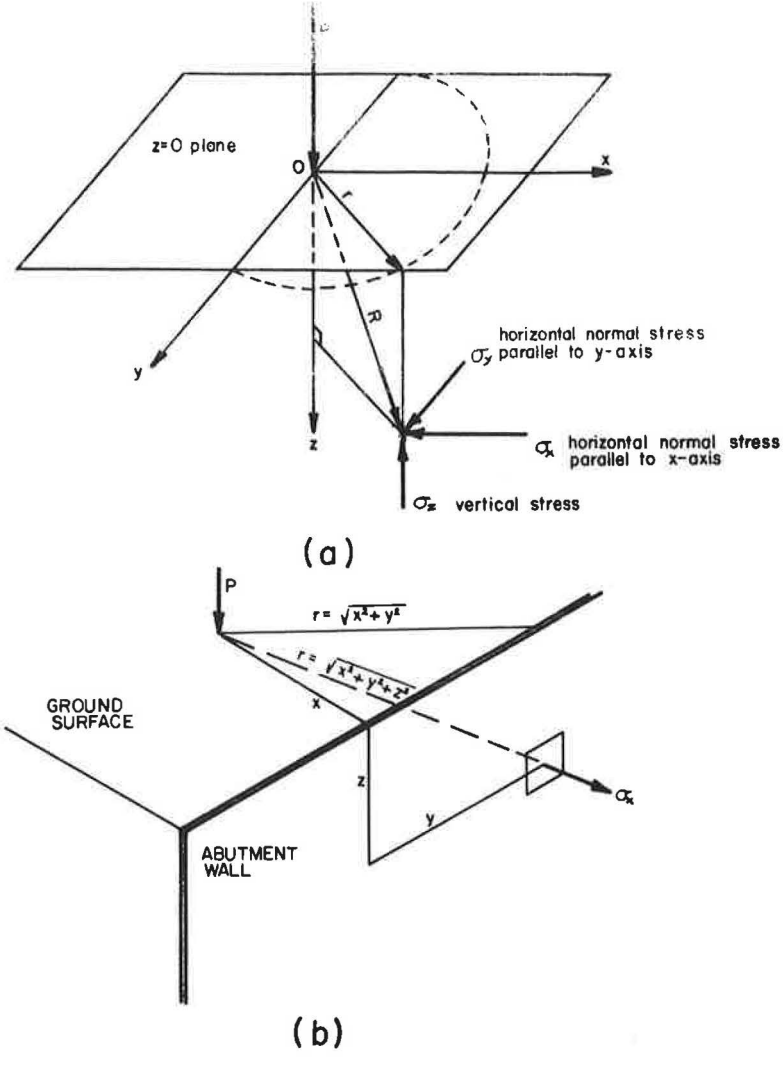

Figure 1. Lateral stress distribution created by concentrated surface load: (a) stress components created by concentrated load, and (b) lateral stress on abutment wall created by concentrated wheel load.

$$\sigma_X = \frac{3P}{2\pi} \frac{X^2 Z}{R^5} \tag{2}$$

Calculations for Theoretical Pressures

Calculations were made, according to Boussinesq's theory, to determine the location of the load for the maximum lateral pressure in a horizontal plane. This was accomplished by two methods. First, calculations were made for horizontal planes passing through the depths of 1, 2 and 3 ft with a unit load placed every one-half foot from the wall, on the centerline, until the maximum values of lateral pressures were obtained. The resulting curves are shown in Figure 2. Second, the Boussinesq equation was differentiated with respect to X (the distance from the wall) to determine the location of the load for maximum lateral pressure. Solving for x gave the relationship $X = Z\sqrt{2/3}$.

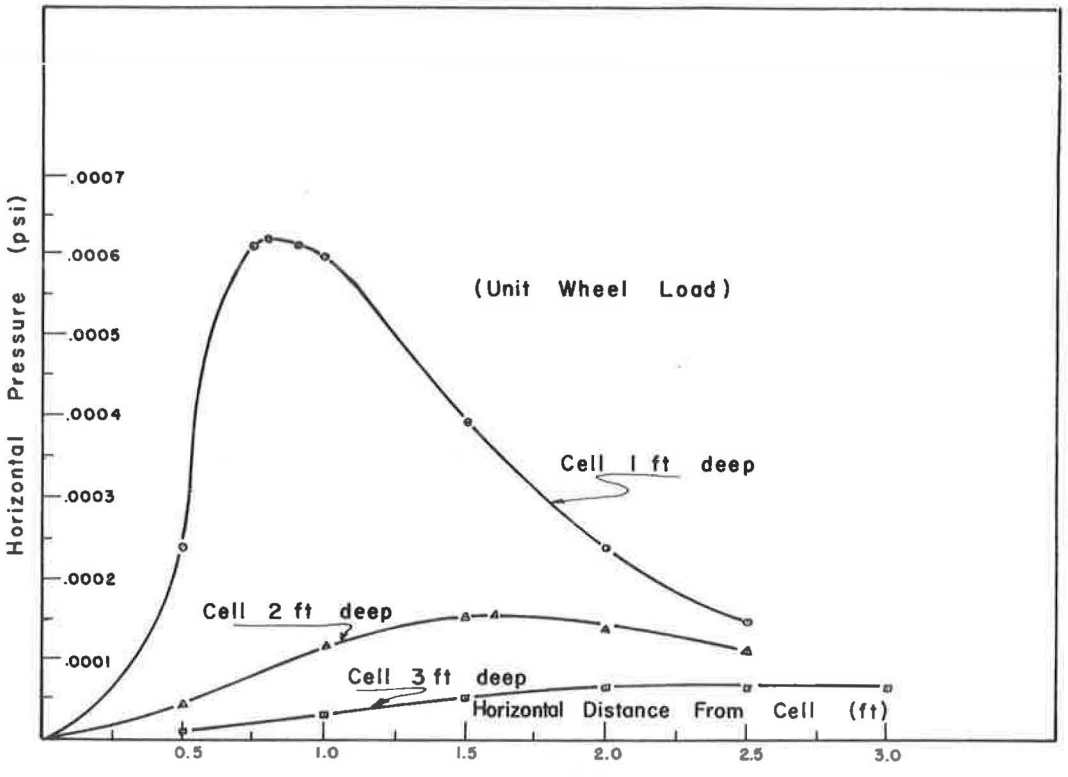

Figure 2. Theoretical variation in horizontal pressure as a wheel load approaches pressure cell.

The relationship is shown in Figure 2, in which the theoretical pressure distribution is plotted in a manner similar to that of an influence line. These calculations determined where the load should be placed to obtain the maximum lateral pressure in the horizontal planes at depths of one, two and three feet. To determine the maximum lateral pressure in this vertical plane, the Boussinesq equation was differentiated with respect to Z (the distance below the surface). The maximum lateral pressure in the vertical plane will theoretically occur at a depth $Z = X/2$.

EXPERIMENTAL SETUP

The Test Abutment

The test abutment was designed as a part of a larger research project for the New Mexico State Highway Department. An isometric view with dimensions is shown in Figure 3. It is apparent that there is a definite difference in the construction of the two walls. The flexible wall is basically a simple cantilever type. The rigid wall is a step type cantilever and is constructed rigidly. This was done to determine the variations in soil pressure with respect to the relative rigidity of wall construction.

Figure 4 shows an end view of the test abutment before the backfill material was placed. Figure 5 shows the approach from the roadway after backfilling.

The Test Vehicle

The test vehicle is shown diagrammatically in Figure 6. The truck was loaned to the project by the New Mexico State Highway Department. The truck was loaded evenly with iron rails and the resulting wheel loads were as follows: front wheels, 2,350 lb each wheel; and rear wheels, 10,400 lb each dual.

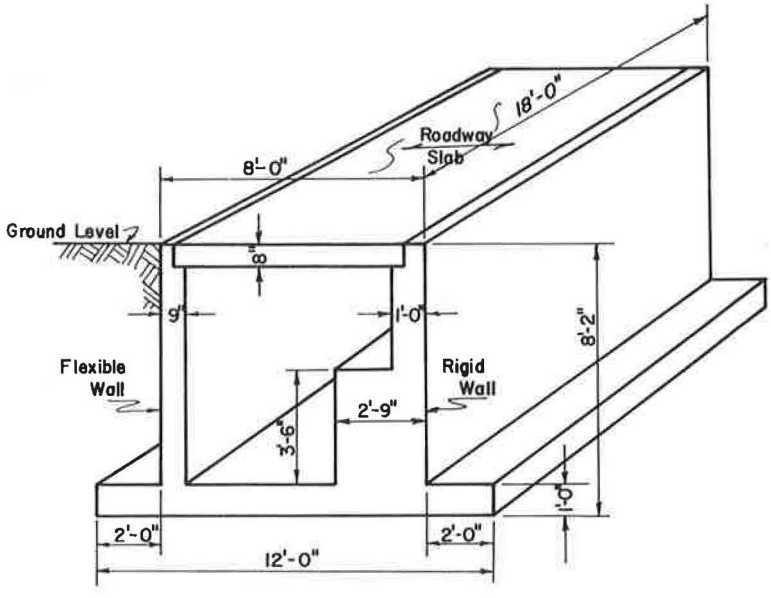

Figure 3. Test abutment.

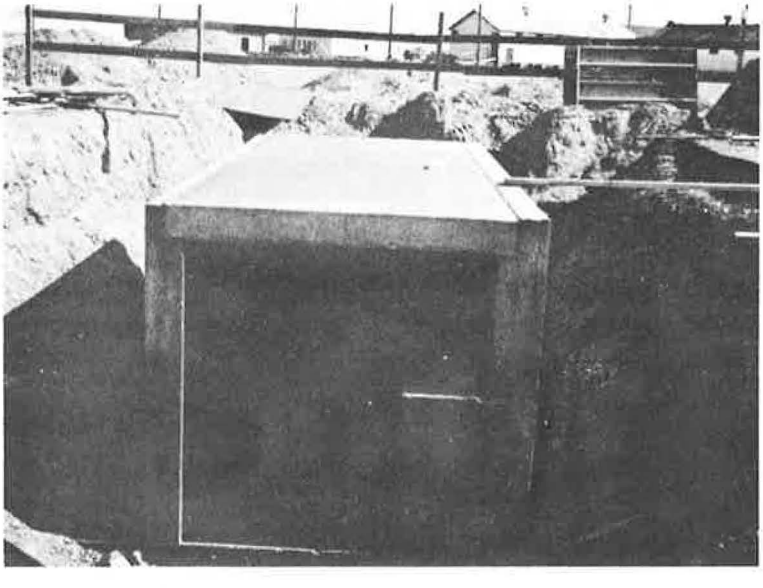

Figure 4. End view of test abutment.

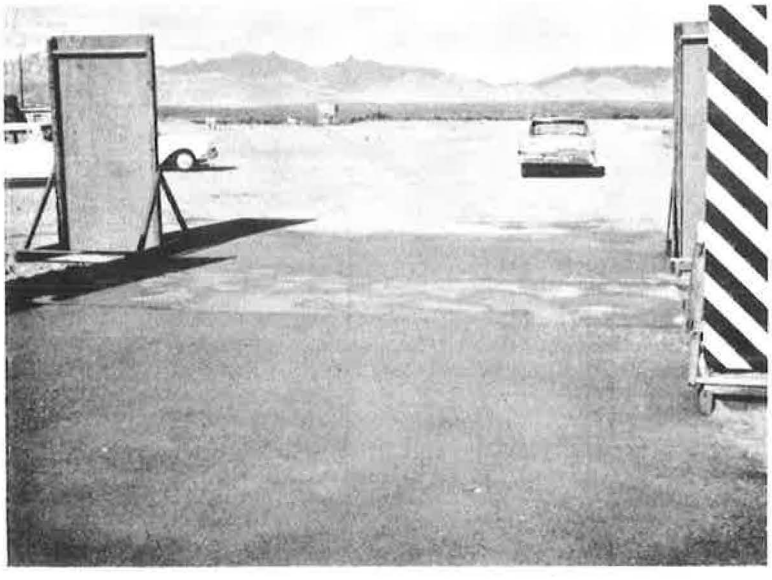

Figure 5. View of abutment from roadway showing approach.

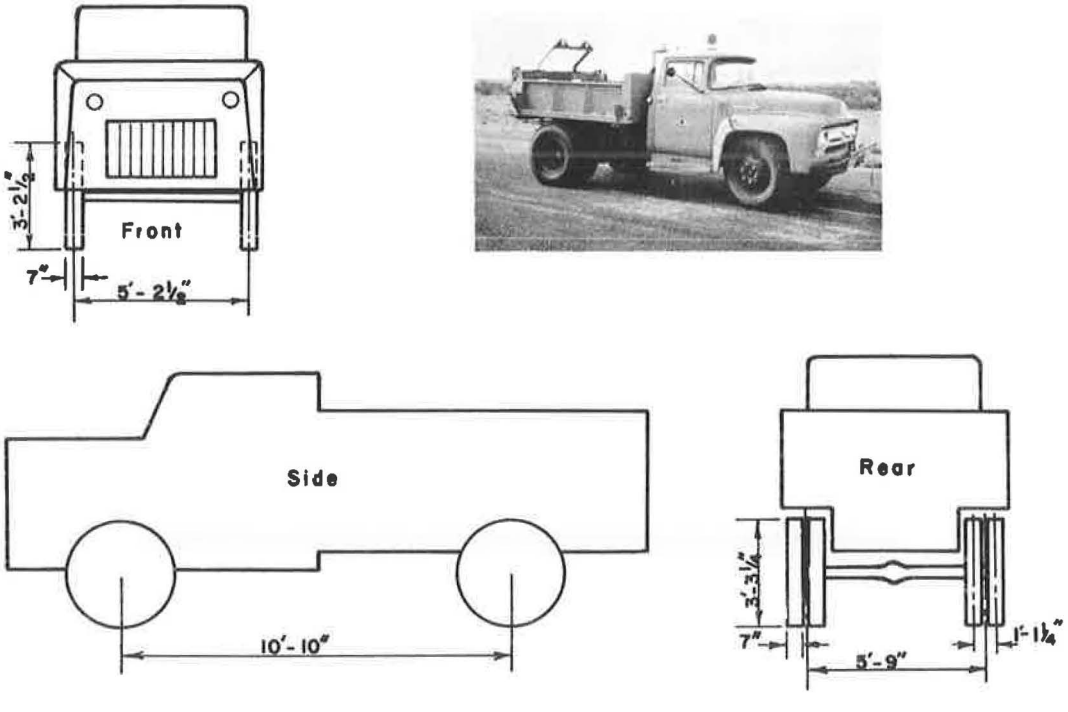

Figure 6. Single-axle truck.

Backfill Materials

Two different backfill materials were used in this study. The first material was a native soil found at the test site; its gradation is shown in Figure 7. The uniformity coefficient of the native soil was 13.9, which should normally designate a well-graded soil. It was apparent from the gradation curve that the material was gap-graded. This was to be expected because the material was used as it was uncovered and the gap-grading may be traced directly to the action of weathering of the soil. The characteristics

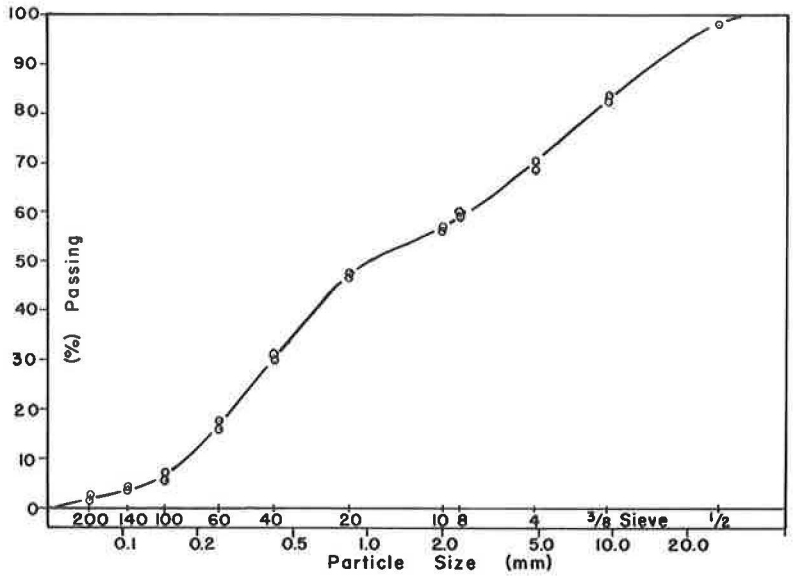

Figure 7. Gradation of selected backfill material (native).

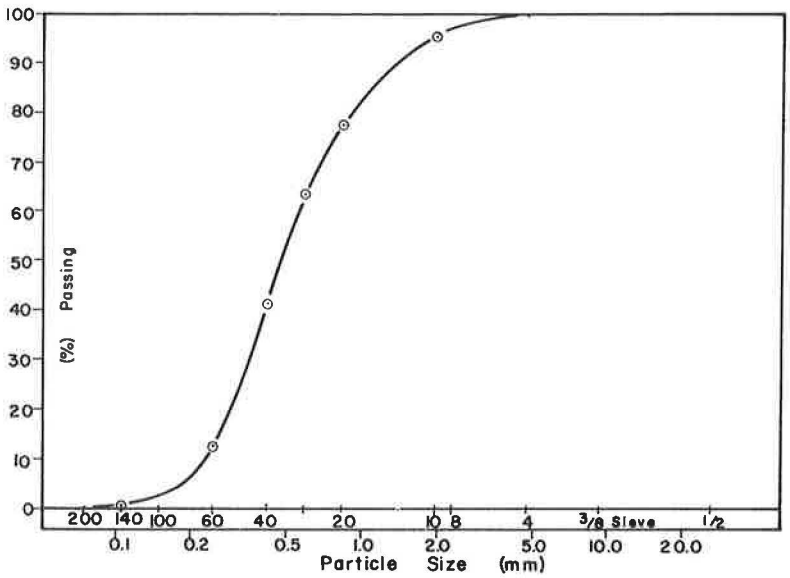

Figure 8. Gradation of sand backfill material.

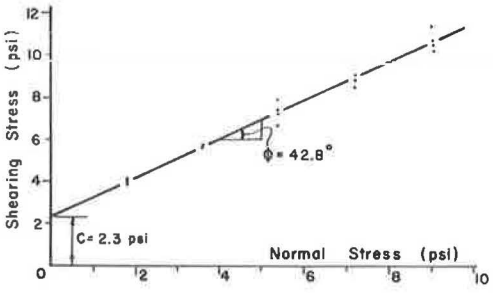

Figure 9. Direct shear envelope for native backfill material.

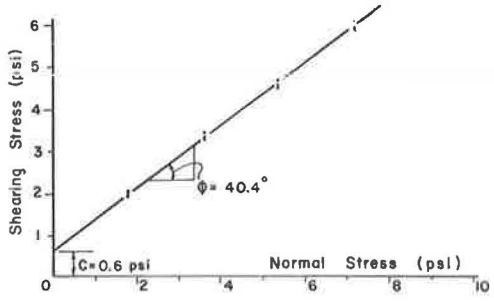

Figure 10. Direct shear envelope for sand backfill material.

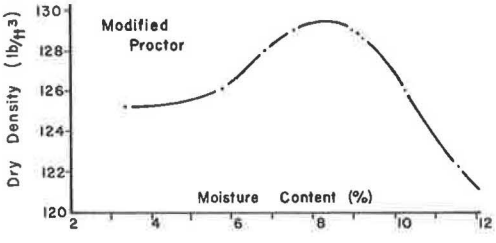

Figure 11. Moisture-density relationship for native backfill material.

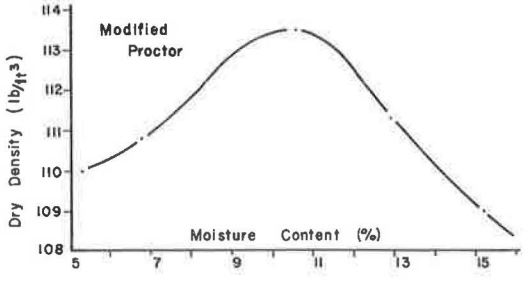

Figure 12. Moisture-density relationship for sand backfill material.

of gradation of this soil, and the adequate but not excess of fine material, allowed this soil to be compacted to a very dense condition.

The second soil used for backfill was a clean washed plaster sand; its gradation is shown in Figure 8. The uniformity coefficient for the sand was 2.39, which was considered a uniform material.

The standard direct shear test was run to determine the angle of internal friction and the cohesive properties of both soils.

The direct shear envelope for the native soil backfill is shown in Figure 9. The angle of internal friction of the native soil was found to be 42.8°, and the effective cohesion was 2.3 psi. The direct shear envelope for the plaster sand backfill is shown in Figure 10. The angle of internal friction for the sand was found to be 40.4°, and the effective cohesion was 0.6 psi.

Compaction tests were made on both soils to enable the achievement of the greatest amount of compaction when backfilling. The moisture-density relationships for the native soil backfill and the plaster sand are shown in Figures 11 and 12, respectively. The maximum dry density was found to be 129.5 pcf at a water content of 8.5 percent for the native soil. The plaster sand had a maximum dry density of 113.5 pcf at a water content of 10.5 percent. The Modified Proctor test was used to determine these relations.

Placing of Backfills

The native soil was placed into the excavated hole by hand and was compacted in 4- to 6-in. layers by using a pneumatic tamper. The pneumatic tamper was necessary in compacting the native soil due to the larger particle sizes of the material. Random in-place density tests were made to check the degree of compaction achieved. The water-balloon method was used in determining the volume of the test hole. This method was used on both backfill materials. In-place densities for the native soil are given in Table 1.

TABLE 1

IN-PLACE DENSITY RESULTS FOR NATIVE SOIL

Dist. from Wall (ft)	Depth from Surface (ft)	Dist. from Centerline	Water Content (%)	Dry Density	Percent of Modified
		(a) Flexible Wall			
2.0	4.0	Centerline	8.8	121.0	93.5
2.0	4.0	6 ft South	6.3	109.0	84.2
2.0	4.0	6 ft North	7.3	113.3	87.5
2.0	2.5	Centerline	5.3	108.5	83.7
2.0	1.5	Centerline	9.4	122.2	94.6
2.0	1.5	6 ft North	8.7	127.0	98.4
2.0	1.5	6 ft South	7.5	135.5	105.0
		(b) Rigid Wall			
2.0	4.0	Centerline	8.5	121.2	93.8
2.0	3.0	6 ft North	7.5	115.7	89.6
2.0	3.0	Centerline	8.9	128.5	99.5
2.0	3.0	6 ft South	8.8	118.8	91.7
2.0	2.0	Centerline	6.6	123.0	93.3
2.0	2.0	6 ft South	10.2	122.2	94.6
2.0	2.0	6 ft North	6.9	121.5	94.0
		(c) Rigid Wall After Rolling			
5.0	Surface	Centerline	6.8	123.0	95.3
		(d) Flexible Wall After Rolling			
2.0	Surface	Centerline	4.1	137.5	106.7

TABLE 2

IN-PLACE DENSITY RESULTS FOR PLASTER SAND

Dist. from Wall (ft)	Depth from Surface (ft)	Dist. from Centerline	Water Content (%)	Dry Density	Percent of Modified
		(a) Flexible Wall			
3.0	3.0	Centerline	11.7	112.2	99.0
3.0	2.0	Centerline	15.5	108.6	95.7
3.0	1.0	Centerline	15.1	107.5	94.7
		(b) Rigid Wall			
4.0	3.0	Centerline	10.0	112.1	99.0
2.5	3.0	Centerline	9.7	105.0	92.5
2.0	2.0	Centerline	12.6	112.5	99.2
1.0	2.5	Centerline	11.2	111.9	98.5

The washed plaster sand used was also placed by hand. The method of compaction used was vibration, which employed a hand vibratory compactor in a single unit. Random in-place density tests were also made. In-place densities for the washed plaster sand backfill are given in Table 2.

After the backfill materials had been placed and compacted, the last operation was the use of a steel-wheel roller to compact the top two to three inches. The roller created a smooth approach to the test area.

Pressure Cells

Two types of pressure cells were used. The first was a can-type pressure cell. Each cell was instrumented with four bonded resistance-type strain gages, which made up the four legs of one Wheatstone Bridge. This provided an extremely sensitive pressure cell. The sensitivity of pressure reading was needed to measure some of the smaller pressures recorded.

The second type of pressure cell was a Carlson stress meter for soils manufactured by Roy Carlson of Berkeley, California. The Carlson cell is basically a half-bridge circuit. When a pressure is applied to the face of the cell, one resistance decreases while the other increases. These cells were used to determine the lateral pressures at the wall; while the can-type pressure cells measured the lateral pressures in the soil.

Figure 13 shows the apparatus used in the calibration of the pressure cells. The can-type cells were embedded in the soil at the center of the elastic membrane. A static load was applied at the end of the lever arm and the pressure was recorded. The soil used in the elastic membrane was compacted until a compaction near field conditions was achieved. Each cell was calibrated a minimum of three times by loading and unloading until the calibration curve was reproduced. The Carlson cells were calibrated by application of a direct uniform load. These cells were also calibrated a minimum of three times. The calibration curves for three of the can-type pressure cells, which are representative of the sensitivity and linearity of all the can-type cells, are shown in Figure 14. Figure 15 shows the calibration curves for the Carlson cells.

Each cell was hand placed in the backfill material. The soil was compacted about six to eight inches above the desired location. A small amount of soil was then removed

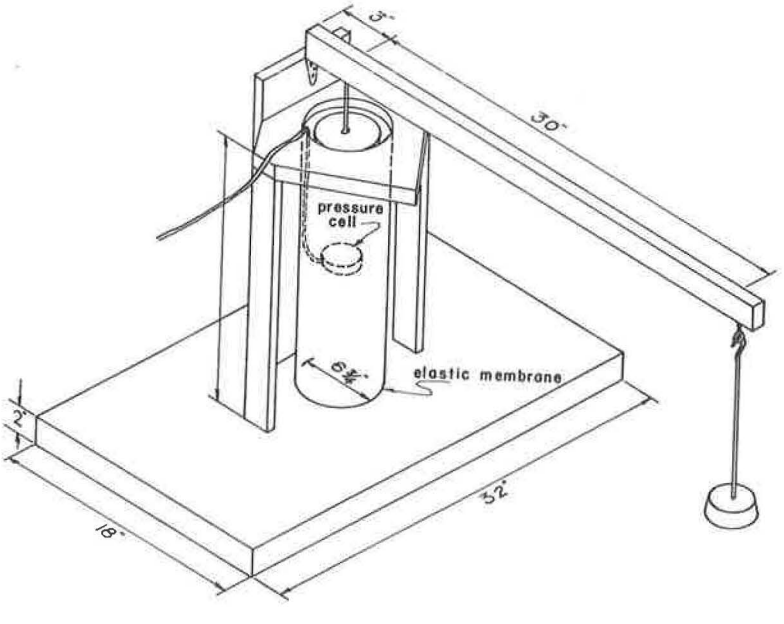

Figure 13. Calibration apparatus.

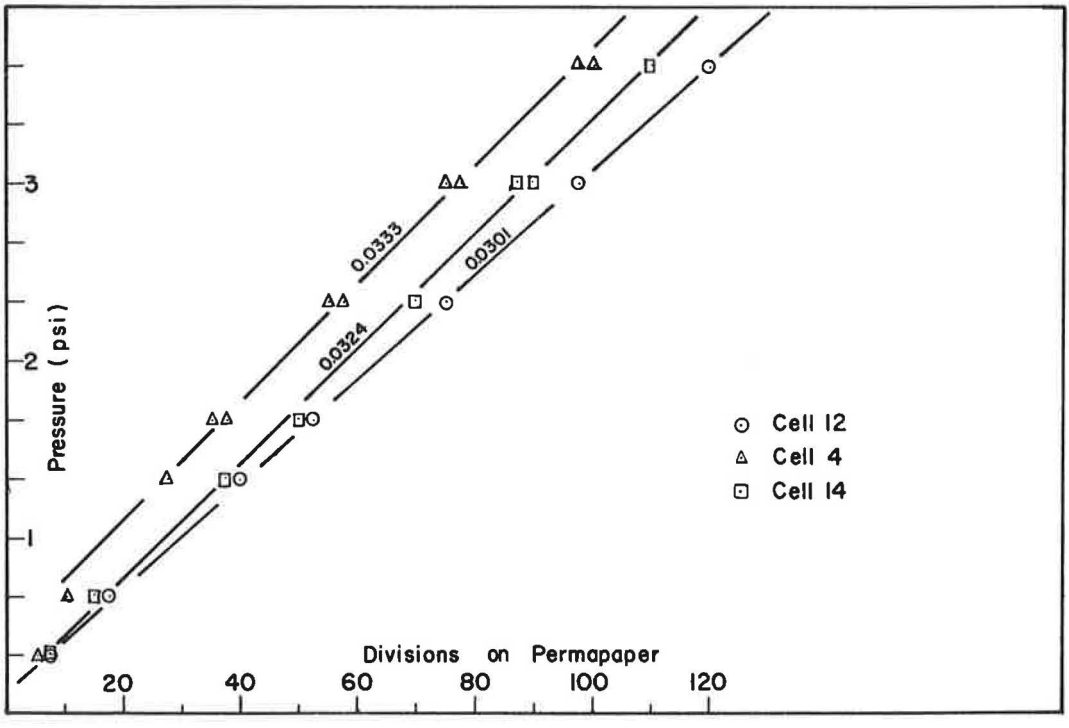

Figure 14. Calibration of can type pressure cells.

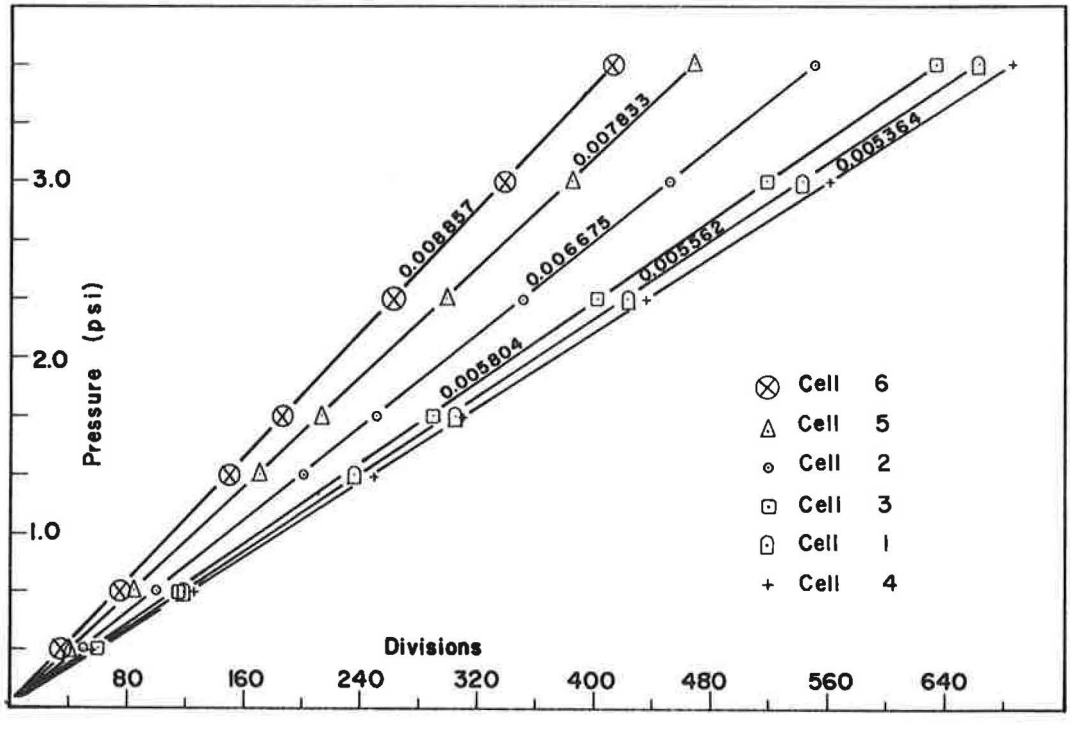

Figure 15. Calibration of Carlson pressure cells.

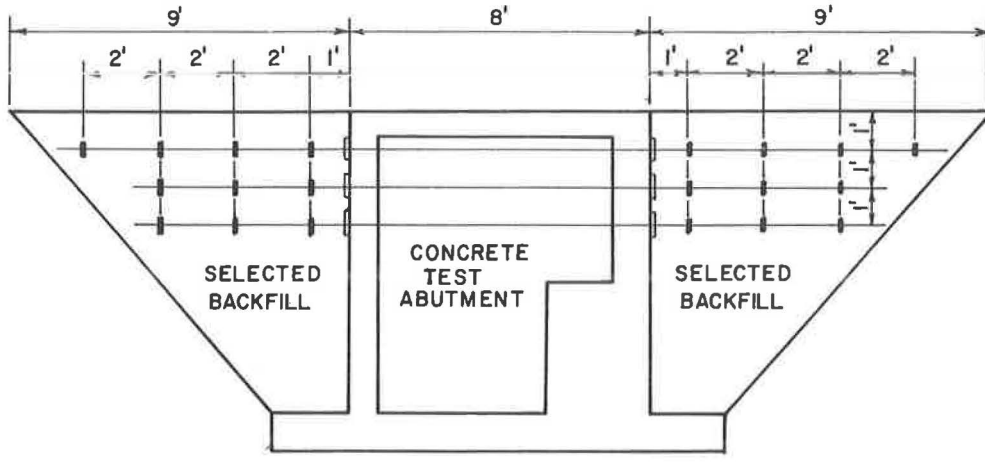

CAN TYPE PRESSURE CELL ▮
CARLSON TYPE PRESSURE CELL ▯

Figure 16. Location of pressure cells in backfill (native).

by using a post-hole digger and the cell was properly positioned. The soil was replaced and compacted around the cell. This procedure was used to achieve a uniform compaction of the soil around the cell. Figure 16 shows the location of the pressure cells in the native soil backfill. All cells were placed on centerline. The location of the pressure cells in the sand backfill was similar to the native soil, except the outer two rows of cells were omitted. After running the tests on the native soil, it was determined that less cells could be used because the pressures in the backfill away from the wall did not change.

EXPERIMENTAL PROCEDURE

To determine the distribution of lateral pressure both vertically and horizontally at the face of the abutment and also in the backfill, a method of locating the load at different points on the backfill was set up. A grid was laid out on the surface of the backfill as shown in Figure 17.

It should be restated here that all pressure cells were located on centerline. By locating the load on grid line 3N, 3 ft north of the centerline, the pressure would be measured at the centerline. This pressure would be the same as the pressure at 3N if the wheel was located at the centerline by reciprocal pressures. The above approach was used over the entire grid to give the complete picture of the pressure distribution.

Tests were conducted with the front and rear wheels to study the effect of different wheel loads. The front wheel was used first. The truck was driven as slowly as possible without stalling from a point approximately ten feet from the wall over one of the grid lines perpendicular to the wall. A continuous pressure reading was taken as the truck approached the abutment. Sanborn Recorders were used for recording the pressures measured by the pressure cells. A continuous record of the pressures was made as the truck approached and passed over the cells. Figure 18 shows a representative recording for a pressure cell at the wall and in the soil mass respectively. When the front wheels were on the abutment, the truck was stopped, thus assuring that the load carried by the rear wheels did not affect the soil pressures created by the front wheels. Each test was conducted a minimum of three times whenever possible.

The procedure used in conjuction with the rear wheels was exactly the same as that used for the front wheel except the truck was backed onto the backfill surface. The truck was placed so that the grid line was exactly in the center of the dual tires. When the test wheels were on the abutment, the truck was stopped to insure that the load

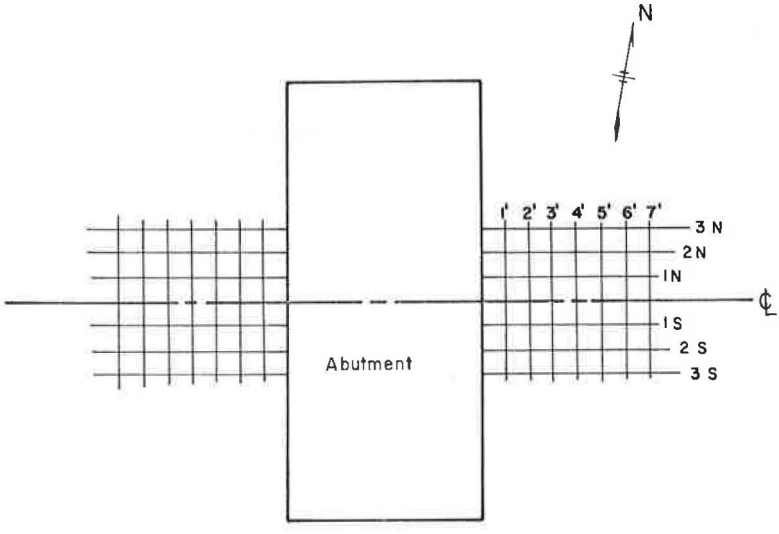

Figure 17. Grid pattern for location of surface wheel loads.

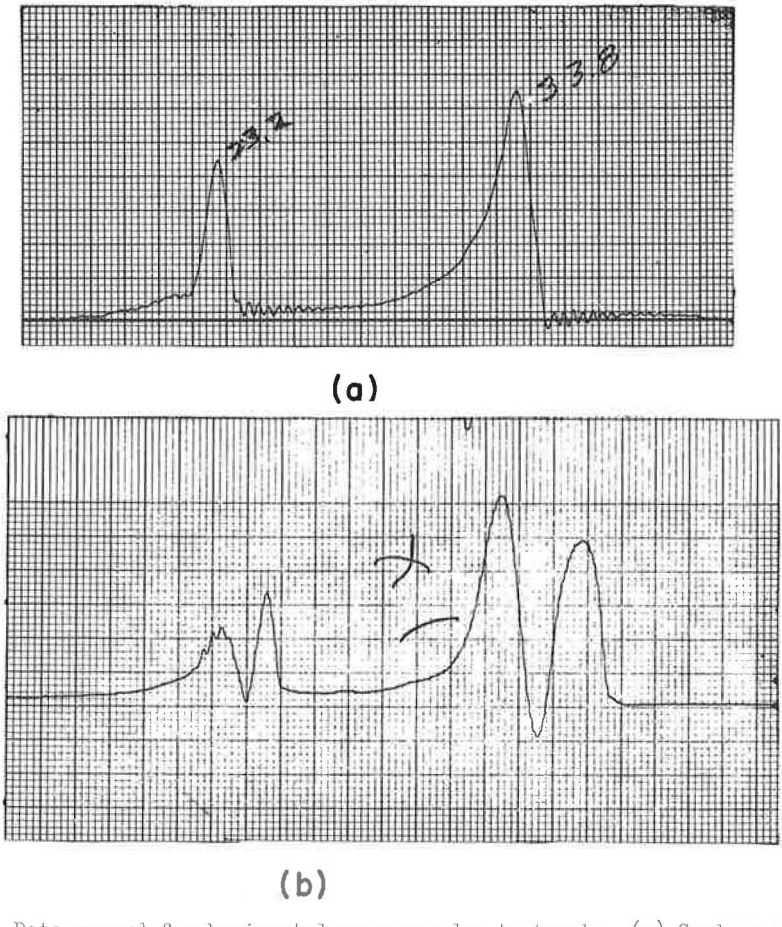

Figure 18. Data record for horizontal pressure due to truck: (a) Carlson pressure cell data at wall, and (b) can type pressure cell data in soil.

carried by the front wheel did not affect the soil pressures. These tests were also conducted a minimum of three times whenever possible.

To measure the relative magnitude of the deflection of the flexible wall under load, an Ames dial was mounted at the top of the wall on the inside, directly on centerline.

TEST RESULTS

This research resulted in six series of tests designated series A through F. In general, each series letter defines a particular physical setup in the testing program. The results of tests in each series are presented in the form of pressure bulbs. These resulting pressure bulb curves are compared with theoretical curves of the Boussinesq solution.

Series A—Comparison of the pressure created in the native soil by the front wheel of the truck to the pressure created in the sand backfill by the front wheel.

Series B—Comparison of the pressure created in the native soil by the rear wheel of the truck to the pressure created in the sand backfill by the rear wheel.

Series C—Comparison of the pressure created against the rigid wall for the front wheel of the truck and the native soil to the pressure created against the rigid wall for the front wheel and the sand backfill.

Series D—Comparison of the pressure created against the rigid wall for the rear wheel of the truck and the native soil to the pressure created against the rigid wall for the rear wheel and the sand backfill.

Series E—Comparison of the pressure created against the rigid wall for the front wheel of the truck and the sand backfill to the pressure against the flexible wall for the front wheel and the sand backfill.

Series F—Comparison of the pressure created against the rigid wall for the rear wheel of the truck and the sand backfill to the pressure created against the flexible wall for the rear wheel and the sand backfill.

The graphs are smooth curves through the approximate averages of the test points; however, all test points are shown for realistic comparison. The theoretical curves were calculated using the Boussinesq equation for lateral pressures under the test vehicle wheel loads.

Pressures in Soil Mass

Test Series A. —Figure 19 shows the theoretical and experimental curves for the distribution of lateral pressure created in the native soil backfill by the front wheel of the truck. The experimental pressure measured on centerline at a 1-ft depth was approximately 76 percent of the theoretically calculated value; at a 2-ft depth, 67 percent; and at a 3-ft depth, 81 percent.

Figure 20 shows the distribution of lateral pressure created in the sand backfill by the front wheel of the truck. At a 1-ft depth on centerline, the measured pressure was 99 percent of the calculated theoretical value and was well approximated by the theoretical curve so that an experimental curve was not necessary. At a 2-ft depth the pressure was 67 percent of the theoretical value, and at a 3-ft depth, about 81 percent.

Comparing the results obtained for the native soil with those of the sand backfill shows the sand to have slightly higher pressure in the top foot of the soil created under identical load. The pressures at 2- and 3-ft depths were nearly equal.

Test Series B. —Figure 21 shows the distribution of lateral pressure created in the native soil backfill by the rear dual tires. At a 1-ft depth on centerline the measured pressure was 62 percent of the theoretical; at a 2-ft depth, 60 percent; and at a 3-ft depth, the measured pressure compared closely with the theoretically computed values.

Figure 22 shows the distribution of lateral pressure created in the sand backfill by the rear dual tires. At a 1-ft depth on centerline the measured pressure was 86 percent of the theoretical value; at a 2-ft depth, 64 percent; and at a 3-ft depth, the resulting pressure was approximately the same as the theoretical value and the experimental curve was not shown.

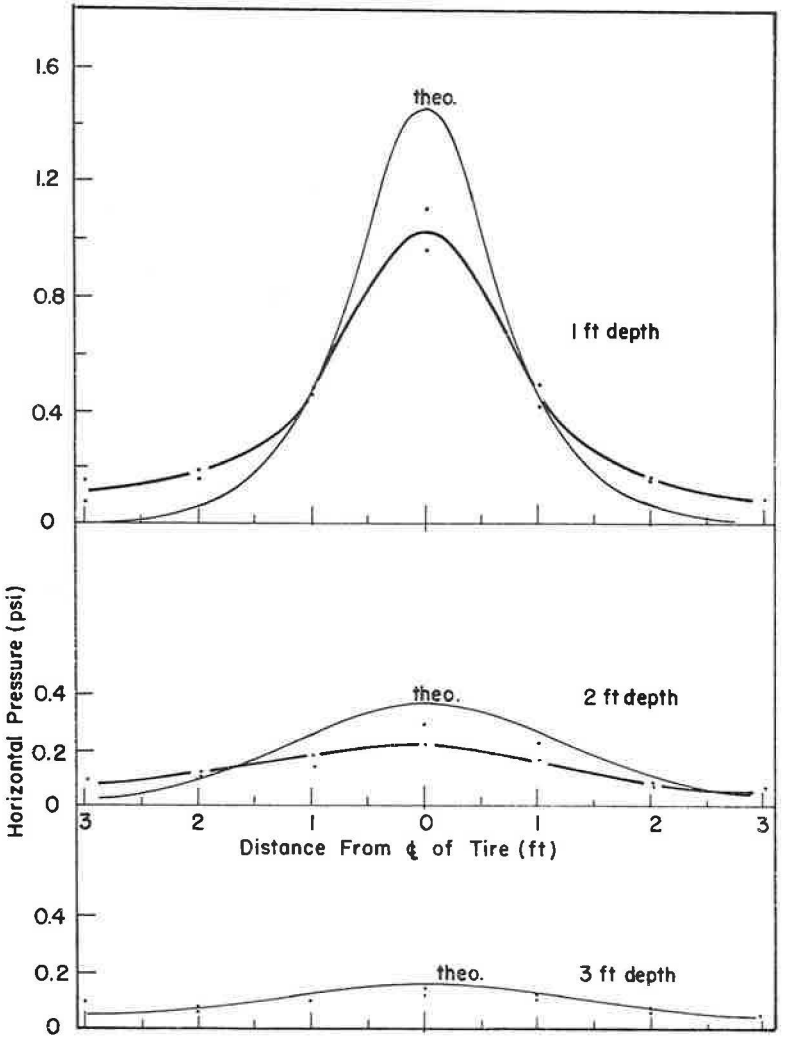

Figure 19. Distribution of lateral pressure in soil for truck front tire (native).

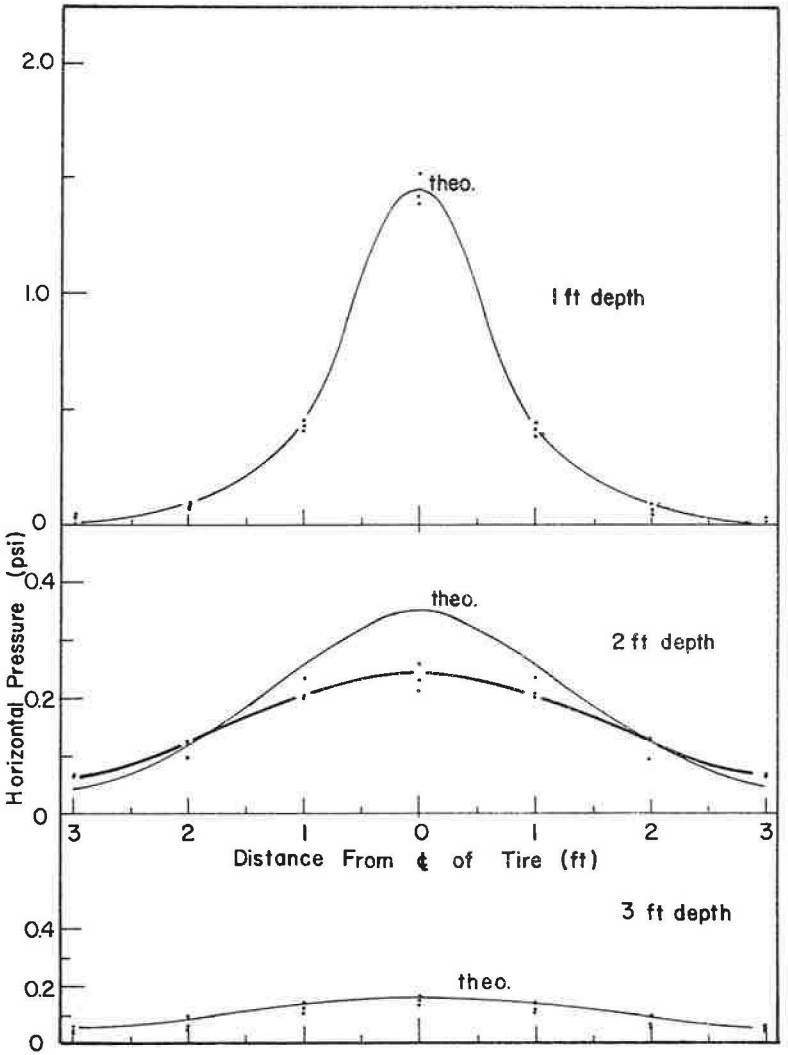

Figure 20. Distribution of lateral pressure in soil for truck front tire (sand).

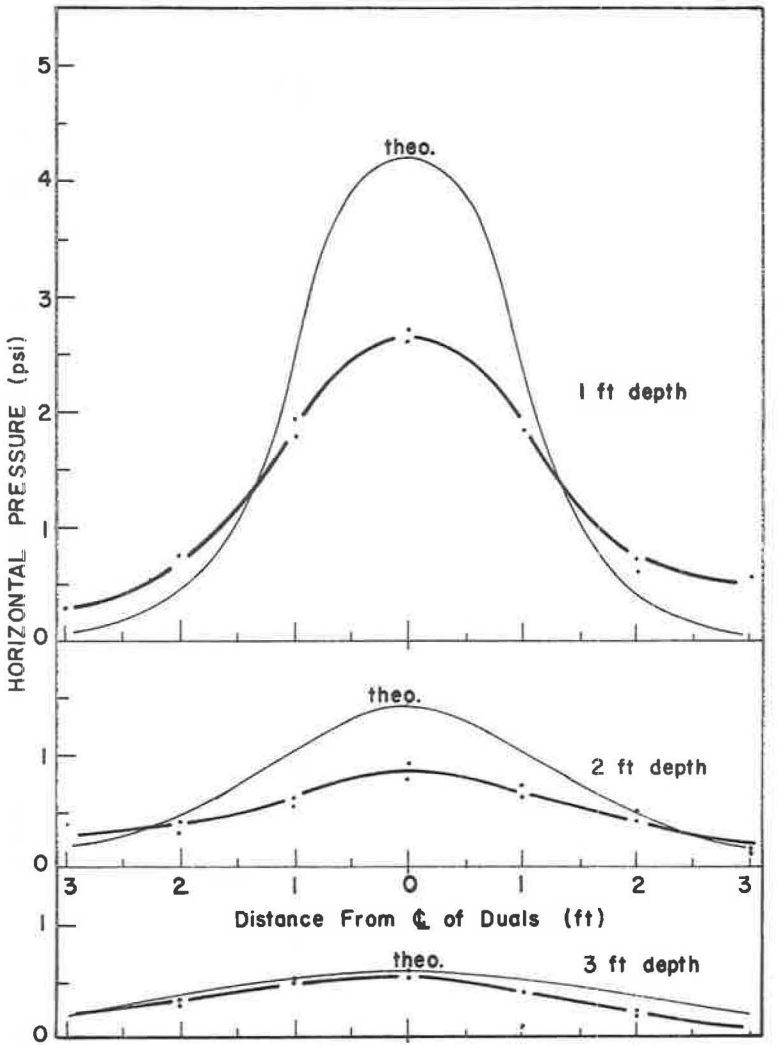

Figure 21. Distribution of lateral pressure in soil for truck rear dual tires (native).

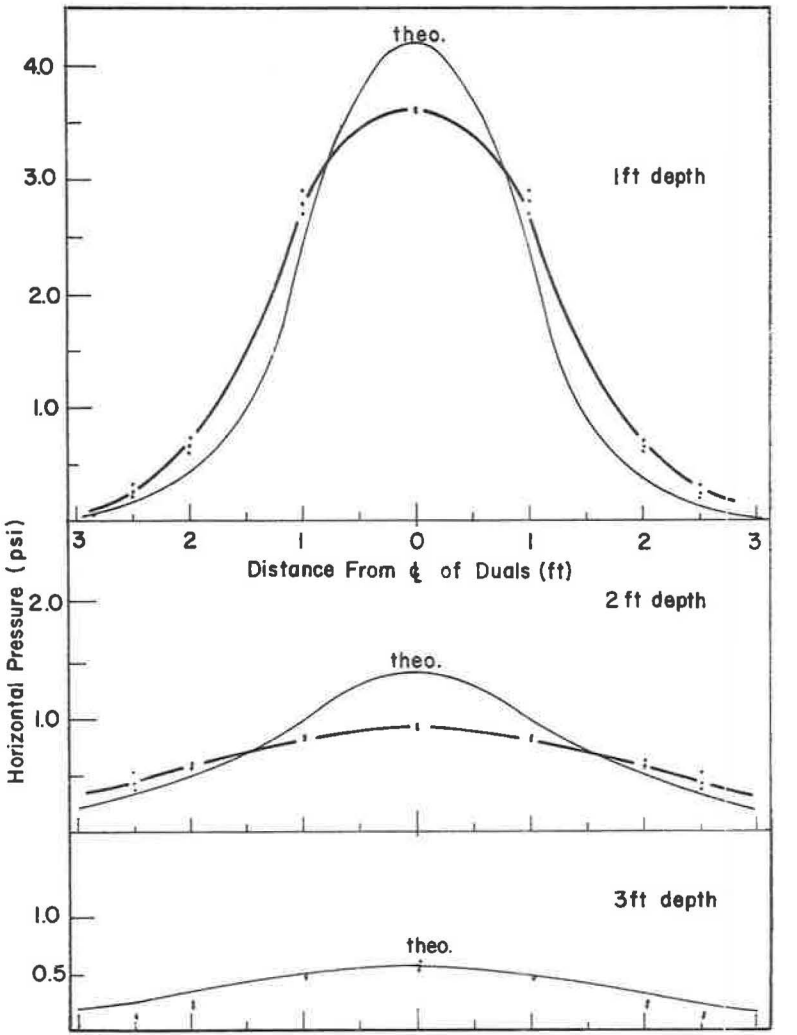

Figure 22. Distribution of lateral pressure in soil for truck rear tires (sand).

Comparing the results of the native soil with the sand backfill for the rear duals shows that the pressure created within the first foot was significantly higher in the sand backfill than in the native soil backfill. The experimental pressure measured in the sand backfill was approximately 135 percent of the pressure measured in the native soil at a 1-ft depth. The pressures at 2- and 3-ft depths were nearly equal. The experimentally measured pressures were roughtly 60 percent of the theoretical value at the 2-ft depth and almost equal to the theoretical value at the 3-ft depth.

Pressures at Soil-Wall Interface

Test Series C. —Figure 23 shows the distribution of lateral pressure against the rigid wall for the front tire of the truck on the native soil backfill. At a 1-ft depth on centerline, the pressure measured was 190 percent of the calculated theoretical value; the pressure measured at the wall was 250 percent of the pressure measured in the soil. At a 2-ft depth the pressure measured against the wall was 158 percent of the theoretical value and was 275 percent of the pressure measured in the soil. At a 3-ft depth, the pressure measured against the wall was small in magnitude but was 126 percent of the theoretical value and 154 percent of the pressure measured in the soil.

Figure 24 shows the distribution of lateral pressure against the rigid wall for the front tire of the truck on the sand backfill. At a 1-ft depth on centerline, the pressure created was 379 percent of the theoretical value. The pressure measured against the wall was 385 percent of the pressure measured in the soil. At a 2-ft depth, the measured pressure was 222 percent of the theoretical value and 333 percent of the pressure measured in the soil. At a 3-ft depth, the measured pressure was 188 percent of the theoretical value and approximately 200 percent of the pressure measured in the soil.

Figure 25 shows the soil pressure at the rigid wall for different front wheel locations on the native soil backfill. The curves illustrate the variation in soil pressures created against the wall with respect to depth for a specific wheel location on centerline. At a 1-ft depth on centerline, the pressure was maximum when the load was located approximately 0.8 ft from the wall. At 2- and 3-ft depths on centerline, the pressures were maximum when the load was located approximately 1.6 and 2.4 ft, respectively, from the wall. These curves also show how the pressure against the wall changes as the wheel of the truck approaches the abutment.

Figure 26 shows the soil pressure against the rigid wall for different front wheel locations on the sand backfill. The curves show the variation of soil pressures with respect to depth for specific wheel locations on centerline.

Comparison of Figures 25 and 26 shows the pressure development against the wall was similar in characteristics, but of varying magnitude.

Test Series D. —Figure 27 shows the distribution of lateral pressure against the rigid wall for the rear dual tires of the truck on the native soil backfill. At a 1-ft depth on centerline, the pressure measured was 152 percent of the theoretical value. The measured pressure at the wall was 241 percent of the pressure measured in the soil. At a 2-ft depth, the pressure at the wall was 153 percent of the theoretical value and 275 percent of the pressure in the soil. At a 3-ft depth, the pressure against the wall was 138 percent of the theoretical value and 150 percent of the pressure in the soil.

Figure 28 shows the distribution of lateral pressure against the rigid wall for the rear dual tires of the truck on the sand backfill. At a 1-ft depth on centerline, the pressure was 195 percent of the theoretical value; pressure at the wall was 228 percent of the pressure in the soil. At a 2-ft depth, the pressure at the wall was 216 percent of the theoretical value and 337 percent of the pressure in the soil. At a 3-ft depth the pressure against the wall was 174 percent of the theoretical value and of the pressure in the soil.

Figure 29 shows the pressures created against the rigid wall for different rear wheel locations on the native soil backfill. Figure 30 shows the pressures against the rigid wall for different rear wheel locations on the sand backfill. The experimental pressures measured in the sand backfill at the soil-wall interface were approximately 200 percent of the theoretical value for both back and front wheel loadings, except for the 1-ft depth under the front wheel where the experimental pressure was 379 percent of the theoretical.

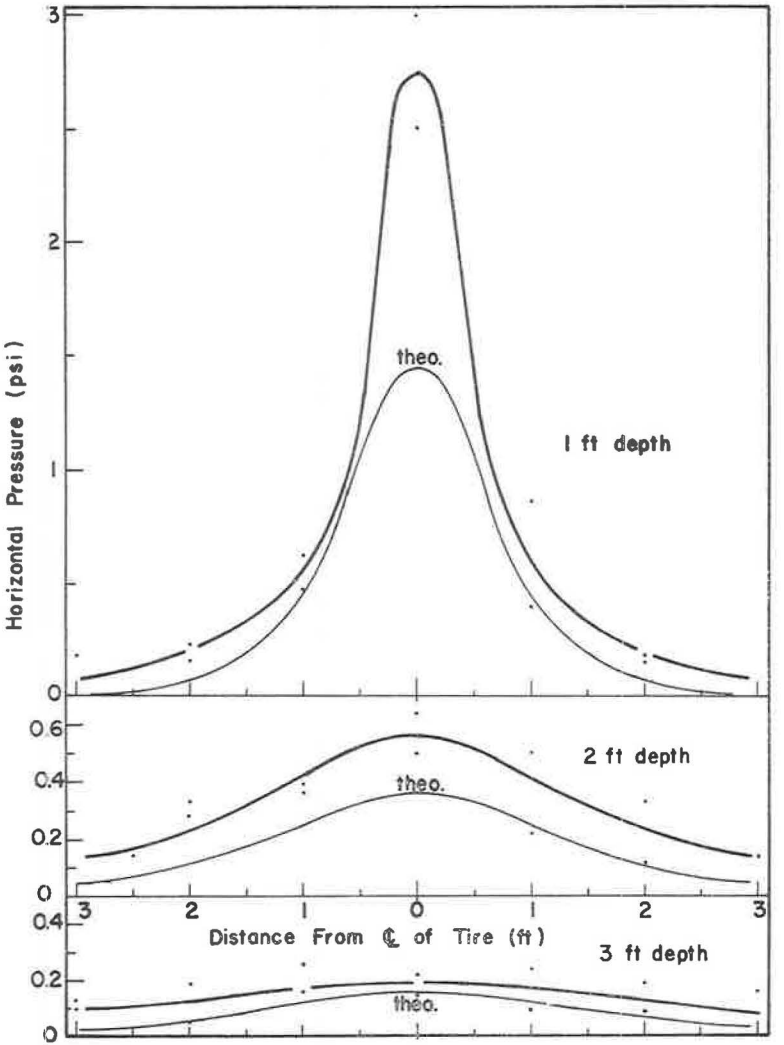

Figure 23. Distribution of lateral pressure at rigid wall for truck front tire (native).

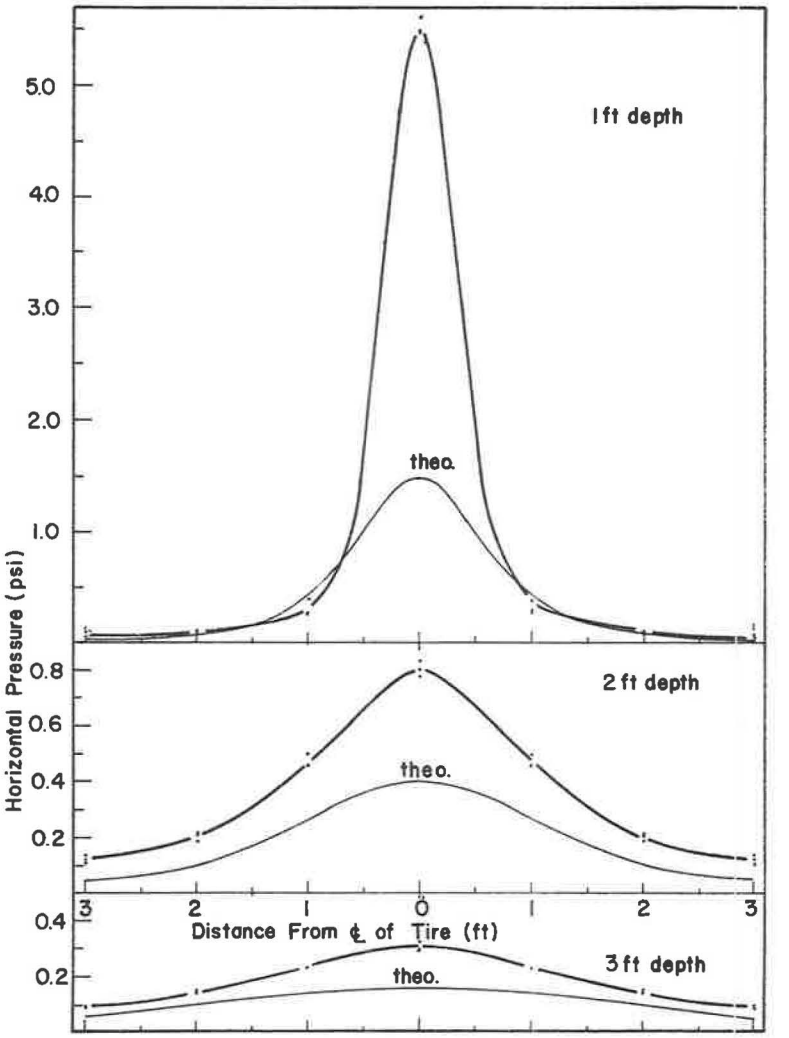

Figure 24. Distribution of lateral pressure at rigid wall for truck front tire (sand).

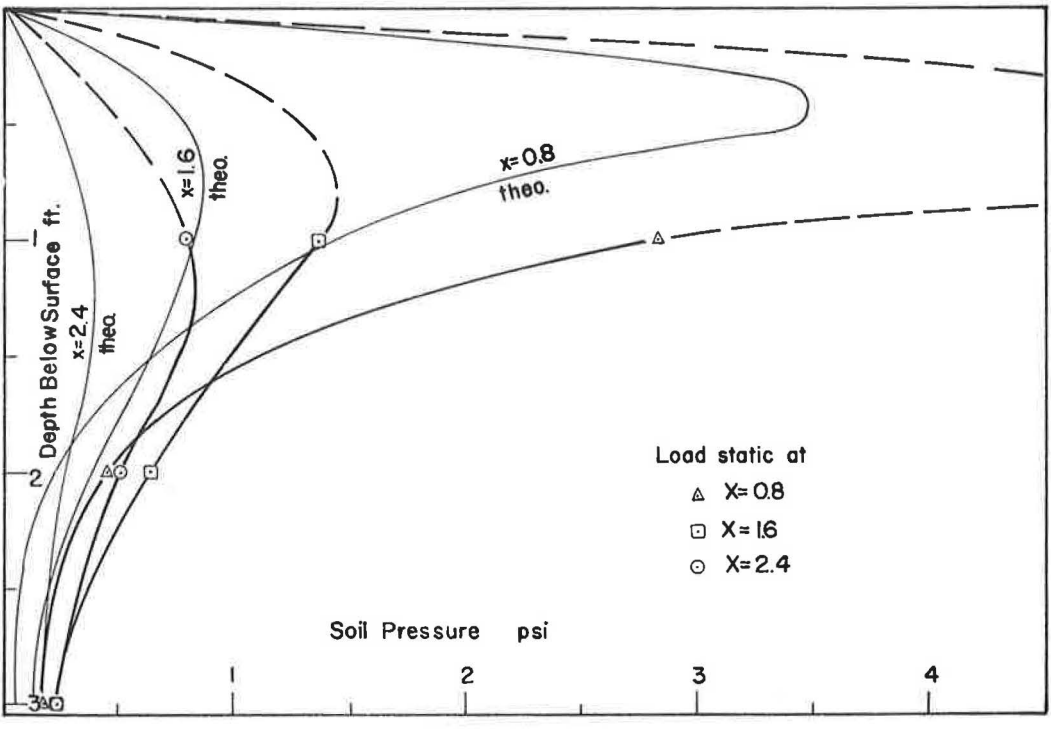

Figure 25. Soil pressure at rigid wall for different front wheel locations (native).

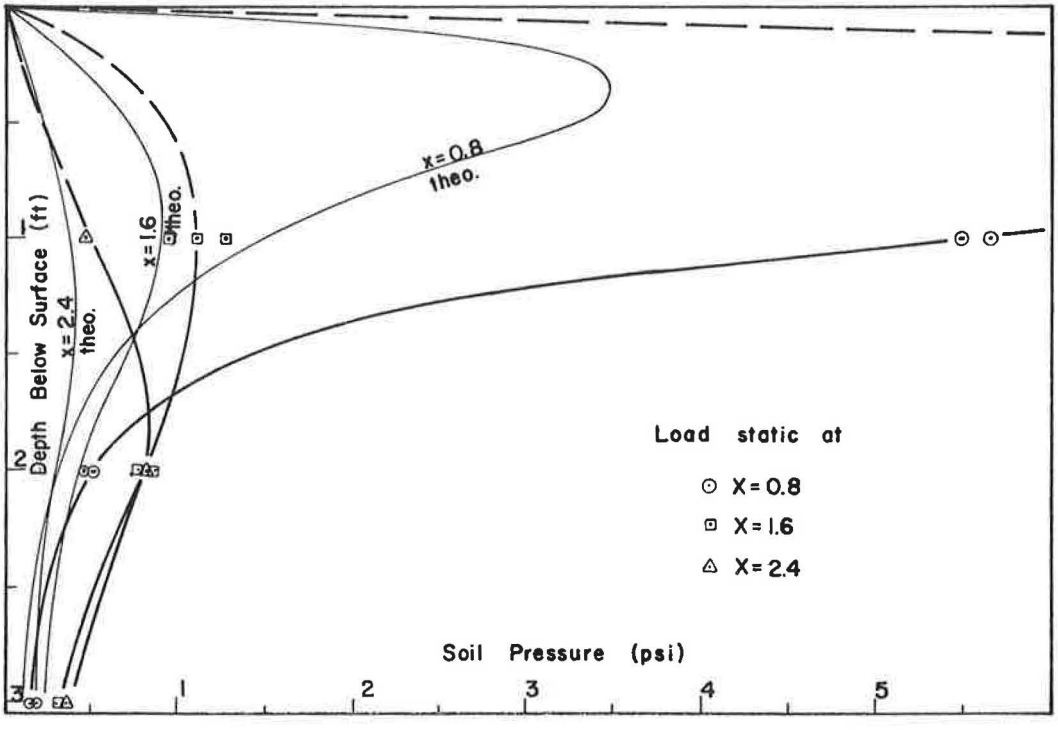

Figure 26. Soil pressure at rigid wall for different front wheel locations (sand).

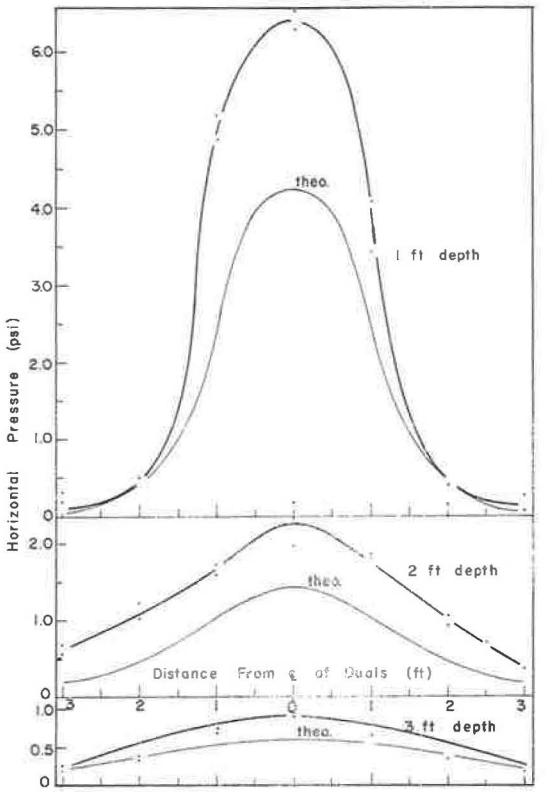

Figure 27. Distribution of lateral pressure at rigid wall for truck rear dual tires (native).

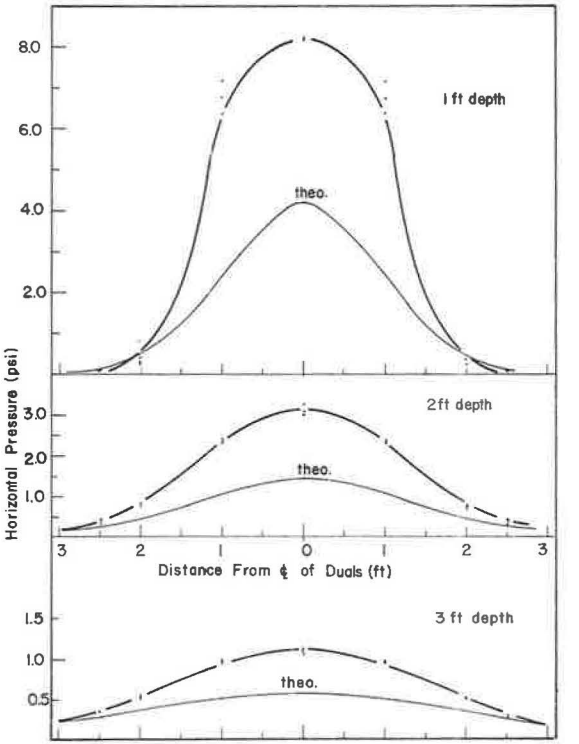

Figure 28. Distribution of lateral pressure at rigid wall for truck duals (sand).

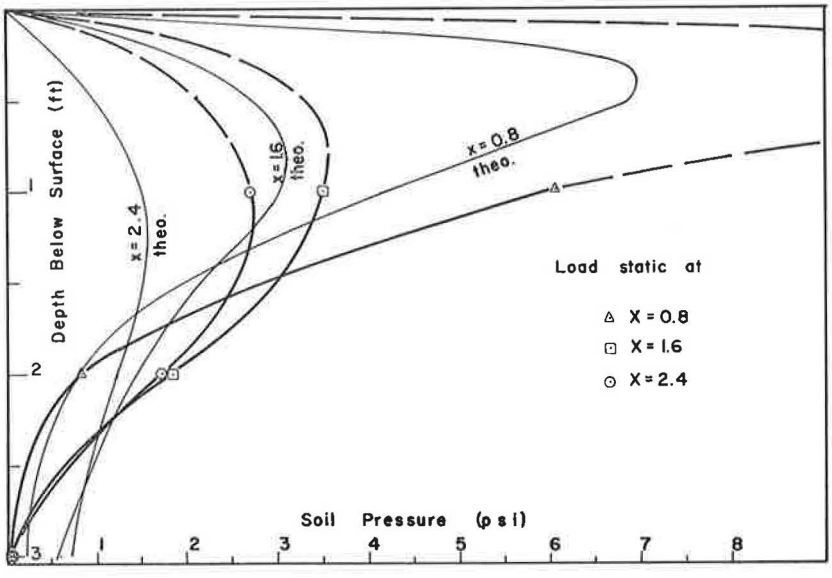

Figure 29. Soil pressure at rigid wall for different rear wheel locations (native).

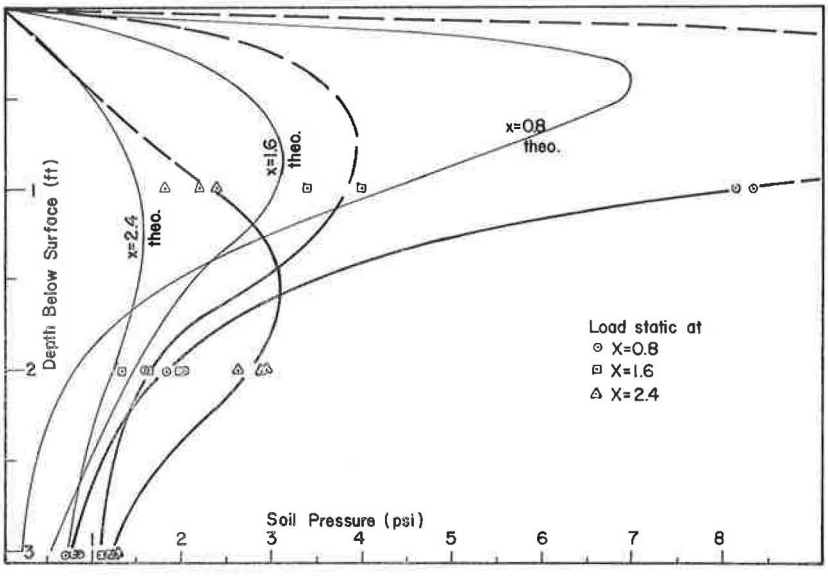

Figure 30. Soil pressure at rigid wall for different rear wheel locations (sand).

The pressures measured in the native backfill were similar in characteristics except that the pressures were approximately 150 percent of the theoretical value. The front wheel load caused a greater increase in pressure at the 1-ft depth, which was 190 percent of the theoretical value.

It is apparent that the experimental pressures at the soil-wall interface, i.e., against the wall, were 133 percent greater in the sand backfill than in the native soil backfill, with the exception noted.

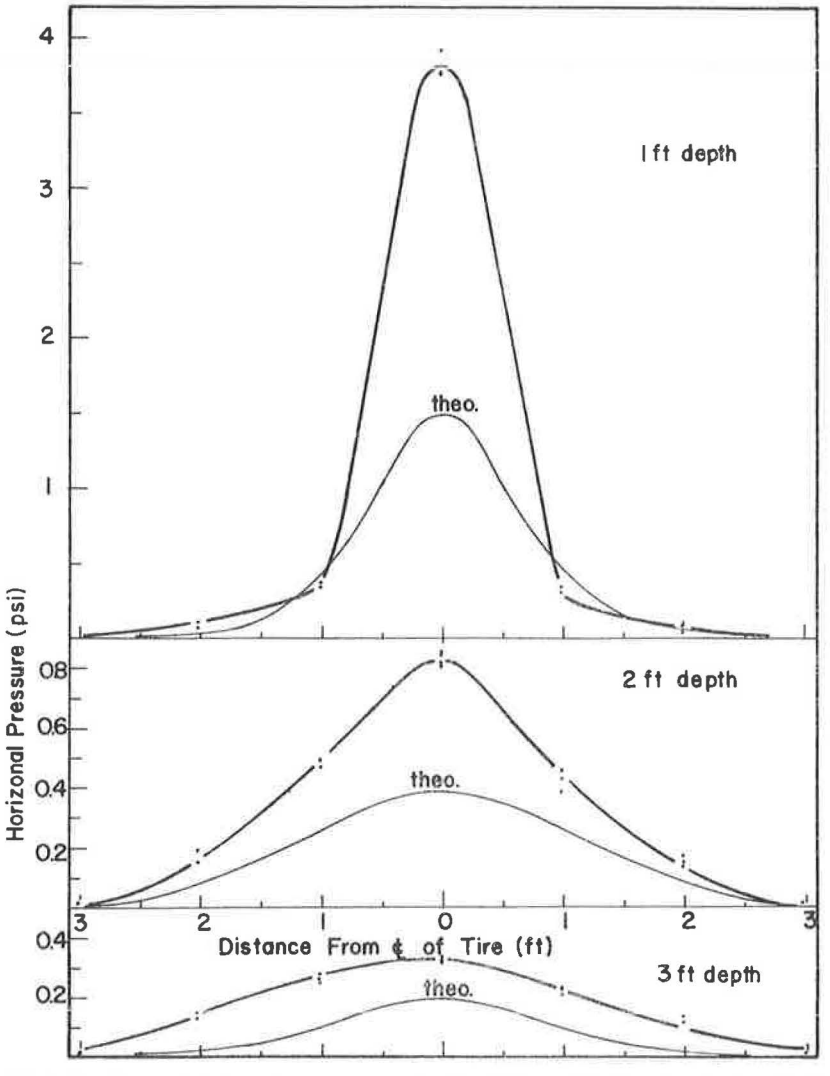

Figure 31. Distribution of lateral pressure at flexible wall for truck front tire (sand).

The increase in pressure in the sand backfill can be made more apparent by comparing Figures 25 and 29 with Figures 26 and 30. These figures, which show the variation in pressure with depth, exemplify the increase in maximum pressure in the sand at the soil-wall interface.

Test Series E. —Test series E compares the pressures against the rigid wall for the front wheel of the truck on the sand backfill to the pressure created against the flexible wall for the front wheel of the truck on the sand backfill.

Figure 31 shows the distribution of lateral pressure against the flexible wall for the front wheel of the truck on the sand backfill. At a 1-ft depth on centerline, the experimental pressure was 259 percent of the theoretical value; at a 2-ft depth, 222 percent; and at a 3-ft depth, 188 percent.

Comparison of Figure 24 and Figure 31 shows the pressures at the soil-wall interface of the rigid wall at a 1-ft depth was 133 percent greater in magnitude than at the 1-ft depth against the flexible wall. The effect of the flexible wall was not in evidence in the pressures measured at 2- and 3-ft depths, because these pressures were the same for both walls.

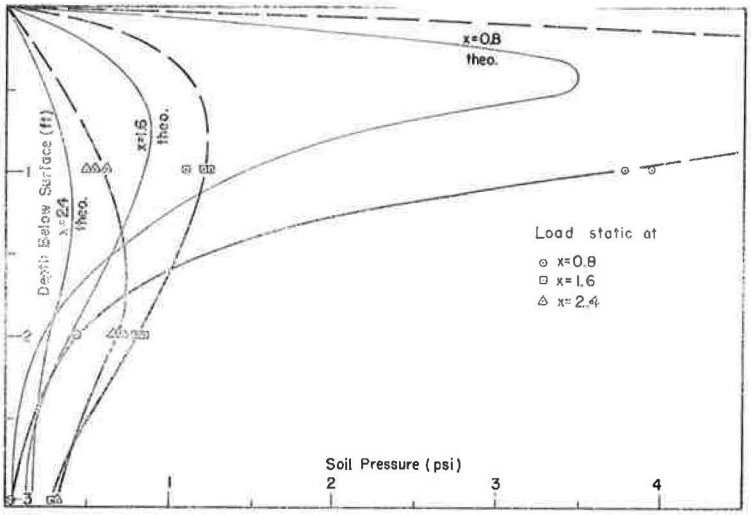

Figure 32. Soil pressure at flexible wall for different front wheel locations (sand).

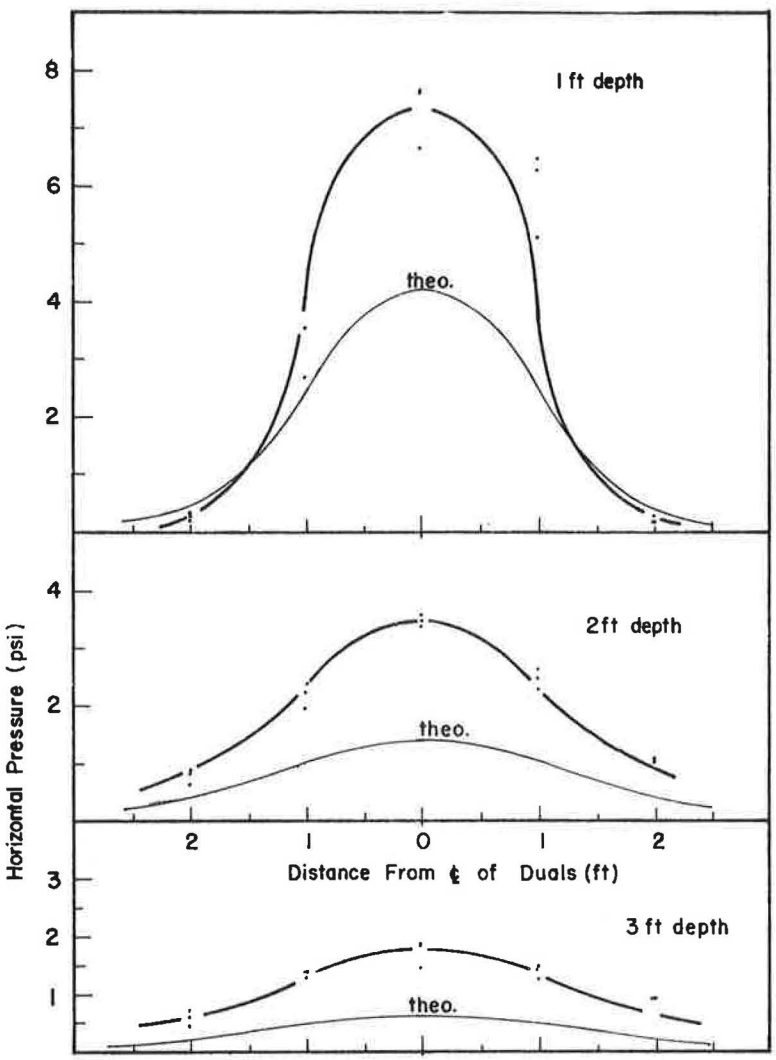

Figure 33. Distribution of lateral pressure at flexible wall for truck duals (sand).

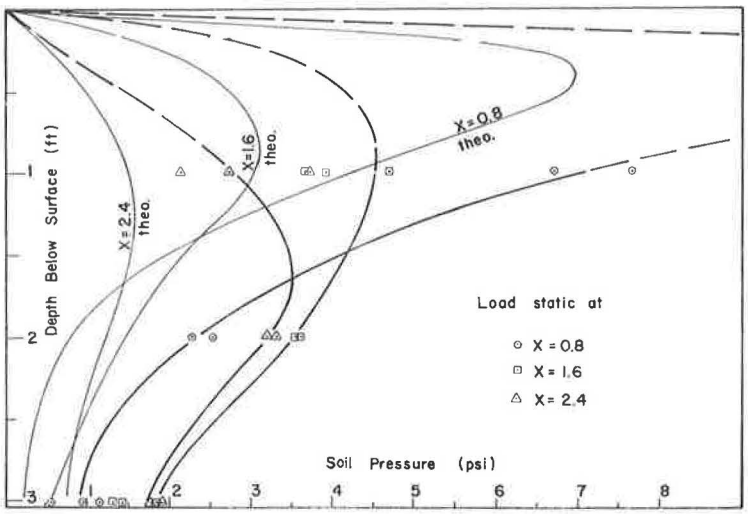

Figure 34. Soil pressure at flexible wall for different rear wheel locations (sand).

The movement of the flexible wall was found to be small. The measured deflections of the top of the wall at the point of the load were approximately 0.0005 in. for each 1,000 lb of wheel load applied at the surface of the backfill for both front and rear wheels.

Figure 32 shows the pressures against the flexible wall for different front wheel locations on the sand backfill. It is evident that the effect of movement did not alter the pressure distributions. The movement only affected the maximum pressure at the 1-ft depth.

Test Series F. —Test series F compares the pressure against the rigid wall for the rear dual tires of the truck on the sand backfill to the pressure against the flexible wall.

Figure 33 shows the distribution of lateral pressure against the flexible wall for the rear dual tires of the truck on the sand backfill. At a 1-ft depth on centerline, the experimental pressure was 179 percent of the theoretical value; at a 2-ft depth, 236 percent; and at a 3-ft depth, 232 percent.

Comparison of Figure 28 and Figure 33 shows the pressure against the rigid wall at a 1-ft depth was about 110 percent greater than the pressure at the same depth on the flexible wall. The effect of movement of the wall was not significant for the pressures measured at 2- and 3-ft depths.

Figure 34 shows the pressure against the flexible wall for different rear wheel locations on the sand backfill. The movement did not affect the pressure distributions, but only the maximum pressures.

CONCLUSIONS

The first problem investigated was that of determining the variation of pressure, measured both in the soil and at the soil-wall interface, due to variation of the soil characteristics. Test Series A and B were conducted for different wheel loads on the soil in order to determine the effect of wheel loads on the pressures created in the soil. The sand backfill tends to create greater pressure in the soil. The measured pressures in the sand backfill gave results closer to the theoretically computed values. The tendency of the sand to create greater pressure could be attributed to the fact that the sand was more uniform and was closer to being homogeneous. Series A and B show that the effect of different characteristics of the soils was predominant only to a 1-ft depth.

This phase of the investigation also included a study to determine the effect of soil characteristics on the pressures created at the soil-wall interface. The pressures

measured in Series C and D show that the sand backfill transmitted larger pressures to the wall. The resulting pressures, even though two to three times the theoretical value, were consistent at all depths.

The resulting pressure distributions for Series A through D show that the soil pressure created by the concentrated load was distributed in accordance with the elastic theory. The pressures measured in the soil were less than the theoretical values for both the native soil and the sand backfill. The pressures measured at the wall show a large stress concentration caused by the discontinuity in the soil mass due to the wall. The relatively rigid wall interrupts the lateral strains within the soil mass and hence concentrates the stresses at the plane of the back face of the wall.

The second problem investigated was that of determining the variation in soil pressure with respect to the relative rigidity of the wall construction. Test Series E and F show that the pressure in the first foot of soil against the rigid wall was higher than the pressure against the flexible wall. The pressures measured at 2- and 3-ft depths were not influenced to any degree by the wall flexibility and were of the same order of magnitude. It can be concluded that for relatively flexible abutment retaining walls, the greatest effect of the flexibility on the soil pressure will be limited to the first foot of the backfill.

ACKNOWLEDGMENTS

The subject matter of this paper was obtained as part of a research project on the "Effect of Vibration on Soil Properties" sponsored by the New Mexico State Highway Department and the U. S. Bureau of Public Roads. The cooperation and assistance of H. S. Wiley, Planning Director, and Charles W. Johnson, Assistant Chief Engineer, both of the New Mexico State Highway Department are especially appreciated. Acknowledgment is also due Dean F. Bromilow and Associate Professor N. N. Gunaji of the New Mexico State University.

REFERENCES

1. Andersen, Paul, "Substructure Analysis and Design." Ronald Press, 2nd Ed. (1956).
2. Jumikis, Alfreds R., "Soil Mechanics." D. Van Nostrand (1962).
3. Linger, Don A., "Effect of Vibration on Soil Properties." Unpublished report, Eng. Exp. Sta., New Mexico State Univ. (July 1961).
4. Peck, Ralph B., Hanson, Walter E., and Thornburn, Thomas H., "Foundation Engineering." John Wiley and Sons (1953).
5. Perry, C. C., and Lissner, H. R., "The Strain Gage Primer." McGraw-Hill (1955).
6. Sanborn Company, "Sanborn Equipment Manual." Cambridge, Mass. (1956).
7. Sowers, George B., and Sowers, George F., "Introductory Soil Mechanics and Foundations." Macmillan, 2nd Ed. (1961).
8. Spangler, M. G., "Horizontal Pressures on Retaining Walls Due to Concentrated Surface Loads." Iowa State College, Eng. Exp. Sta. Bull. 140 (1938).
9. Spangler, M. G., "Soil Engineering." International Textbook (1960).
10. Taylor, Donald W., "Fundamentals of Soil Mechanics." John Wiley and Sons (1948).
11. Timoshenko, S., "Theory of Elasticity." McGraw-Hill (1934).
12. Tschebotarioff, Gregory P., "Soil Mechanics, Foundations, and Earth Structures." McGraw-Hill (1951).
13. Weiskopf, Walter H., "Stresses in Soils Under a Foundation." J. Franklin Inst., Vol. 239, No. 6 (June 1945).
14. White, L., and Paaswell, G., "Lateral Earth and Concrete Pressures." ASCE, Vol. 65, No. 8, Part 2 (Oct. 1939).

Equations of Failure Stresses in Materials With Anisotropic Strength Parameters

M. LIVNEH and E. SHKLARSKY
Respectively, Lecturer of Civil Engineering and Associate Professor of Civil Engineering, Technion—Israel Institute of Technology

The Mohr-Coulomb equations of the failure stress and Prandtl's equation of the bearing capacity are extended to include the case of a medium with anisotropic cohesion and anisotropic angle of internal friction.

•THE RUPTURE theory conventionally applied to soils and asphaltic concretes is that of Mohr-Coulomb, according to which rupture occurs when the major (σ_1) and minor (σ_3) principal stresses determine a stress circle tangent to the strength line of the material. The latter is, at first approximation, a straight line and yields the following two strength parameters: cohesion C and angle of internal friction ϕ.

Normally these parameters are regarded as isotropic, although as previously shown (1 - 3) this is not always the case in asphaltic concretes. This is especially evident in materials where density is acquired by means of mechanical compaction, whether in the laboratory or in the field. In such compaction the compactive load is transmitted to the material in one direction only, a fact which suffices for the assumption of anisotropy of the resulting structure and hence of strength parameters as well. In these circumstances the failure force which acts parallel to the direction of compaction is greater than that perpendicular to it.

With regard to dense asphaltic concretes it was suggested (1, 2) that the anisotropy of their strength is due solely to that of the cohesion, while the friction angle remains isotropic. This assumption is reasonably accurate when the asphaltic concrete is, for example, composed of cubic aggregates. However, with aggregates of elongated shape it has been shown (3) that both the cohesion and the internal friction angle are anisotropic. This fact necessitates extension of the conventional strength theory to include the case of anisotropy of both strength parameters.

THE FUNCTION DESCRIBING THE VARIATION C AND ϕ

Theoretical calculation of the failure stresses in a material with anisotropic friction angle and cohesion necessitates knowledge of the values of the cohesion and angle of internal friction in every direction.

Where the angle of friction is isotropic and the cohesion anisotropic, a function has been proposed for this variation (2). This function, although a theoretical one, satisfies tests results which show that the cohesion has two major values: C_{max}, which comes into play when the principal stress is parallel to the direction of compaction; and C_{min}, which comes into play when it is perpendicular to the direction of compaction.

The function is:

$$C = C_{max} - \left(C_{max} - C_{min}\right) \sin^2 \bar{\psi} \tag{1a}$$

with

$$\bar{\psi} = \beta_i - \left(45° - \frac{\phi}{2}\right) = \beta_j + \left(45° - \frac{\phi}{2}\right) \tag{1b}$$

Paper sponsored by Committee on Stress Distribution in Earth Masses.

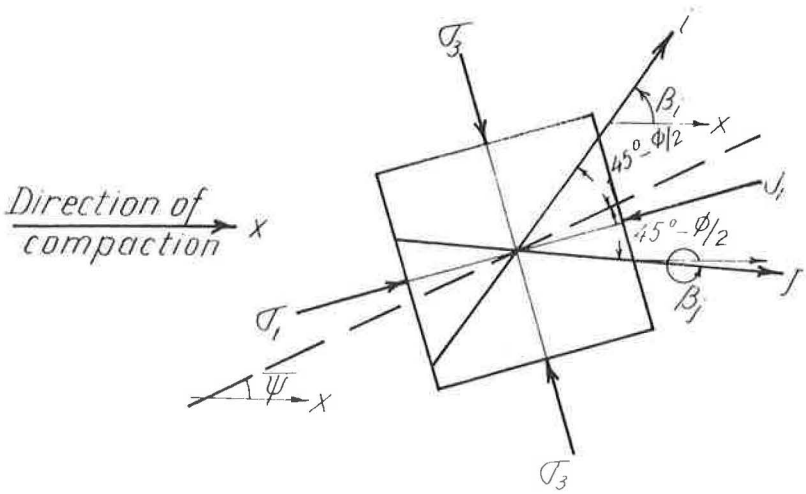

Figure 1. Slip planes in an element with anisotropic strength parameters.

β_i and β_j being the inclination of the failure planes i and j, respectively, as measured from the x-direction (that of compaction; see Fig. 1).

The above proposed function satisfies the limiting conditions. When $\bar{\psi} = 0$, i.e., the direction of the major principal stress is parallel to the direction of compaction, $C = C_{max}$. When $\bar{\psi} = 90°$, i.e., the direction of the major principal stress is perpendicular to the direction of compaction, $C = C_{min}$. For an intermediate value of $\bar{\psi}$, the cohesion has an intermediate value between C_{max} and C_{min}. The function proposed allows for only an initially small reduction in C from C_{max}, as the value of $\bar{\psi}$ increases from 0, and hence is considered to approximate the true behavior closer than another assumption such as a linear variation.

Experimental data are not yet available that define more closely the function of actual variation of C between the two extreme values.

If the value of ϕ varies with the orientation of the failure plane, a function similar to the foregoing can also be proposed:

$$\tan\phi = \tan\phi_{max} - (\tan\phi_{max} - \tan\phi_{min}) \sin^2\bar{\psi} \tag{2}$$

The relation between the maximum and minimum values of cohesion and friction may be defined as:

$$\frac{\tan\phi_{max}}{\tan\phi_{min}} = m_\phi \tag{3a}$$

$$\frac{C_{max}}{C_{min}} = m_c \tag{3b}$$

For the purpose of further development in this paper, the special case is analyzed of $m_c = m_\phi = m$. This case is represented geometrically by all strength lines originating as straight lines from a single point O′ (Fig. 2), because in this case $C \cot\phi$ is a constant independent of $\bar{\psi}$.

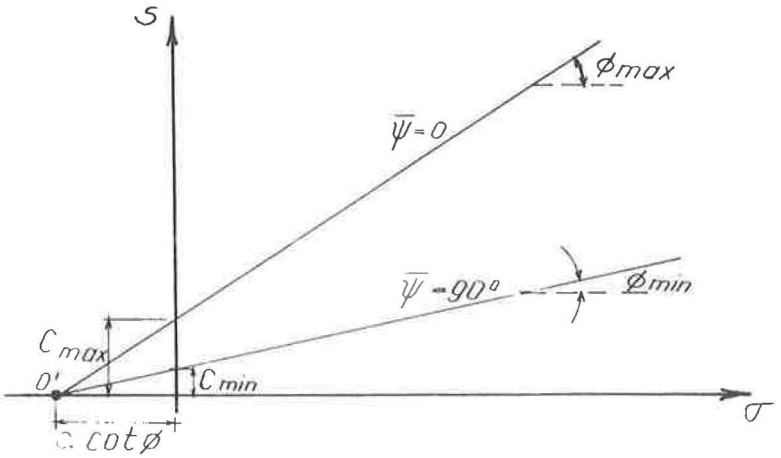

Figure 2. Strength lines diagram.

THE FAILURE STRESS EQUATIONS

The general formulation of the shear strength law for a medium with anisotropic cohesion is

$$S = C + \sigma_n \tan\phi \tag{4}$$

in which

S = the shear strength;
C = cohesion;
ϕ = angle of internal friction (dependent on the orientation of the failure plane); and
σ_n = stress perpendicular to the failure plane.

From the above law it is possible to obtain the values of σ_x, σ_y, τ_{xy} determining the state of stress of a point in plane problems. It is convenient, for this purpose, to employ Mohr's stress circle at failure of the point considered. In a Mohr circle of given radius R (Fig. 3) failure occurs in the plane in which the conditions

$$\frac{dS}{d\beta} = \frac{d\tau}{d\beta} \tag{5a}$$

$$S = \tau \tag{5b}$$

are satisfied.

However, since $\tau = R \sin 2(\beta - \psi)$, Eqs. 5a and b reduce in effect to the following:

$$\frac{dS}{d\beta} = \frac{2S}{\tan 2(\beta - \psi)} \tag{6}$$

ψ being the angle between the x-axis and the plane of the minor principal stress.

Eq. 6 prescribes the condition for the inclination of the failure plane β_i for a Mohr circle of given radius R. Geometrical representation of this equation is obtained with segment a of Figure 3 given by

$$a = \frac{1}{2}\frac{dS}{d\beta} \tag{7}$$

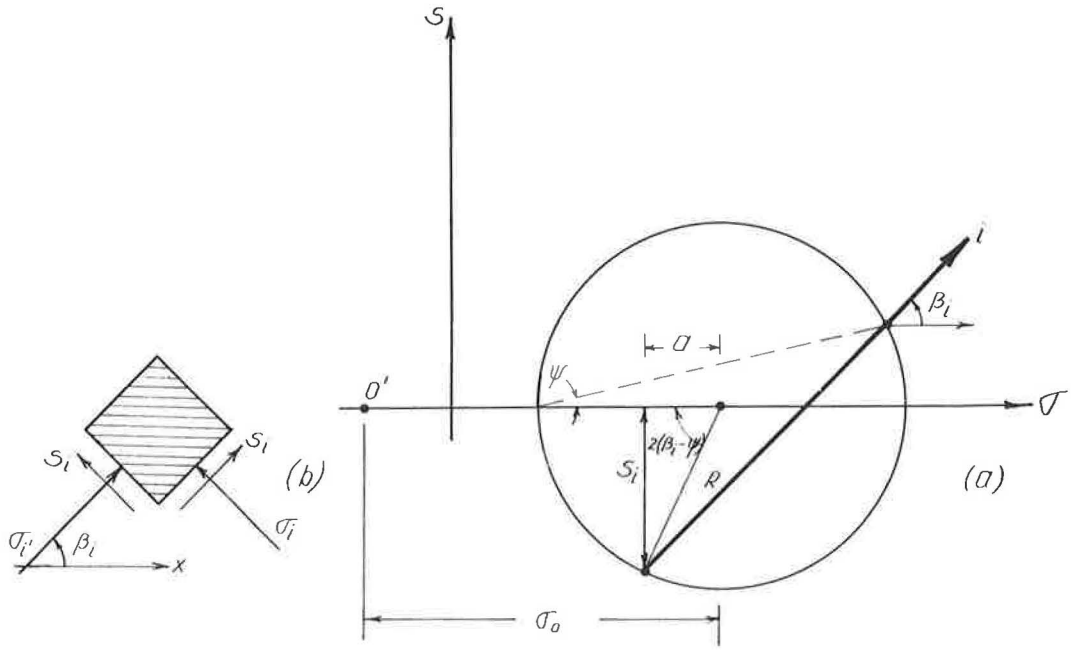

Figure 3. (a) Stress diagram; (b) stresses parallel and perpendicular to slip line direction.

In order to determine a, S must be differentiated with respect to β.

The relation between S and β is

$$S = \left[\sigma_o - R \cos 2(\beta_i - \psi) \right] \tan \phi \tag{8}$$

where σ_o represents the distance between O′ and O (see Fig. 3).

Differentiation of Eq. 8 yields

$$a = R \sin 2(\beta_i - \psi) \tan \phi + \frac{1}{2} \left[\sigma_o - R \cos (\beta_i - \psi) \right] \frac{\partial \tan \phi}{\partial \beta} \tag{9}$$

It should be borne in mind that in Eq. 8, σ_o is independent of β since, as already shown, C cot ϕ is constant.

The Mohr circle also gives the relation

$$\sigma_o - R \cos 2(\beta_i - \psi) = \sigma_o - a \tag{10}$$

and substitution in Eq. 9 yields

$$a = (\sigma_o - a) \tan^2 \phi + (\sigma_o - a) \frac{\partial \tan \phi}{2 \partial \beta} \tag{11}$$

or finally

$$a = \sigma_o \sin^2 \phi - f \sigma_o \cos^2 \phi \tag{12a}$$

where

$$f = -\frac{\partial \tan\phi}{2\partial\bar{\psi}} \cdot \frac{1}{1+\tan^2\phi} = -\frac{\partial\phi}{2\partial\bar{\psi}} \tag{12b}$$

Eq. 12 already includes the substitution

$$\frac{\partial \tan\phi}{\partial\bar{\psi}} = \frac{\partial \tan\phi}{\partial\beta}\left(1 - \frac{\partial\phi}{2\partial\bar{\psi}}\right) \tag{13}$$

Now, with a known, the stresses can be calculated. The Mohr circle diagram shows that the stresses respectively parallel and perpendicular to the failure plane i (Fig. 3) are:

$$\sigma_i = \sigma_o - C\cot\phi + a \tag{14a}$$

$$\sigma_{i'} = \sigma_o - C\cot\phi - a \tag{14b}$$

$$\tau_i = -(\sigma_o - a)\tan\phi \tag{14c}$$

Rotating the axes from i/i′ to x/y, and substituting a from Eq. 12 the failure stresses σ_x, σ_y, τ_{xy} are obtained as follows:

$$\sigma_x = \sigma_o\,(1 + \sin\phi\cos 2\bar{\psi}) + \sigma_o f \sin 2\bar{\psi}\cos\phi - C\cot\phi \tag{15a}$$

$$\sigma_y = \sigma_o\,(1 - \sin\phi\cos 2\bar{\psi}) - \sigma_o f \sin 2\bar{\psi}\cos\phi - C\cot\phi \tag{15b}$$

$$\tau_{xy} = \sigma_o \sin\phi\sin 2\bar{\psi} - \sigma_o f\cos 2\bar{\psi}\cos\phi \tag{15c}$$

It should be borne in mind that in these equations ϕ is a function of $\bar{\psi}$ according to Eq. 2. When ϕ and C are constant, $f = 0$ and Eqs. 15 are identical with their conventional counterparts for the case of isotropic strength parameters. Finally, it should be noted that Eqs. 15 refer to the case of two-dimensional state of stress with the direction of compaction parallel to the x-axis.

MOHR CIRCLE REPRESENTATION

This section deals with the geometry of the Mohr circle at failure of a material with anisotropic strength parameters. In this circle (Fig. 4) PA is the failure plane, i.e., at A the shearing stress equals the shear strength so that the angle AO′O equals ϕ for the given $\bar{\psi}$.

Using Eq. 15, it can be proved that

$$\overline{DP} = \sigma_o f\cos\phi\sin 2\bar{\psi} \tag{16a}$$

$$\overline{HD} = \sigma_o f\cos\phi\cos 2\bar{\psi} \tag{16b}$$

where in triangle OHP we have

$$\overline{OH} = \overline{OB} = \overline{O'O}\sin\phi \tag{17a}$$

$$\hat{POH} = 2\bar{\psi} \tag{17b}$$

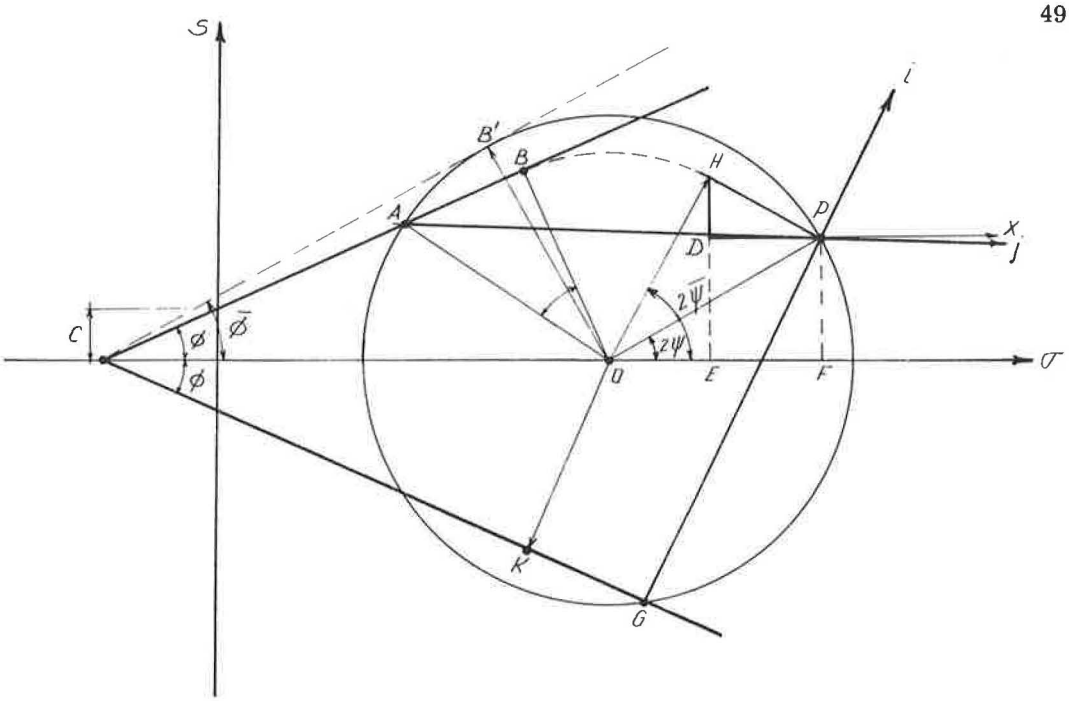

Figure 4. Mohr circle for anisotropic strength parameters.

$$O\hat{H}P = 90° \tag{17c}$$

hence

$$\overline{HP} = \sigma_O f \cos \phi \tag{18}$$

Triangles OHG and DAB are congruent, hence

$$O\hat{A}B = 2(\psi - \bar{\psi}) \tag{19}$$

and

$$\overline{AB} = \sigma_O f \cos \phi \tag{20}$$

hence

$$\frac{\overline{AB}}{\overline{O'B}} = f \tag{21}$$

Obviously, when $f = 0$, A coincides with B, but when $f \neq 0$ the failure circle is tangent not to the strength line O'A but to another line originating in O', its inclination $\bar{\phi}$ being given by

$$\sin \bar{\phi} = \frac{\overline{OB'}}{\overline{O'O}} = \frac{\sin \phi}{\cos 2(\psi - \bar{\psi})} \tag{22a}$$

or

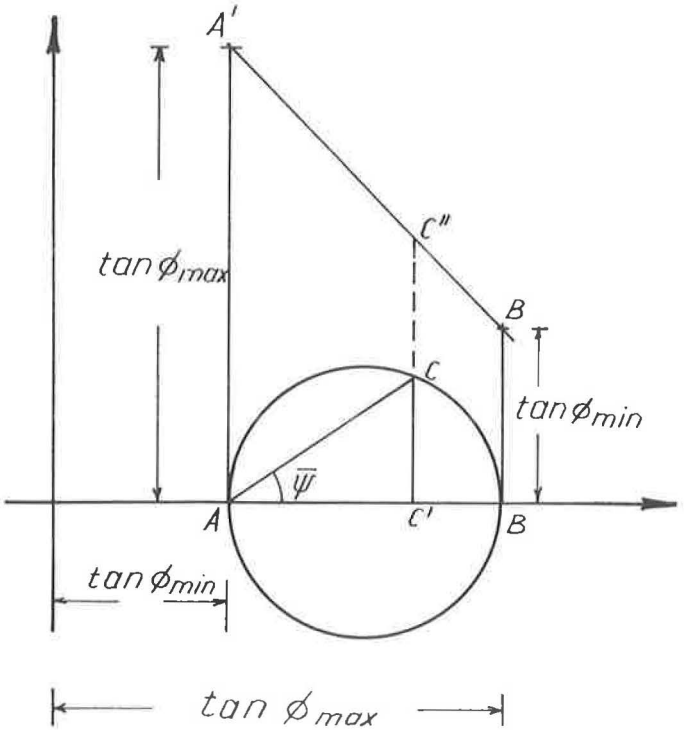

Figure 5. Graphical determination of tanφ and ∂tanφ/2∂ψ̄.

$$\sin \bar{\phi} = \sqrt{\sin^2 \phi + f^2 \cos^2 \phi} \tag{22b}$$

Clearly this failure circle contains a second failure plane, namely the segment $\overline{GP}$, for APC = 90° - ϕ. Previous derivations show that here again

$$\frac{\overline{KG}}{\overline{O'K}} = f \tag{23}$$

To sum up, a graphical method is given for calculating tan ϕ and $-\frac{\partial \tan \phi}{2 \partial \bar{\psi}}$ which yields the expression for f. To accomplish this, a circle of diameter AB = tan ϕ_{max} - tan ϕ_{min} (Fig. 5) is drawn. A perpendicular BB′ = tan ϕ_{max} is raised at B and a perpendicular AA′ = tan ϕ_{min} at A. The straight line A′B′ and circle represent the function for tan ϕ and $-\frac{\partial \tan \phi}{2 \partial \bar{\psi}}$, as follows: from A an inclined line is drawn for the given value of $\bar{\psi}$. CC″ is then the required value of tan ϕ and C′C″ that of $-\frac{\partial \tan \phi}{2 \partial \bar{\psi}}$.

FORMULA OF BEARING CAPACITY

In routine laboratory tests, C and ϕ are determined at $\bar{\psi}$ = 0, thus generally yielding C_{max} and ϕ_{max} for a material with anisotropic strength parameters. To calculate the bearing capacity, these values are substituted in Prandtl's formula. This substitution

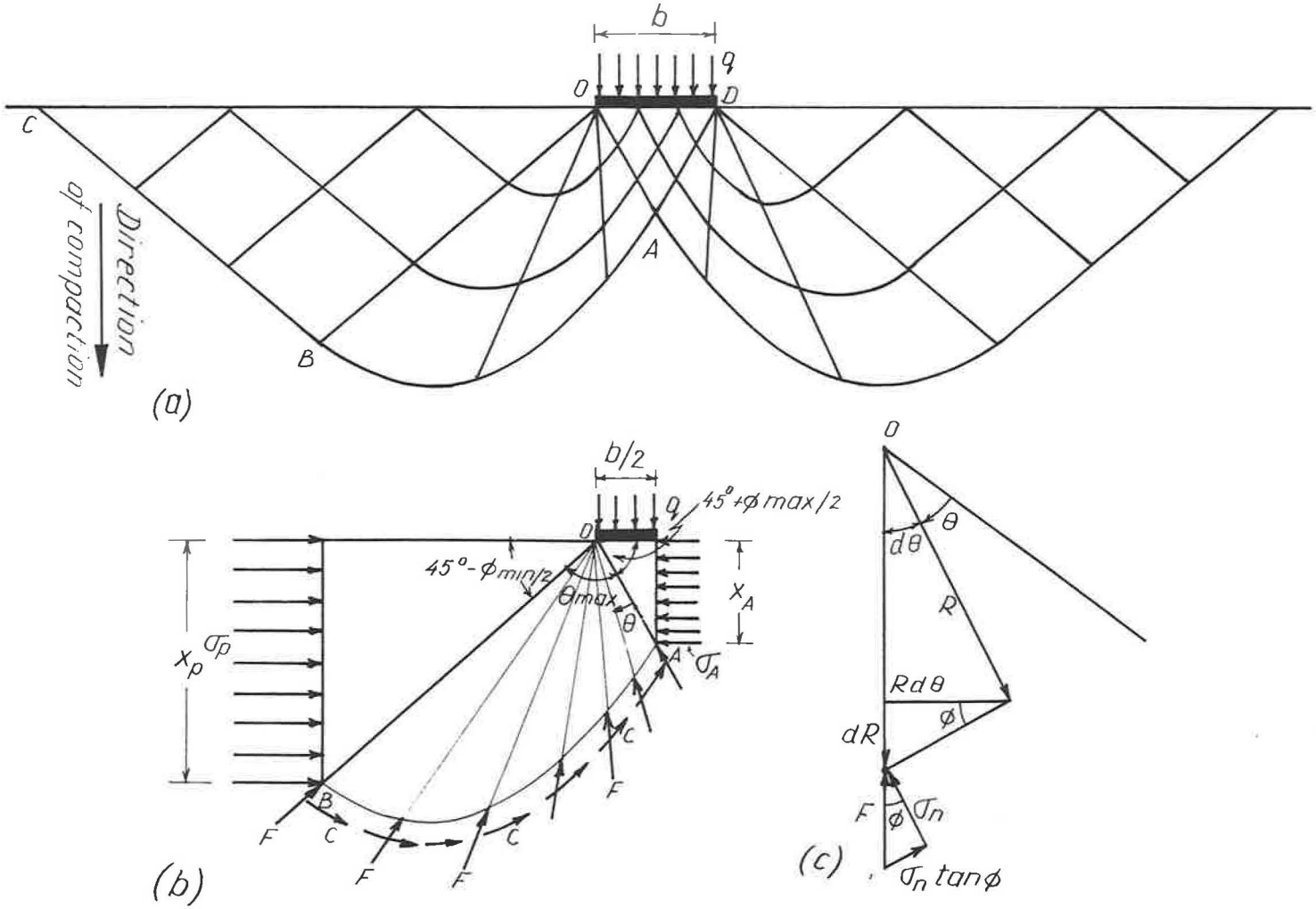

Figure 6. Rupture mechanism for bearing capacity determination.

yields correct results so long as the C and ϕ are isotropic; otherwise, the actual bearing capacity is smaller than the obtained value.

The equations for the anisotropy case are derived below, and demonstrate how important it is to ascertain, prior to calculation, whether the strength parameters are isotropic or anisotropic.

The failure mechanism for this case is shown in Figure 6a, with the direction of compaction parallel to the unit bearing load q. The mechanism consists of (a) triangle OAD, a region of active Rankine shear with angle OAD = 90° - ϕ_{max}; (b) triangle CBO, a region of passive Rankine shear with angle CBO = 90° + ϕ_{min}; (c) sector OAB, a region of radial shear with:

$$\frac{dR}{R d\theta} = \tan \phi \tag{24a}$$

$$\theta = \phi/2 - \phi_{max}/2 + \bar{\psi} \tag{24b}$$

where R is the radius vector of the failure lines in this latter region. Eq. 24 insures that the resultant of σ_n and $\sigma_n \tan \phi$ (Fig. 6c) in this region passes through O, as in the case of Prandtl's mechanism.

Eq. 24 leads to the following expression for the radius vector in the radial shear region:

$$R = R_o \exp\left\{\left[\tan \phi_{max} + \tan \phi_{min}\right]\frac{\bar{\psi}}{2} + \left[\tan \phi_{max} - \tan \phi_{min}\right]\frac{\sin 2\bar{\psi}}{4} + \left[\tan^2 \phi - \tan^2 \phi_{max}\right]\frac{1}{4}\right\} \tag{25}$$

where R_o is represented by segment OA in Figure 6a. To find the bearing capacity q, moments are equated about O. The stresses producing moments about O are (see Fig. 6b): σ_A—the active stress, σ_P—the passive stress, the cohesion C along BA (σ_n and $\sigma_n \tan \phi$ along AB do not produce moments about O, since their resultant passes through it), and the bearing capacity q is thus:

$$\sigma_P \frac{x_P^2}{2} + \int_o^{\theta_{max}} C R^2 \, d\theta = \frac{qb^2}{8} + \sigma_A \cdot \frac{x_A^2}{2} \tag{26a}$$

according to Eq. 13, σ_A is given by σ_y for $\bar{\psi} = 0$ and $q = \sigma_1$, i.e.,

$$\sigma_A = q\frac{1 - \sin \phi_{max}}{1 + \sin \phi_{max}} - \frac{2 C_{max} \cos \phi_{max}}{1 + \sin \phi_{max}} \tag{26b}$$

Similarly, σ_P is given by σ_x for $\bar{\psi} = 90°$ and $\sigma_3 = 0$

$$\sigma_P = \frac{2 C_{min} \cos \phi_{min}}{1 - \sin \phi_{min}} \tag{26c}$$

and substitution and integration yields

$$q = \bar{N}_c \cdot C_{max} \tag{27a}$$

where

$$1 + \frac{\bar{N}_c}{\cot \phi_{max}} = \left\{ \left[\frac{\sin \phi_{min}}{1 - \sin \phi_{min}} + \frac{1}{1 - \sin \phi_{max}} \right] \right.$$

$$\left. \exp\left[\frac{\pi}{2} \left(\tan \phi_{max} + \tan \phi_{min} \right) - \frac{1}{2} \left(\tan^2 \phi_{max} - \tan^2 \phi_{min} \right) \right] \right\} \tag{27b}$$

The factor $\bar{N}_c$ can also be given as:

$$\bar{N}_c = F \cdot N_c \tag{28}$$

where N_c is the bearing factor for a material with isotropic strength parameters, and F a reduction factor accounting for the effect of anisotropic strength. F is plotted in

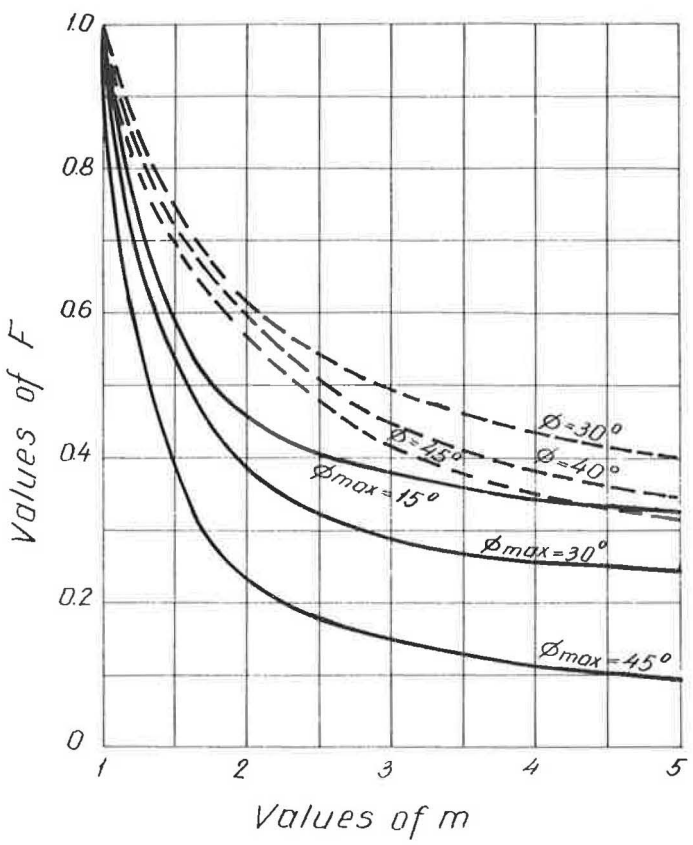

Figure 7. Reduction factor F vs anisotropic strength factor m.

Figure 7 (solid lines) against m for different values of ϕ_{max}; the dashed lines represent the case of anisotropic cohesion and isotropic friction angle (4). Figure 7 shows that the anisotropy effect is decisive, hence the need for ascertaining it. For example, for $\phi_{max} = 45°$ and $m = 3$, F is 0.15; hence disregard of possible anisotropy will in this case lead to six-fold overestimation of the bearing capacity compared with the result when m is taken into account. Obviously, F will always be smaller in the case of anisotropy of both parameters, compared with its value when the cohesion is anisotropic and the angle of friction isotropic.

CONCLUSIONS

1. The failure stress equation for the case of anisotropic strength parameters involves the term $\partial \phi / \partial \bar{\psi}$; when this term equals zero the equations become identical to the conventional ones.
2. In the case of anisotropic strength parameters the Mohr circle at failure is not tangent to the strength line defined by $S = C + \sigma \tan \phi$.
3. The bearing capacity of materials with anisotropic strength parameters is very much affected by the value of the anisotropic strength factor.

REFERENCES

1. Shklarsky, E., and Livneh, M. The Anisotropic Strength of Asphaltic Paving Mixtures. Bull. Res. Counc. of Israel 9C, (4), 183, 1961.
2. Livneh, M., and Shklarsky, E. The Splitting Test for Determination of Bituminous Concrete Strength. Proc. AAPT 31, 1962.
3. Hennes, R. G., and Wang, C. C. Physical Interpretation of Triaxial Test. Proc. AAPT 20, 180, 1951.
4. Livneh, M., and Shklarsky, E. The Bearing Capacity of Asphaltic-Concrete Carpets. Int. Conf. on Structural Design of Asphalt Pavements, University of Michigan, 1962.

Computer Solution for Settlement of Foundations

R. M. K. WONG and L. D. GRAVES
Teaching Assistant and Associate Professor, Department of Civil Engineering, University of Notre Dame

Modern complex structures with heavy loadings require a detailed analysis of the differential settlements to be expected because of soil consolidation. However, the accurate calculation of such settlements considering variable soil properties and many loaded points is a laborious and time-consuming job. It was decided to develop a digital computer solution which would be based on the one-dimensional consolidation theory and the elastic theory of stress distribution but would still take into account the variation in soil properties and the complexity of many loading conditions.

The mathematical integration of the expression developed to predict settlement is very difficult because the stress-strain relation in soil is nonlinear, there is no general relation between the pressure at a point in soil and the many loads that cause the pressure, and both the initial and final pressures are variables. To overcome these difficulties, a numerical modified Euler method was used. A flow diagram and a specific FORTRAN language instruction for the IBM 1620 computer were prepared and typical differential settlement problems were solved. The settlements obtained compared favorably with experimental results. The time involved to execute a program depends on the computer speed, the number of loads, thickness of soil layer and the increment of thickness selected. The computer solution compares favorably in cost, accuracy and speed with other calculation methods. The greater the complexity of the structure, the better is the comparison.

•A STRUCTURE usually rests on soil and the load which is transmitted by the foundations will cause the soil to undergo compressive strains resulting in the settlement of the structure. Therefore, the stress-strain characteristics of the foundation soil must be studied to understand the behavior of the structure and to predict with a fair degree of accuracy the probable settlement during the life of the structure, so that suitable provisions may be made to take care of the settlement.

Settlement of itself does not affect a structure adversely. In fact, all structures, with the exception of those whose foundation reactions are transmitted to solid rock, will settle to a greater or lesser extent. As long as settlement is uniform throughout the loading plan of a structure and it does not reach excessive proportions, one does not have to fear the possible failure or malfunction of the structure. But if the settlement is uneven, i.e., if one corner of a building or one end of a structure settles more than the others, serious consequences may ensue. The progressive buildup of unequal settlements may eventually result in overturning or leaning of the structure. In some cases, the integrity of the framework may be destroyed. Unequal settlement may also cause serious overstress in some members and subject the structure to a loading pattern not provided for in the original design, thus making the structure dangerously unstable or unsafe.

From the foregoing discussion, it is evident that the most important effect of settlement is not the total magnitude of settlement which the structure may undergo but the

Paper sponsored by Committee on Stress Distribution in Earth Masses.

differential settlement of various portions of the structure and the resulting distribution of pressures on the soil and of the foundation reactions on the structure. It is, therefore, essential to develop a method to analyze the distribution of settlement of the loading plan of a structure. Once this distribution of settlement is known, suitable measures can be taken to guard against serious consequences. Alternatively, the loading plan may have to be radically changed.

For a comparatively simple structure, the evaluation of the distribution of settlements does not present any difficulties. But complex structures of the types gaining in popularity in the modern age require a lengthy computational procedure which would almost invariably involve computation errors. When dealing with complex structures, one cannot afford the luxury of a mistake. Therefore, it is both expedient and necessary to carry out the computations with an electronic computer. The present study develops a method of analysis which enables the computation of the distribution of settlements through a digital computer program.

SCOPE

Settlement is affected by the pressure distribution within the soil mass. The solution presented here is based on an original idea by Stoll (4) and on the consolidation theory developed by Terzaghi to explain the compression of soil under structural loads. Several consolidation theories have been published but to include all theories along with complex soil properties would make the problem unnecessarily long. However, for the one consolidation theory, the study does consider the process of evaluating settlements in soils with variable properties.

THEORETICAL ANALYSIS OF SETTLEMENT

Settlement of a structure resting on soil may be caused by two main types of action within the foundation soil. The first is a shearing failure within the soil mass. This causes the soil mass to slide downwards and laterally, and the structure settles and may even tip out of vertical alignment. This kind of settlement, caused by the failure in bearing capacity of soil, is usually developed suddenly and rapidly. Its amount is not predictable and can not be allowed for in the design of foundations. Therefore, this kind of settlement will not be discussed here.

In the second type, a structure settles by virtue of the compressive stress and the accompanying strains developed in the soil by the load imposed on it without failure of the soil. This kind of settlement, caused by the reduction in volume of a soil mass resulting from the application of a foundation load and the accompanying compressive stress and strain, is called consolidation. This will be considered as the major part of settlement in this study.

Because the soil mass lies beneath a limited horizontal plane surface and extends to an infinite distance in all directions below that plane, it is considered as a semi-infinite solid. The transmission of surface load into the subsoil will produce vertical, horizontal, radial and shearing stresses within the soil mass. The volume change of soil mass may be caused by the combined effects of vertical consolidation due to vertical pressure and upward displacement due to lateral pressure and shearing stresses. But in the soil masses in the soil column directly under the loaded area (Fig. 1), the vertical stress is much greater than the other stresses. Therefore, the effect of the settlement component due to the vertical consolidation usually predominates in comparison to the others, except for soils such as very soft clays which are weak in shearing resistance and easily displaced like a viscous fluid. For that reason, settlement due to the volume changes in a soil mass resulting from the application of foundation loads and the accompanying compressive stress and strain may be assumed to be in the vertical direction only.

Based on this assumption, the settlement S in a soil column in a homogeneous soil layer of thickness H directly under a single load P, as shown in Figure 1, is equal to the sum of the vertical compressive strains in the successive horizontal layers of thickness dZ due to the vertical pressure transmitted by P:

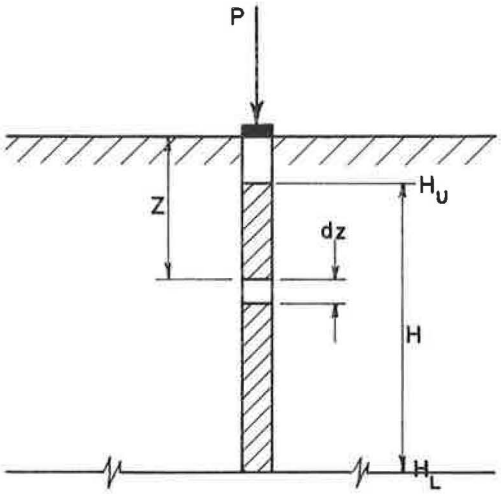

Figure 1. Soil column under single load.

$$S = \int_{H_u}^{H_\ell} \epsilon \, dZ \tag{1}$$

in which

ϵ = unit strain for a layer dZ at depth Z below loaded area,
H_u = upper boundary of soil layer, and
H_ℓ = lower boundary of soil layer.

Because soil is porous material containing a large proportion of void space, the strain due to volume change in soil actually corresponds to a decrease in void space, although there may be a negligible compression of water in the soil and of soil grains at their points of contact due to intergranular pressure. The unit strain ϵ may, therefore, be expressed in terms of the change of void ratio:

$$\epsilon = \frac{\Delta e}{1 + e} \tag{2}$$

in which

e = original or known void ratio,
Δe = change of void ratio, and
1 + e = total volume of soil.

The character of the change of void ratio for most soil in consolidation tests is such that the curve of void ratio vs pressure plotted on a semilogarithmic paper, as shown in Figure 2, is almost a straight line, and its slop C_c, the compression index, is a constant. By this relationship, the change of void ratio may be written in terms of pressure as:

$$\begin{aligned} \Delta e &= C_c \Delta \log P \\ &= C_c (\log T - \log B) \\ &= C_c \log \frac{T}{B} \\ &= C_c \log \left(\frac{B + V}{B}\right) \\ &= C \log \left(1 + \frac{V}{B}\right) \end{aligned} \tag{3}$$

in which B is existing overburden pressure before surface load is applied and T is total pressure equal to B plus the additional vertical pressure transmitted by P.

The magnitude of vertical pressure transmitted by the surface load depends on the relative location of the point of loading and the stressed point in the subsoil, and is governed by the transmission factor, A:

$$V = A \cdot P \tag{4a}$$

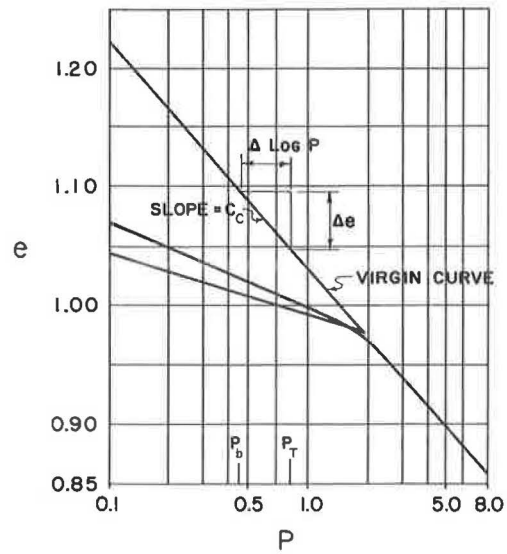

Figure 2. Idealized void ratio vs pressure curve.

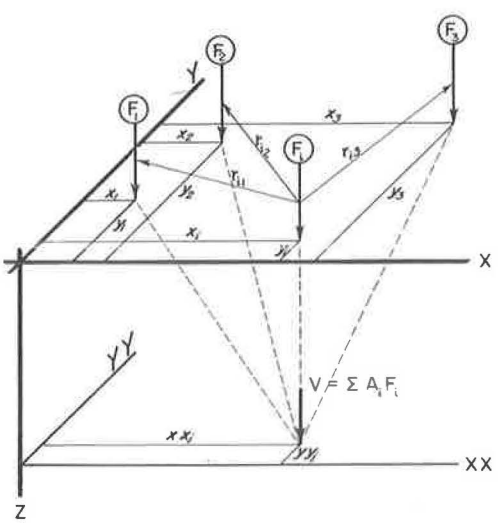

Figure 3. Transmission of surface load.

in which

j = number of calculating point,
k = number of increment, and
i = number of point load.

Since Eq. 4a considers one point load only, if there are n point loads at the surface, as shown in Figure 3, the vertical pressure is then equal to

$$V = \sum_{i=1}^{n} A_i P_i = 1 \ldots \qquad (4b)$$

By combining Eq. 1 with the relationships expressed by Eqs. 2, 3, 4a, and 4b, we obtain for settlement due to one surface load:

$$S = \int_{H_u}^{H_\ell} \frac{C_c}{1+e} \log \left(1 + \frac{A \cdot P}{B}\right) dZ \qquad (5a)$$

or for settlement due to a combination of surface loads:

$$S = \int_{H_u}^{H_\ell} \frac{C_c}{1+e} \times \log \left(1 + \frac{\sum_{i=1}^{n} A_i P_i}{B}\right) dZ \qquad (5b)$$

Because of the multiplicity of loads and the nonlinear character of the transmitting factor, numerical methods have to be used to evaluate the equations and the modified Euler method was adopted. The basic assumption of this method is the approximation that the unit strain at the mid-depth of a small increment of thickness ΔZ is the mean value of unit strain for that layer. Eq. 4b is then rewritten as

$$S_j = \sum_{k=1}^{\ell} \frac{C_c}{1+e} \times \log \left(1 + \frac{\sum_{i=1}^{n} A_{jki} P_i}{B_{jk}}\right) \Delta Z \qquad (6)$$

TRANSMITTING FACTORS

Some equations developed to determine the transmitting factors are as follows:

1. Boussinesq equation for a point load applied to a homogeneous isotropic semi-infinite elastic mass:

$$A = \frac{3}{2\pi} Z^3 (r^2 + Z^2)^{-5/2} \tag{7}$$

2. Westergaard equation for point load applied to a horizontal layer of an elastic mass infinitely rigid in the horizontal direction:

$$A = \frac{1}{2\pi} \left[1 + 2 \left(\frac{r}{Z} \right)^2 \right]^{-3/2} \tag{8}$$

3. Steinbrenner equations for a uniformly loaded area with unit load P for rectangular loading area (calculating point at center):

$$A = \frac{2}{\pi} \left\{ \arctan \left[\frac{b'}{Z} \; \frac{a'(a'^2 + b'^2) - 2a'Z(R' - Z)}{(a'^2 + b'^2)(R' - Z) - Z(R' - Z)^2} \right] + \frac{a'b'Z(R'^2 + Z^2)}{(b'^2 + Z^2)(a'^2 + Z^2) R'} \right\} \tag{9}$$

in which

$a' = 1/2$ of width a,
$b' = 1/2$ of length b, and
$R' = \sqrt{a^2 + b^2 + c^2}$;

and for circular loading area (calculating point at center):

$$A = 1 - \left(\frac{1}{1 + \frac{R^2}{Z^2}} \right)^{3/2} \tag{10}$$

in which R is radius of circular section. These equations, when properly applied, will serve reasonably well to determine the vertical pressure in the subsoil. A mistake in the selection of the transmitting factor will cause a great error in the computation. For example, when the calculating point is directly under the loading point, for which the horizontal distance r is equal to zero in both the Boussinesq and Westergaard equations, the transmitting factors are infinity as the depth Z approaches zero. This may be explained by the fact that a point load is not really a point load but a load distributed over a certain area. Therefore, when the calculating point lies directly under the loading point, the transmitting factor of a distributed surface load should be taken into consideration instead of a point load.

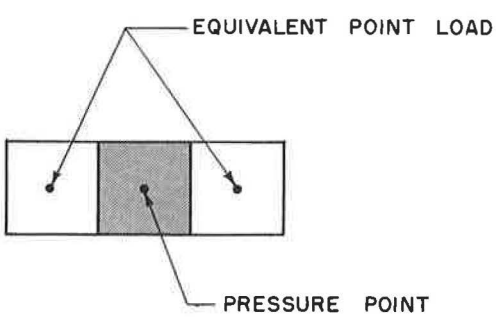

Figure 4. Assumed loading.

Because the transmitting factor equation for a rectangular loaded area is rather complicated, the authors suggest the use of the equation for a circular section having an equivalent area of the rectangular section. If the width and length are greatly different, we can divide the area into several approximately square sections, as shown in Figure 4, and consider the section above the calculating point as a distributed loaded area and the others as point loads. The difference between the transmitting factor for a square section and that for a circular section is very small.

The final expression for the transmitting factor shown in Eq. 6 is written as follows for a point load:

$$A_{jki} = \frac{3}{2\pi} Z_{jk}^3 \left[1 + \left(\frac{r_{jk}}{Z_{jk}} \right)^2 \right]^{-5/2} \quad \text{(Boussinesq)} \tag{11}$$

or

$$A_{jki} = \frac{1}{2\pi} \left[1 + 2 \left(\frac{r_{ji}}{Z_{jk}} \right)^2 \right]^{-3/2} \quad \text{(Westergaard)} \tag{12}$$

when $r_{ji} \neq 0$; and for a distributed load:

$$A_{jki} = \left[1 - \left(\frac{1}{1 + \left(\frac{R_{ji}}{Z_{jk}} \right)^2} \right)^{3/2} \right] \tag{13}$$

as $R_{ji} = 0$

EXISTING OVERBURDEN PRESSURE

The existing overburden pressure at any point of the subsoil may be expressed in the form

$$B_{jk} = B_j (k - 1) + G\Delta Z \tag{14}$$

in which

$B_j (k - 1)$ = existing pressure above the increment layer dZ, and
G = effective unit weight of subsoil.

It should be noted that the existing overburden pressure at the loading surface is not zero but is equal to the weight of soil excavated. The effective unit weight is equal to the submerged weight if the subsoil is under the water table.

SIGNIFICANT ACTING PRESSURE

The vertical pressure transmitted down to the horizontal planes in the subsoil, as shown in Figure 5, would normally spread out with depth. Thus, the increase of the horizontal distance from the point of application of load will result in decreased magnitude of the vertical pressure. The increment of vertical pressure at the point such that r/Z is greater than 2 is very small. Therefore, the surface loads located beyond the horizontal distances greater than 2Z need not be taken into account.

If the subsoil layer extends to a great depth, the compressive strains will vanish when the vertical pressure is very small compared to the overburden pressure. It is, therefore, generally safe to assume that stress due to boundary loading is no longer significant in regard to settlement when it is less than 10 percent of the existing overburden pressure, except in formations which have a presumptive bearing capacity of zero.

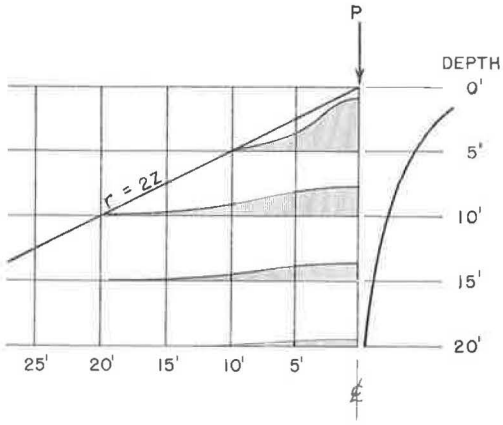

Figure 5. Vertical stress distribution on horizontal planes.

TABLE 1

LOADING DATA FOR COMPUTER

NN	F (lb)	P (psf)	X (ft)	Y (ft)
1	48000	3000	0	20
2	48000	3000	0	20
3	56000	3500	20	20
4	56000	3500	20	0

DEVELOPMENT OF COMPUTER PROGRAM

Because the magnitude of settlement is dependent on the magnitude of surface load, its point location, and the properties of the soil between the surface and the point at which the settlement is required, all these data must be listed before proceeding with the program.

The first step is to obtain the loading data, which include the magnitude of point loads, the average unit contact pressure of point load foundations, and the location of the point loads. Each individual foundation is treated as a single point if its shape is approximately square or circular or if the loaded area is not too large; otherwise, the loaded area is divided into shapes as described previously. As soon as the point loads are decided, the relative location of point loads may be determined by laying out rectangular coordinates on horizontal planes, as shown in Figure 3. The coordinate values are assigned to each point load to signify the position of the point from left to right and from top to bottom. For convenience in the work, a tabular form is set up as shown in Table 1.

The second step is to decide on the points at which settlement computations are required. The procedure for locating these points is the same as for the point loads. The soil properties in the different layers, such as void ratio, unit effective weight, compression index and the upper

TABLE 2

SOIL DATA FOR COMPUTER

MM	XX (ft)	YY (ft)	BS (psf)	LN	G (pcf)	E	C	H_u (ft)	H_ℓ (ft)
1	0.0	20	500	1	100	0.95	0.05	0	6
				2	110	0.81	0.04	6	12
				3	60	0.81	0.04	12	18
				4	50	0.90	0.05	18	26
				5	42	0.86	0.05	26	32
2	0.0	0	0	1	100	0.95	0.05	0	6
				2	110	0.81	0.04	6	12
				3	60	0.81	0.04	12	18
				4	50	0.90	0.05	18	26
				5	42	0.86	0.05	26	32

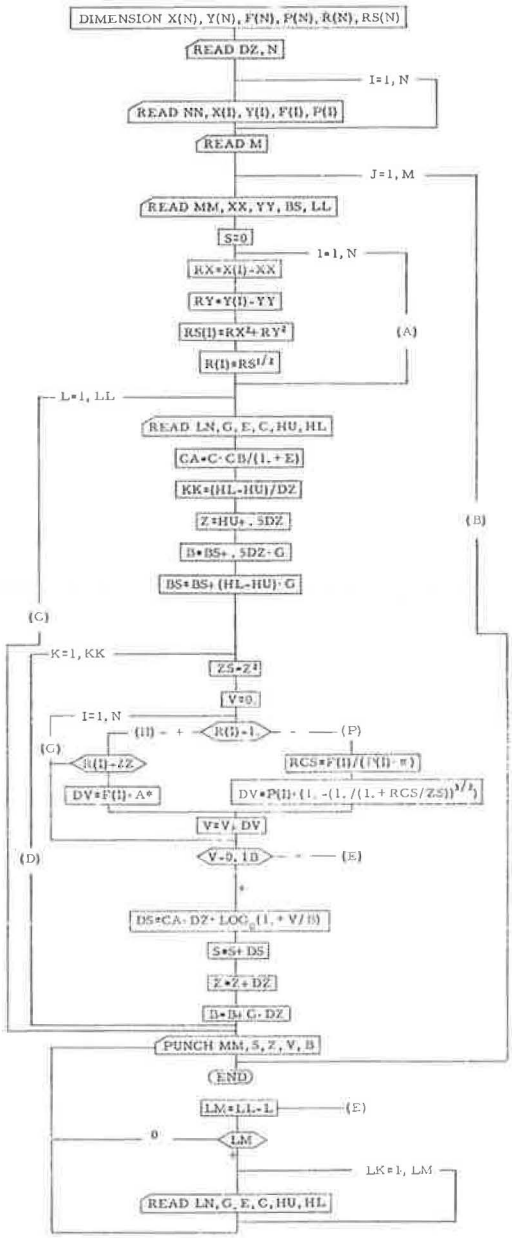

Figure 6. Flow diagram.

and lower boundary of the soil layer, should be provided in proper order, layer to layer, from the surface to the required depth. These may be listed as shown in Table 2.

FLOW DIAGRAM

Using Eq. 6, flow diagram is constructed as shown in Figure 6. The specific FORTRAN language program is given in Appendix B and the symbols used are defined in Appendix A. The procedures of the program are shown in the flow diagram, but some of the statements, which might be easily confused, are explained as follows.

In Section D when V - 0.1B is negative, the settlement at this point is not significant and there is no need of further calculations; the program then will be shifted to Section E where the computer checks how many data cards for this calculation point are left, reads all of them, then jumps to the next calculation point.

In Section G when R(I) - 1.0 is negative, R(I) is approaching zero. The point load is treated as a distributed loading area, and the program goes to Section P. Otherwise the progression is to Section H.

In Section H when R(I) - 2Z is positive, the load on the surface has no effect on this point and there is no need to calculate the vertical pressure at this point. The program goes back to Section G.

SAMPLE PROBLEMS

The settlement pattern for a building in Brazil was computed using the program developed and an IBM 1620 computer. Details of the solution are given in Appendix C. The problem involved 33 loaded points on a soil having two layers with a total depth of 55 ft. Settlements were computed for each 1-ft increment of depth. The computer time used was 2.5 hr.

Another problem was solved for 16 loaded points and a single 30-ft layer of soil using both a 1- and a 0.1-ft increment for calculating settlements. The computer time used was 10 min for the 1-ft increment and 100 min for the 0.1-ft increment. The difference between the total settlements in each case was only about 5 percent.

CONCLUSIONS

The settlements obtained by the computer solution have been compared with some observed settlements and are found to be in reasonable agreement with the actual settlements (Appendix C). The computer solution avoids computation errors which might occur if these lengthy computations are made in another manner. The solution can be used for complex or simple structures.

The time required to execute the program is dependent on the computer speed, the number of loads, thickness of soil layer and the increment dZ selected. However, the computer solution compares very favorably in cost, accuracy and speed with any of the other methods that might be used. The greater the complexity of structures, the better is the comparison.

REFERENCES

1. Griffith, J. A. Pressure Under Substructures. Engineering and Contracting, March 1929.
2. Hough, B. K. Basic Soils Engineering. Ronald Press Co., 1957.
3. Spangler, S. G. Soil Engineering. New York, International Textbook Co.
4. Stoll, U. W. Computer Solution of Pressure Distribution Problem. Jour. Soil Mechanics and Foundations Div., ASCE, Vol. 86, No. SM6, Dec. 1960.
5. Terzaghi, K., and Peck, R. B. Soil Mechanics in Engineering Practice. New York, John Wiley and Sons, 1948.
6. Terzaghi, K. Theoretical Soil Mechanics. New York, John Wiley and Sons, 1943.
7. Temoshenko, S. Theory of Elasticity. New York, McGraw-Hill, 1934.
8. Tschebotarioff, G. P. Soil Mechanics Foundations, and Earth Structures. New York, McGraw-Hill.
9. Westergaard, A. M. Soft Material Reinforced by Numerous Strong Horizontal Sheets. Contr. to Mechanics of Soils, Stephen Temoshenko 60th Ann. Vol, 1934.
10. Machado, J. Settlement of Structures in the City of Santos, Brazil. Proc. 5th Int. Conf. on Soil Mechanics and Foundation Eng., Vol. 1, 1961.

Appendix A

NOMENCLATURE

A = transmission factor,

B = existing overburden pressure before surface load is applied,

C = compression index of soil in flow chart,

E = void ratio in flow chart,

F = equivalent concentrated point load,

G = effective unit weight of soil,

K = sequential number for increment DZ,

M = total number of calculation points,

N = total number of point loads,

P = average unit contact pressure of point load,

R = horizontal radial distance between calculation point and loading point,

S = total settlement,

T = total pressure in soil after surface load is applied,

V = vertical pressure transmitted from surface load to a point in the soil,

X = distance of point load from Y axis,

Y = distance of point load from X axis,

Z = depth from contact surface to calculation point,

BS = overburden pressure at upper boundary of soil layer,

CB = constant equal to $12 \cdot \log_e / \log_{10}$ (5.211534 for inch system),
DS = increment of settlement for thickness DZ,
DV = increment of vertical pressure from a point load,
DZ = increment of thickness of soil layer,
HL = depth of lower boundary of soil layer for flow chart,
HU = depth of upper boundary of soil layer for flow chart,
KK = number of increments of thickness DZ,
LL = total number of soil layers under calculation point,
LM = number of data cards in which data is beyond significant settlement,
LN = sequential number for soil layers,
MM = sequential number for calculation points,
NN = subscript for point load data,
RCS = square of radius of equivalent circular loaded area,
RS = square of R,
XX = distance of calculation point from YY axis,
YY = distance of calculation point from XX axis,
C_c = compression index of soil,
H_u = upper boundary of soil layer,
H_ℓ = lower boundary of soil layer,
e = original void ratio of soil,
Δe = change of void ratio,
1 + e = total volume of soil,
r = horizontal distance between loading point and calculation point, and
ϵ = unit strain for layer dZ at depth Z below loaded area.

Appendix B

FORTRAN PROGRAM FOR IBM 1620 COMPUTER

```
      DIMENSION X(100), Y(100), P(100), F(100), R(100), RS(100)
      READ, DZ, N
      DO 2I=1,N
 2    READ, NN F(I), P(I), X(I), Y(I)
 3    READ, M
      DO 10 J=1,M
      READ, MM, XX, YY, B, LL
      DO 11 I=1,N
      RX=X(I)-XX
      RY=Y(I)-YY
```

```
      RS(I)=RX*RX+RY*RY
      R(I)=RS(I)**.5
11    CONTINUE
      DO 20 L=1,LL
      READ, LN,G,E,C,HA,HB
      CA=5.211534*C/(1.+E)
      KK=(HL-HU)/DZ
      Z=HA+.5*DZ
      B=BS+.5*G*DZ
      BS=BS+(HL-HU)*G
      DO 30 K-1,KK
      ZS=Z*Z
      V=0.0
      DO 40 I=1,N
      IF (R(I)-1.0) 41,41,42
42    RCS=F(I)/(P(I)*3.1416)
      DV=P(I)*(1./(1.+RCS/ZS))**1.5)
      V=V+DV
      GO TO 40
41    IF (R(I)-2.*Z)43,40,40
43    DP=.477*F(I)/(ZS*(1.+RS(I)/ZS)**2.5)
      V=V=+DV
40    CONTINUE
      IF (PV-.1*B) 13,31,31
31    DS=CA*LOG(1.+V/B)*DZ
      S=S+DS
      Z=Z+DZ
      B=B+G*DZ
30    CONTINUE
20    CONTINUE
12    PUNCH, MM,S,Z,V,B
10    CONTINUED
13    LM=LL-L
      IF (LM) 12,12
      DO 15 KN=1,KK
      READ, G,E,C,HA,HB
15    CONTINUE
      GO TO 12
      END
```

Appendix C

SAMPLE PROBLEM

The settlement of a building at Santos, Brazil, has been calculated using the program presented in Appendix B. The building has a total load of 9,514 tons carried on strip footings as shown in Figure 7. The footings were placed 8 ft below the surface and were designed for a soil pressure of 3 tons/sq ft. For convenience in calculating the stresses in the soil, an equivalent loading plan as shown in Figure 7 was devised. The loading data for this plan are listed in Table 3.

The strata below the foundations are shown in Figure 7. The water level is 3 ft below the ground surface. The average liquid limit for the clayey sand is 35 percent. From this information, we assume the needed data such as void ratio, effective unit weight and the compression index, as listed in Table 4.

The loading and soil properties were determined and placed in the computer. The settlements calculated are shown in Figure 8. Table 5 gives these settlements along with those actually measured at the building site.

TABLE 3

LOADING DATA

NN	X (ft)	Y (ft)	F (lb)	P(psf)
1	5	37	600000	6000
2	15	37	600000	6000
3	25	37	600000	6000
4	35	37	600000	6000
5	45	37	600000	6000
6	55	37	600000	6000
7	65	37	600000	6000
8	75	37	600000	6000
9	85	37	600000	6000
10	95	37	600000	6000
11	105	37	600000	6000
12	5	21	600000	6000
13	15	21	600000	6000
14	25	21	600000	6000
15	35	21	600000	6000
16	45	21	600000	6000
17	55	21	600000	6000
18	65	21	600000	6000
19	75	21	600000	6000
20	85	21	600000	6000
21	95	21	600000	6000
22	105	21	600000	6000
23	5	5	600000	6000
24	15	5	600000	6000
25	25	5	600000	6000
26	35	5	600000	6000
27	45	5	600000	6000
28	55	5	600000	6000
29	65	5	600000	6000
30	75	5	600000	6000
31	85	5	600000	6000
32	95	5	600000	6000
33	105	5	600000	6000

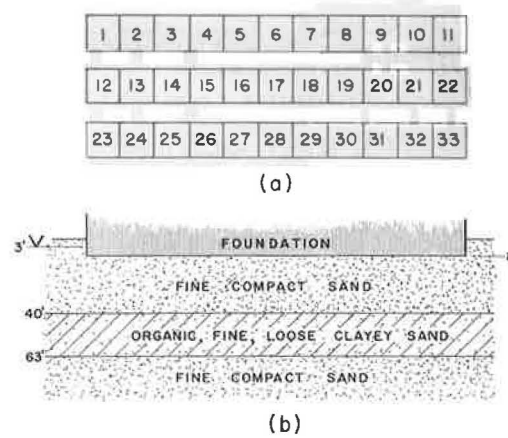

Figure 7. Sample problem: (a) assumed loading on soil, and (b) soil profile.

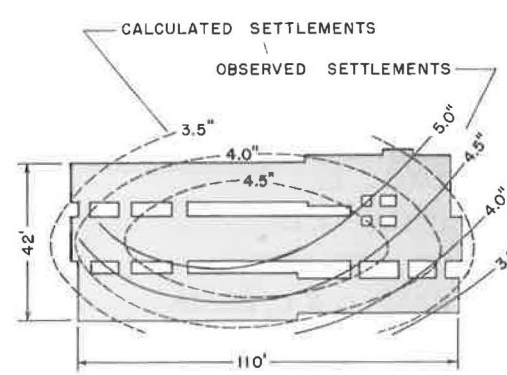

Figure 8. Plan of footings and settlements.

TABLE 4

SOIL DATA

MM	XX	YY	BS	LN	G	E	C	HU	HL
1	5	37	680	1	70	0.5	0.01	0	32
				2	25	1.5	0.16	32	55
2	15	37	680	1	70	0.5	0.01	0	32
				2	25	1.5	-.16	32	55
3	25	37	680	1	70	0.5	0.01	0	32
				2	25	1.5	0.16	32	55
4	35	37	680	1	70	0.5	0.01	0	32
				2	25	1.5	0.16	32	55
5	45	37	680	1	70	0.5	0.01	0	32
				2	25	1.5	0.16	32	55
6	55	37	680	1	70	0.5	0.01	0	32
				2	25	1.5	0.16	32	55
7	65	37	680	1	70	0.5	0.01	0	32
				2	25	1.5	0.16	32	55
8	75	37	680	1	70	0.5	0.01	0	32
				2	25	1.5	0.16	32	55
9	85	37	680	1	70	0.5	0.01	0	32
				2	25	1.5	0.16	32	55
10	95	37	680	1	70	0.5	0.01	0	32
				2	25	1.5	0.16	32	55
11	105	37	680	1	70	0.5	0.01	0	32
				2	25	1.5	0.16	32	55
12	5	21	680	1	70	0.5	0.01	0	32
				2	25	1.5	0.16	32	55
13	15	21	680	1	70	0.5	0.01	0	32
				2	25	1.5	0.16	32	55
14	25	21	680	1	70	0.5	0.01	0	32
				2	25	1.5	0.16	32	55
15	35	21	680	1	70	0.5	0.01	0	32
				2	25	1.5	0.16	32	55
16	45	21	680	1	70	0.5	0.01	0	32
				2	25	1.5	0.16	32	55
17	55	21	680	1	70	0.5	0.01	0	32
				2	25	1.5	0.16	32	55
18	65	21	680	1	70	0.5	0.01	0	32
				2	25	1.5	0.16	32	55
19	75	21	680	1	70	0.5	0.01	0	32
				2	25	1.5	0.16	32	55
20	85	21	680	1	70	0.5	0.01	0	32
				2	25	1.5	0.16	32	55
21	95	21	680	1	70	0.5	0.01	0	32
				2	25	1.5	0.16	32	55
22	105	21	680	1	70	0.5	0.01	0	32
				2	25	1.5	0.16	32	55
23	5	5	680	1	70	0.5	0.01	0	32
				2	25	1.5	0.16	32	55
24	15	5	680	1	70	0.5	0.01	0	32
				2	25	1.5	0.16	32	55
25	25	5	680	1	70	0.5	0.01	0	32
				2	25	1.5	0.16	32	55
26	35	5	680	1	70	0.5	0.01	0	32
				2	25	1.5	0.16	32	55
27	45	5	680	1	70	0.5	0.01	0	32
				2	25	1.5	0.16	32	55
28	55	5	680	1	70	0.5	0.01	0	32
				2	25	1.5	0.16	32	55
29	65	5	680	1	70	0.5	0.01	0	32
				2	25	1.5	0.16	32	55
30	75	5	680	1	70	0.5	0.01	0	32
				2	25	1.5	0.16	32	55
31	85	5	680	1	70	0.5	0.01	0	32
				2	25	1.5	0.16	32	55
32	95	5	680	1	70	0.5	0.01	0	32
				2	25	1.5	0.16	32	55
33	105	5	680	1	70	0.5	0.01	0	32
				2	25	1.5	0.16	32	55

TABLE 5

SETTLEMENT

Pt. No. MM	Calc. Set. (in.)	Pt. No. MM	Calc. Set. (in.)
1	3.344	18	5.133
2	3.947	19	5.029
3	4.302	20	4.813
4	4.500[a]	21	4.418
5	4.600	22	3.741
6	4.626	23	3.344
7	4.600	24	3.947
8	4.500	25	4.302
9	4.302	26	4.500
10	3.947	27	4.600
11	3.344	28	4.626
12	3.741	29	4.600
13	4.418	30	4.500
14	4.813	31	4.302
15	5.029	32	3.947
16	5.133	33	3.344[c]
17	5.164[b]		

[a]Observed settlement = 5.25 in.
[b]Observed settlement = 6.75 in.
[c]Observed settlement = 3.30 in.

Condition of Large Caissons During Construction

NAI C. YANG, Structural Design Engineer, The Port of New York Authority

The pier foundation consisted of a massive concrete caisson placed by open dredge method. The Brooklyn tower pier is embedded in glacial sand of the Wisconsin epoch and is founded 170 ft below sea level on silty clay of the Gardiner interval. Similar glacial sand is encountered at the Staten Island pier which founded at El. -105 ft on the transition of morainal deposit.

At any stage of sinking, the effective weight of the caissons should exceed the anticipated resistance which must be evaluated before the detailed planning. The present methods for determining such resistance, on the basis of soil tests or experience of individual engineers, are widely diversified.

During the sinking and buildup stages of both caissons, records were systematically compiled and tests were rationally analyzed. The bearing capacity of the silty clay at the cutting edge was determined to be 5.9 to 6.5 times shearing strength. The skin friction on the caisson is maximum at the very beginning of sinking and is reduced to a resistance equivalent to 45 percent of average overburden pressure. The lower range of skin friction would depend on the method and manner of applying water jets and compressed air.

•IMPORTANT FEATURES of New York City's Narrows Bridge have been described in an article published in the Engineering News Record (1). Among the many outstanding features of this longest suspension span are the tower foundations, which are of unprecedented dimension and depth of embedment in the ground. At the present stage of construction (August 1963), both pier foundations and steel towers have been completed and the spinning of the cables is in progress.

The pier foundation is actually of the most conventional type, consisting of concrete caisson with open wells for dredging. During the construction, the driving force for seating the caisson was gained by removing the supporting soils at the bottom. Therefore, at any stage of the sinking, the effective weight of a caisson should exceed the anticipated resistance, which consists of the skin friction on caisson surface as well as the bearing resistance of soils at the cutting edge. The theoretical methods for determining such resistance on the basis of soil tests are not often reliable and experiences of individual engineers are widely diversified. It is the purpose of this paper to review the actual mechanics of sinking a caisson.

SUBSOIL CONDITION

Geological Review (2)

The area is underlain by metamorphosed rocks of the pre-Cambrian age. Sediments of Cretaceous age are encountered above the basement rock. As the early continental glacier advanced toward the north shore of Long Island, outwash materials deposited great beds of gravel and clay (Jameco Stage) in the old Sound River Valley which was not too far from the Brooklyn pier. During the subsequent retreat (Sankaty Stage), the land was in a gradual uplift and the Sankaty sediments emerged about 50 ft above water.

With the return of the subsequent glacier, the older beds were overridden and folded. Gay Head outwash and Gardiner sediments were laid on the top of these folds. The area

Paper sponsored by Committee on Construction Practices—Structures.

continued its progressive subsidence throughout the third glacial epoch. At the Tisbury Stage, the land had subsided about 250 ft. Beds of gravel and boulders were deposited on the older sediments and extended over the entire Sound River Valley. During the long erosion period of the Vineyard interval, the present drainage pattern of the Hudson River was established. Fresh water sediments were accumulated at a rather slow pace, permitting the growth of organisms.

At the return of the last glacier, the Wisconsin, initial advancement did not reach the bridge site. Because of the rapid melting of the ice, the outwash plain is predominantly of sand and gravel. During the intermission of glacial advancement, the sea

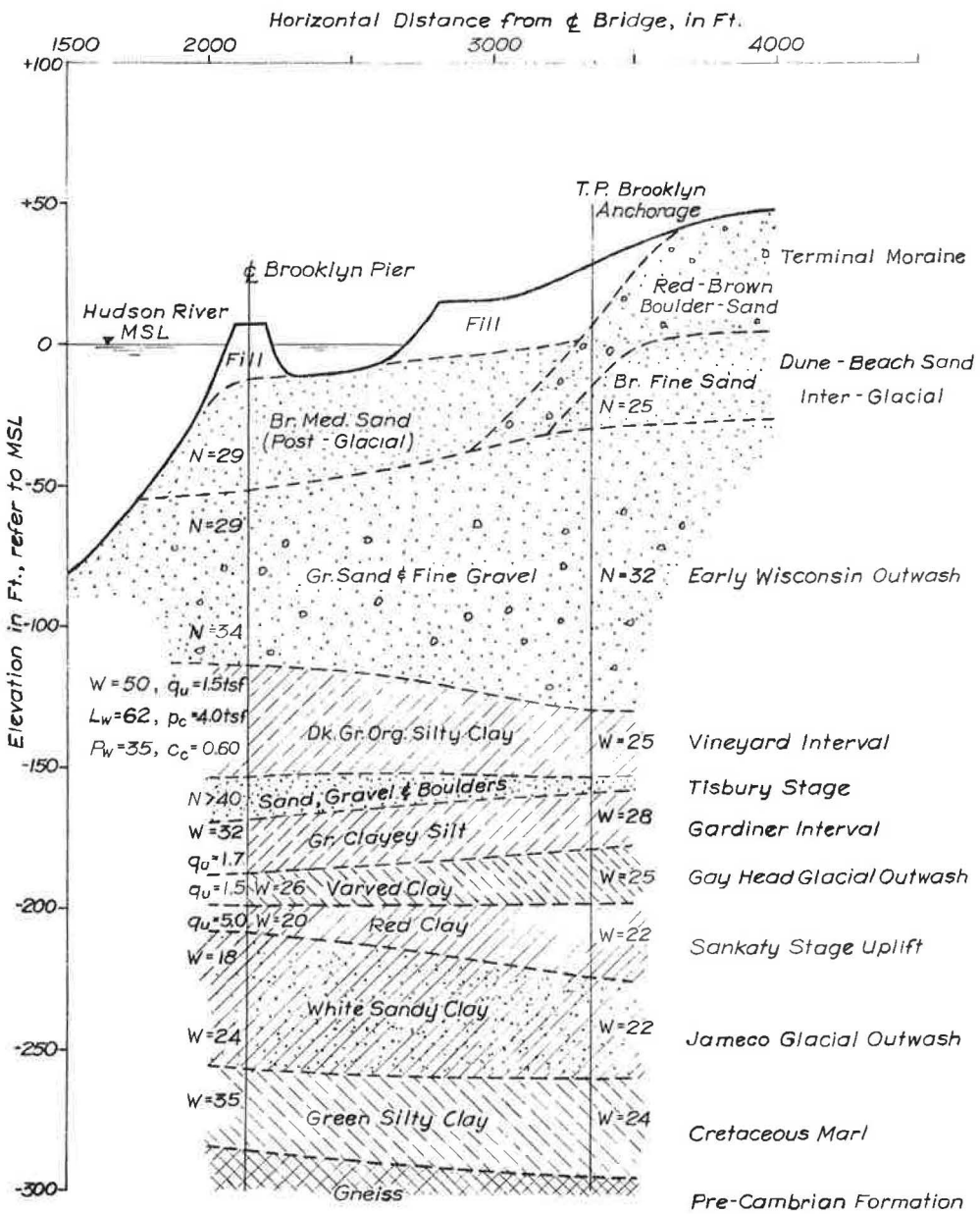

Figure 1. Soil profile of Brooklyn site—Narrows bridge.

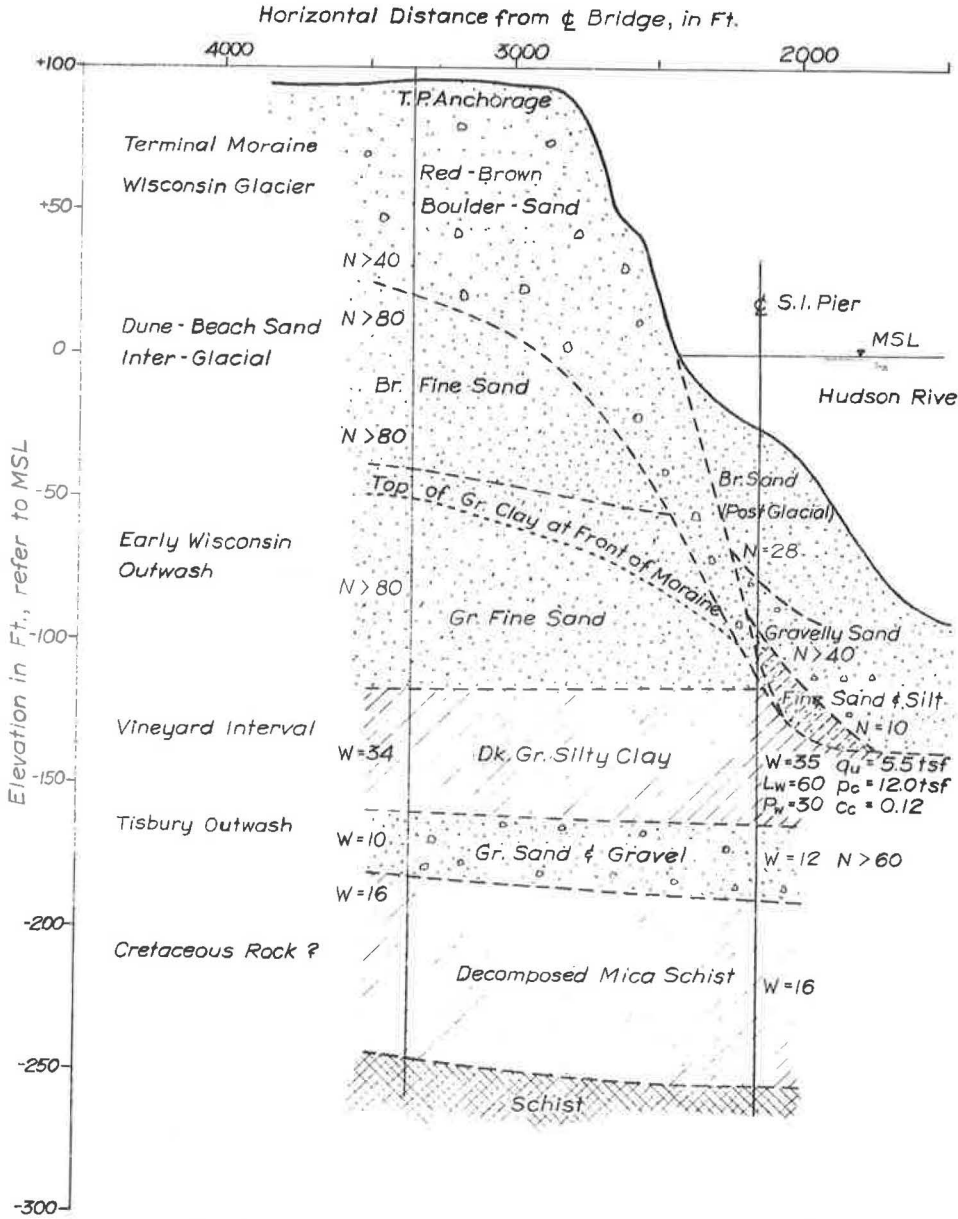

Figure 2. Soil profile at Staten Island site—Narrows bridge.

level was about 50 ft below the present level. The Hudson River cut through the outwash plain and sand dunes were formed along the beach. At the last movement of the Wisconsin glacier, the entire bridge site, except the Brooklyn pier, was covered by the ice. Terminal moraines formed the hilly topography along the present shoreline of the Narrows.

Since the retreat of the last glacier, there has been no significant sedimentation in the Hudson River, except the gradual fill-up of the deep channel following the rising of sea level. Soil profiles for the Brooklyn and Staten Island sites have been constructed and are shown in Figures 1 and 2, respectively.

Basement Rock

The basement rock at the Brooklyn pier is encountered at 290 ft below sea level and consists of gray gneiss. During the test pile operation, a NX-size diamond core was drilled 10 ft into the rock. Average drilling time was 7 min/ft and a solid piece 8.3 ft long was recovered. The uppermost several inches were slightly decayed. Overlying the gneiss is a layer about 1 ft thick of lime-cemented soft rock. At the Staten Island pier, weathered gneiss and schist were encountered in the borings. The rock surface is about 30 ft higher than that at Brooklyn pier.

Cretaceous Deposits

Green clay marl is encountered at the Brooklyn site. The average moisture content is 35 percent at the tower pier and 24 percent under the anchorage where the terminal moraine was located. The clay marl under the anchorage is likely to be precompressed by the weight of the glacier. At the Staten Island site, the formation of Cretaceous age is not clearly defined.

White Sandy Clay

It was a glacial filling of the Sound River Valley. The clay soil is possibly derived by the combined action of weathering and sedimentation. There are resemblances of residual soils. However, pockets of fine sand and patches of lignite are commonly pronounced in the deposit. The deposit is about 50 ft thick and is encountered at 210 ft below sea level. The uppermost part of the deposit is mottled with white, yellow and red, but the lower part is predominantly white. The unconfined compressive strength is estimated to be 4 to 6 tsf for the upper part of the deposit and 3 to 4 tsf for the lower one. Desiccation may have an important role in effecting the strength of this deposit.

Red Clay

It is a very sticky clay and was deposited during the gradual uplift of the coastal area. Although the red clay is only 5 to 10 ft thick, it represents the demarcation between the hard materials of older age and the subsequent deposits of moderate strength. The unconfined compressive strength ranges from 4 to 6 tsf and preconsolidation pressure is estimated from the consolidation tests to be 12 to 14 tsf. The compression index, C_c, is 0.10. The high strength of red clay is assumed to be caused by the internal consolidation pressure during desiccation.

Varved Clay

This deposit is encountered at 170 ft below sea level and extends 30 ft to the red clay layer. The sediments were brought down during the Gay Head and Gardiner Stages. The unconfined compressive strength ranges from 1.5 to 2.0 tsf. The preconsolidation pressure, according to the consolidation test, is estimated to be 4.5 to 5.0 tsf which is equivalent to the present overburden pressure. The compression index ranges from 0.20 to 0.30. It is a fairly compressible material.

Tisbury Sand

At the Tisbury Stage, glacial material appeared at the Staten Island site. The entire valley of the Sound River had been completely filled. The Tisbury formation is relatively thin, ranging from 5 to 10 ft at the Brooklyn site and 20 ft at the Staten Island site. Boulders are encountered in the deposit.

Organic Silty Clay

This deposit was brought down during the long recession (Vineyard Interval) of the continental glacier. The deposit is fairly thick, 40 ft at Brooklyn and 50 ft at Staten Island, as compared with the sediments of earlier glaciation. The Vineyard formation is a bay sediment of organic silt, having a liquid limit of 62 percent and plastic limit of 35 percent. At the Brooklyn pier, the natural water content is 50 percent, unconfined

compressive strength ranges from 1.0 to 1.6 tsf, and preconsolidation pressure is estimated to be 4.0 tsf which is equivalent to the present overburden pressure. The compression index is about 0.60. It is a very compressible soil. The preconsolidation pressure of the same soil formation under the Brooklyn anchorage and the Staten Island pier and anchorage foundations ranges from 10 to 16 tsf. The natural moisture content is 25 to 35 percent and the unconfined compressive strength is 5.0 to 6.5 tsf. Compression index is only 0.10. It is likely that this portion of the Vineyard formation has been precompressed by the weight of the glacier. It is interesting to note that in boring B-3 at the southeast corner of the Staten Island pier, where the front of the terminal moraine is encountered, the unconfined compressive strength of the silty clay decreases from 6.4 to 5.5 and 4.9 tsf, whereas the depth of the clay soil increases from El. -145 to -156 and -163 ft, respectively. The natural water content of the corresponding soil sample varies from 33 to 36 and 38 percent, respectively.

The Vineyard silty clay is a sensitive soil. The ratio of unconfined compressive strength between undisturbed samples and the completely remolded ones ranges from 3.5 at Staten Island to 5.0 at the Brooklyn.

Wisconsin Sand

The outwash of early Wisconsin glacier consists of medium sand and fine gravel. The average size of D_{10}, 10 percent finer, is 0.17 mm (No. 80 sieve), and the average uniformity of grain size, ratio between D_{60}/D_{10}, is 3.7. It is a very clean sand containing only 2 to 4 percent finer than No. 200 sieve.

Postglacial Sand

The postglacial sediments consist of brown medium sand having a standard penetration resistance of 25 to 35 blows and uniformity of grain size of 4 to 6, similar to that of Wisconsin sand. The deposits at the Staten Island pier, however, are complicated by the presence of the terminal moraine and the old erosion channel of the Hudson River. Fine sand and soft silt were encountered in the old channel.

Fill

On the site of the Brooklyn pier was a 140-year-old fort, Fort Lafayette. This island was built up by sand fill and riprap to an elevation about 10 ft above sea level.

Discrepancy of Boring Information

Conventional wash borings were taken in 1954 and 1957 to determine the foundation condition and the strength of subsoil. As a common practice, the penetration resistance, in terms of hammer blows on soil samples, was used as a guide in determining the relative density of sand. In Figure 3, the number of hammer blows, equivalent to the N-value of standard penetration tests, varied from 85 to 320 for the soils at El. -160 to -240 ft in boring C-2. There was some belief that the sand layers were so compact that no pile could possibly be driven through. At the subsequent test pile operation, a 30-in. O. D. open-end pipe was easily driven through at a resistance ranging from 3 to 8 blows/in. which was not considered hard driving. When borings were taken at a great depth, the sampling rods became very flexible and their weight heavy in comparison with the driving hammer. The energy of the hammer impact was absorbed by the vibration of the rods and high blow counts were, therefore, recorded.

The presence of pore-water pressure at the bottom of a boring hole, however, would cause a significant decrease of blow count at the sampling. In a saturated fine sand, the pore water tended to flow into the casing pipe as soon as the overburden was removed. The fine sand could become partially unstable. Consequently, a low blow count was registered in the boring record. For the final borings taken during the caisson construction, drilling mud was used to fill up the casing to reduce the negative pressure at the bottom of the boring hole. The blow counts for the mud holes were significantly different from the early wash borings. In Figure 4, the field count of hammer blows was plotted against the relative density of the same sand tested in the laboratory. The N-value of the mud borings are in closer agreement with those found by others (3, 4).

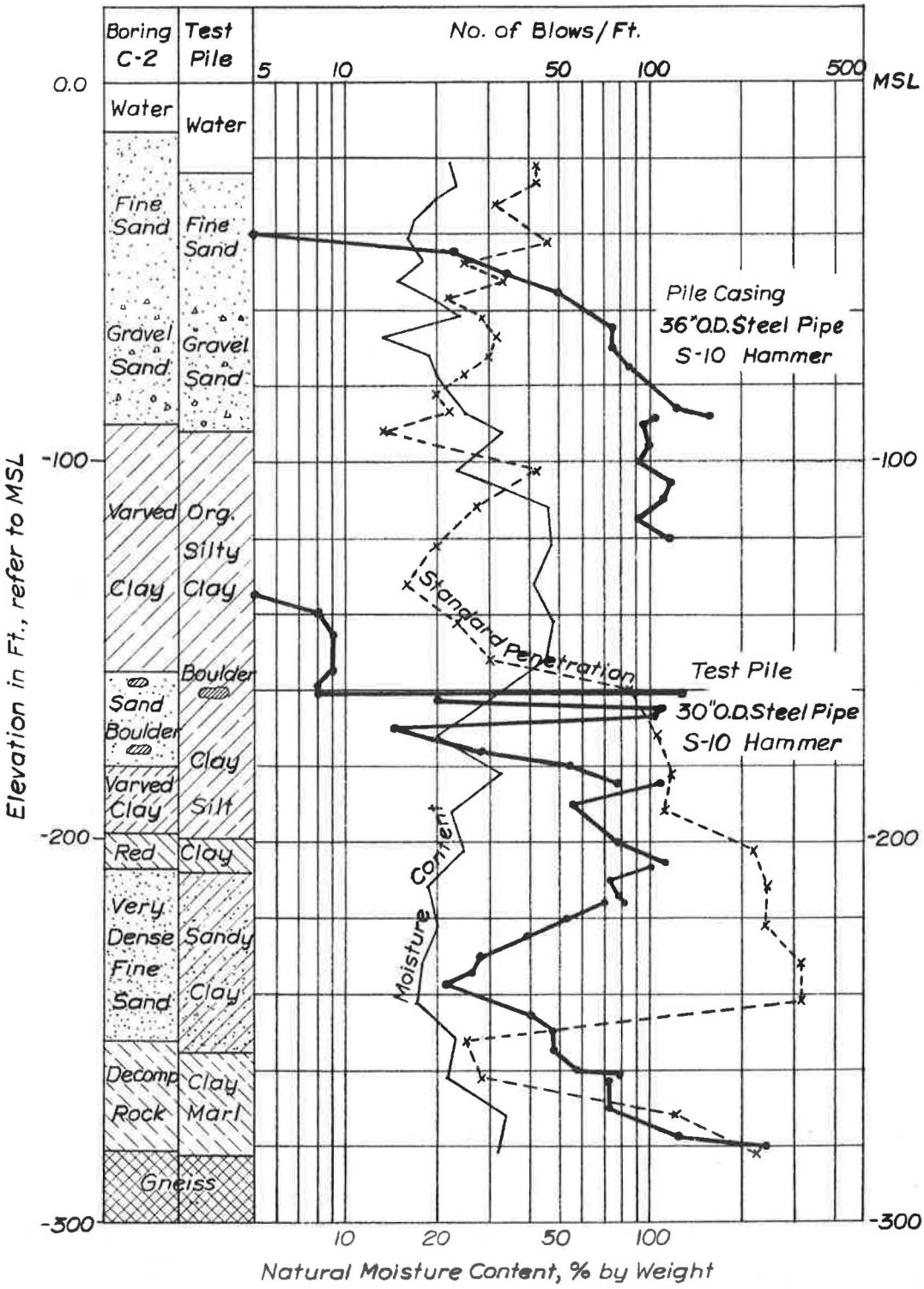

Figure 3. Comparison of pile driving and penetration resistance of boring.

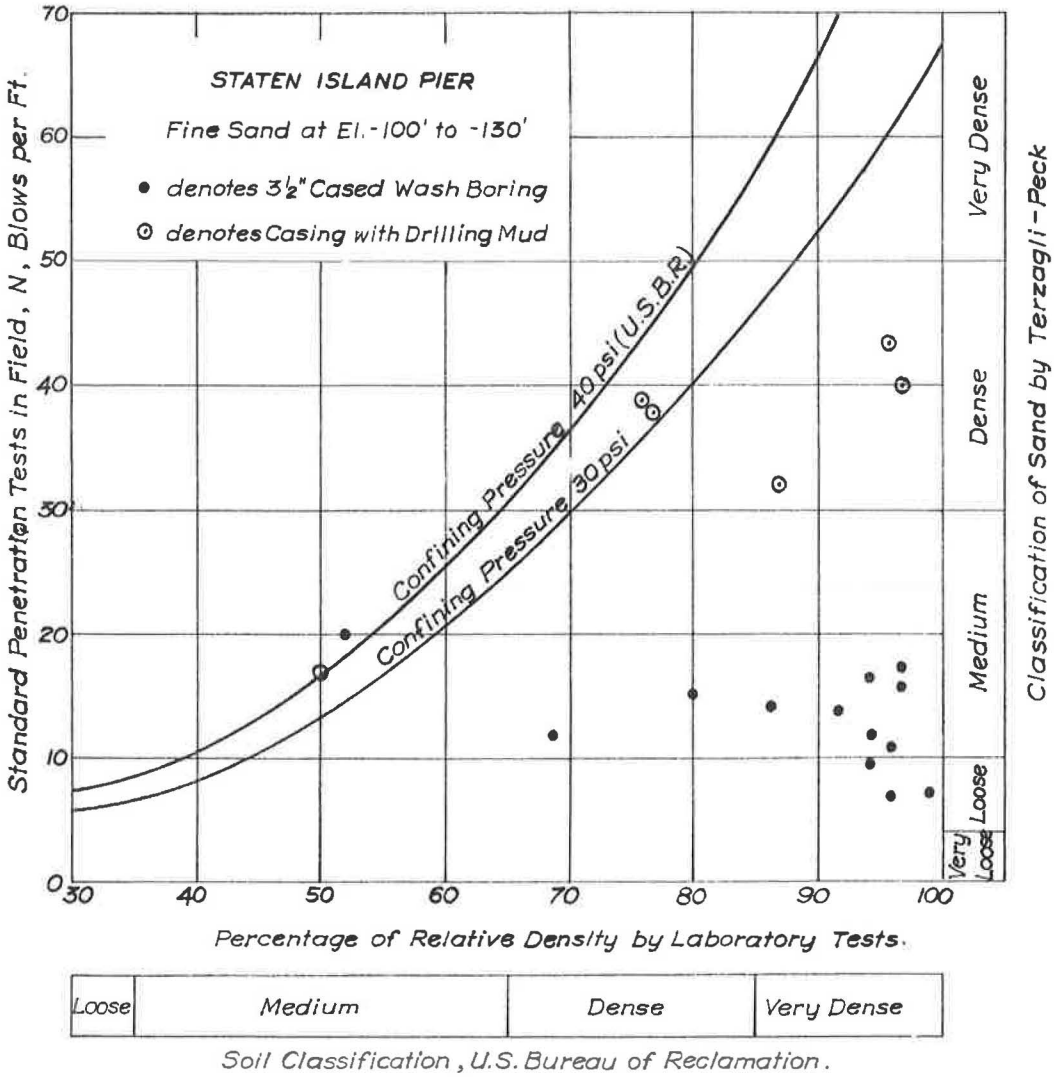

Figure 4. Relation between standard penetration and relative density.

CONSTRUCTION PROCEDURE

Sand Island

The average depth of water was 26 ft at the Staten Island pier and 20 ft at the north end of the Brooklyn pier. The sand island method was adopted for assembling the cutting edge of the caisson. The island consisted of a chain of cellular cofferdams erected around the caisson foundation. The cofferdams were filled with sand to El. +10 ft and the enclosed island to El. -12 ft. Sand fill was placed in water and no compaction was contemplated. Dewatering was done by open pumping, supplemented by a single-stage wellpoint system inside the cofferdam inclosure. A clay blanket was subsequently placed outside the cofferdam and the inclosed island was dewatered to El. -16 ft. The rate of pumping was about 5,000 gpm at the beginning and was reduced to 3,000 gpm after the installation of the clay blanket. The efficiency of the wellpoint system was not as great as described by Hoffman (5).

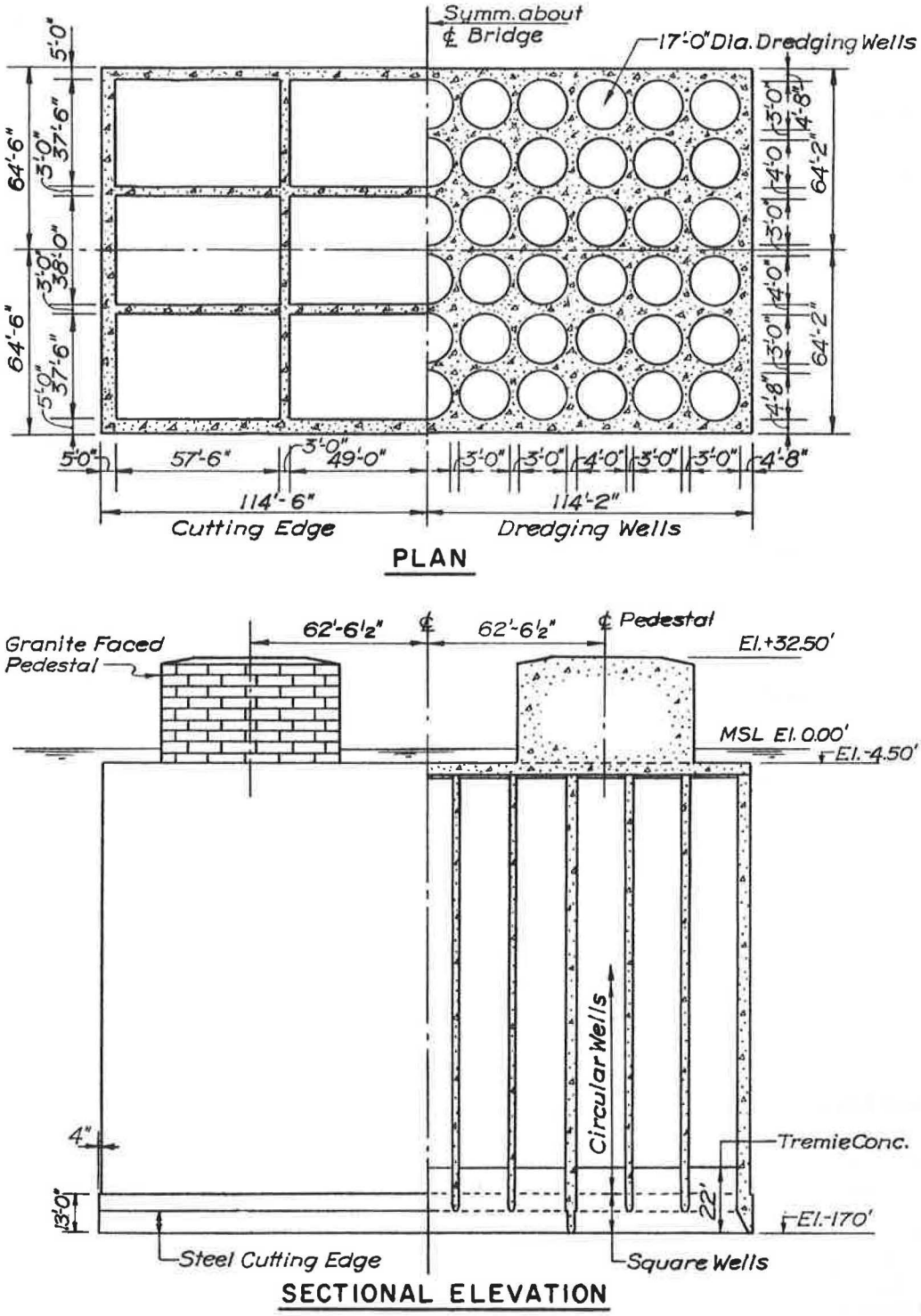

Figure 5. Detail of caisson structure—Brooklyn pier.

Cutting Edge

The steel cutting edge for both caissons consisted of a grid system of steel-plated boxes, 7 ft high and 3 ft wide for the interior walls and 5 ft wide for the peripheral walls. The purposes of the steel cutting edge were to provide a pointed edge during the sinking and to reinforce the caisson to withstand an excessive sagging stress at the early stage of construction. The steel cutting edge was assembled on timber ties. On its completion, the spaces between the walls were filled with sand. The entire assembling operation took about 5 wk. No significant settlement was observed during the period.

Caisson Buildup

The main body of the concrete caisson was progressively built up on the buried cutting edge. The overall dimension of the caisson was 129 by 229 ft, having 66 dredging wells, 17 ft in diameter (Fig. 5). Except for the first 13 ft and the final pour lift, the concrete caisson was poured in lifts of 10 ft and each lift was divided into four blocks with bulkheads at the narrowest parts of the caisson walls. Each stage of caisson buildup consisted of four lifts of concrete pour. The effective weight of the caisson was 37,000 tons at the end of the first stage buildup, and 42,000 tons were added at the completion of each subsequent stage of buildup. The first stage construction was completed in about 10 wk and the average buildup time was only 5 wk for the subsequent stages. During the caisson buildup, pouring sequence was properly controlled to avoid excessive eccentricity of the caisson weight. No significant differential settlement was observed at any stage of the concrete pours.

Open Dredge

The sinking of the caisson was accomplished by removing soil from the dredging wells. The digging was started from the center of the caisson and progressed toward the peripheral wells. The caisson tended to sag rather than to hog. The subsidence of the caisson was constantly measured by level with reference points on the cofferdam which were frequently adjusted with bench marks on shore. During the first stage of the sinking, the sagging stresses of the caisson were very critical. Vertical elevations of every intersection of dredge wells were constantly surveyed to check the stresses in the caisson walls.

REVIEW OF SINKING RECORD

Sinking of the caisson was a round-the-clock operation. Several sets of level readings were taken daily; the morning records were used in the analysis and are plotted on Figure 6. The sinking conditions of the Staten Island caisson were practically identical to those of the Brooklyn caisson; the sinking record of the latter is reviewed herein.

Rate of Sinking

The average daily rate of sinking was 2 ft for the first and second stages of sinking. The caisson could be driven as fast as the sand was removed from the dredging wells. The volume of daily excavation was about 2,500 cu yd in wet bucket measurement and the theoretical volume of caisson displacement was 2,200 cu yd. Cave-in of material was, therefore, insignificant. Where clay excavation was encountered below El. -105 ft, the efficiency of the dredging was considerably reduced because of the deep dredging and loss of material during lift-up. When lenses of fine sand and silt were encountered, additional material tended to flow into the dredging wells. Between El. -105 and -140 ft, the actual volume of caisson excavation was 1,400 cu yd/ft which was 27 percent more than the theoretical volume of caisson displacement. The average daily rate of sinking was about 1.2 ft (Fig. 7). Below El. -140 ft, the soil at the cutting edge became more silty and less able to withstand excessive pore-water pressure. Although positive waterhead was maintained inside the dredging wells to a height of 3 to 8 ft

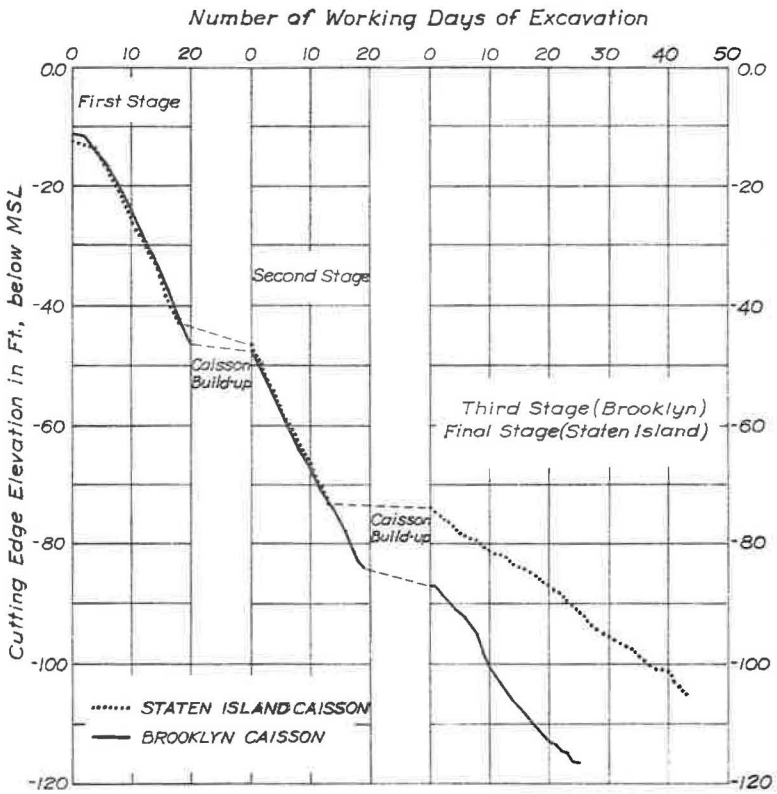

Figure 6. Daily sinking record of Brooklyn and Staten Island caissons.

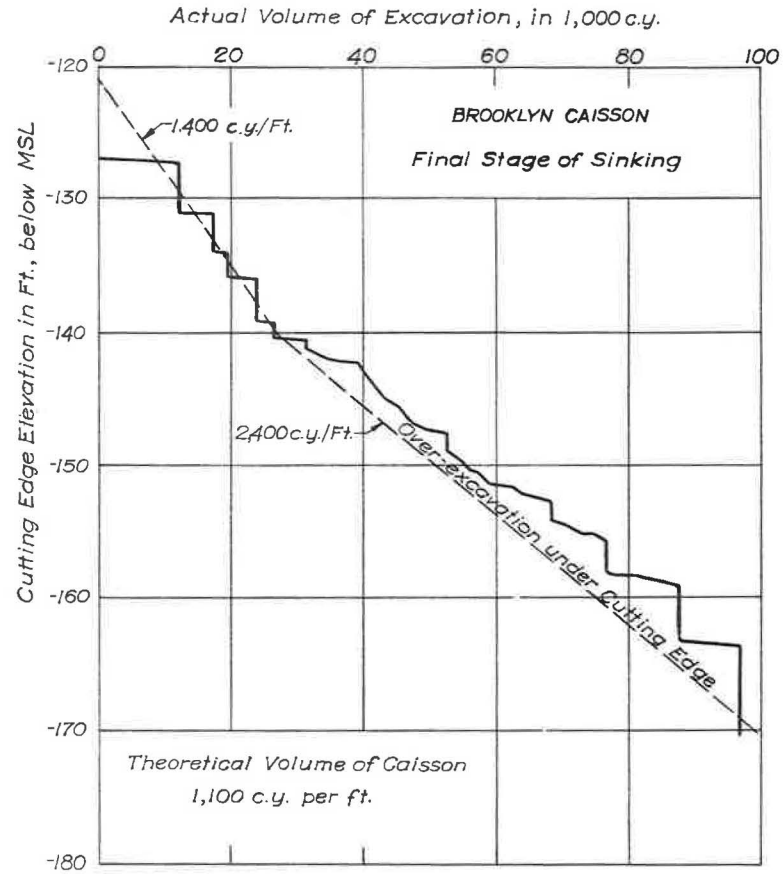

Figure 7. Mass diagram of sinking caisson.

above mean tide level, several cave-ins were noted. The magnitude of in-flows was also compounded by the undermining action below the cutting edge for reducing the sinking resistance. Between El. -140 and -170 ft, the actual volume of soil removed from the caisson was approximately 120 percent more than the theoretical caisson displacement. The average daily rate of sinking was 0.4 ft.

Resistance to Sinking

During the sinking process of a caisson, its downward movement is governed by the following factors: (a) effective weight of caisson, (b) bearing capacity of soil at cutting edge, (c) frictional resistance on caisson surface, (d) "freezing" action of soil, and (e) effectiveness of lubrication system. The first item represents the physical condition of caisson structure which can be readily determined. The last four items are closely related to the property of soils with which the caisson is in direct contact. At various sinking conditions, the contribution of each of the four factors is different and a diversified sinking resistance is therefore encountered (6, 7).

At the end of its third stage of sinking, the Brooklyn caisson had penetrated through 98 ft of sand and 15 ft of uniform clay in which the cutting edge was temporarily embedded. This was a favorable condition for studying the bearing capacity of the clay and the frictional resistance in the sand. This state of equilibrium is identified as Sequence 1 in the following discussion. At the subsequent caisson buildup, the relationship between the caisson settlement and the load increment due to the concrete pours was observed and is plotted in Figure 8. At the beginning of a new concrete pour, a certain amount of the weight was temporarily supported by the additional skin friction gained by "freezing." A new balance of soil resistance would be established until a rapid subsidence resulted. The states of equilibrium representing the conditions before and after the first rapid subsidence were identified as Sequences 2 and 3. Another rapid subsidence of the caisson was observed again at the later stage of buildup. The states of equilibrium representing the conditions before and after the second rapid subsidence were indicated as Sequences 4 and 5. During Sequences 1 through 5, there was no excavation in the caisson. The ultimate bearing capacity of the clay should not change appreciably except for a slight increase in confining pressure inside the dredging wells at Sequence 5.

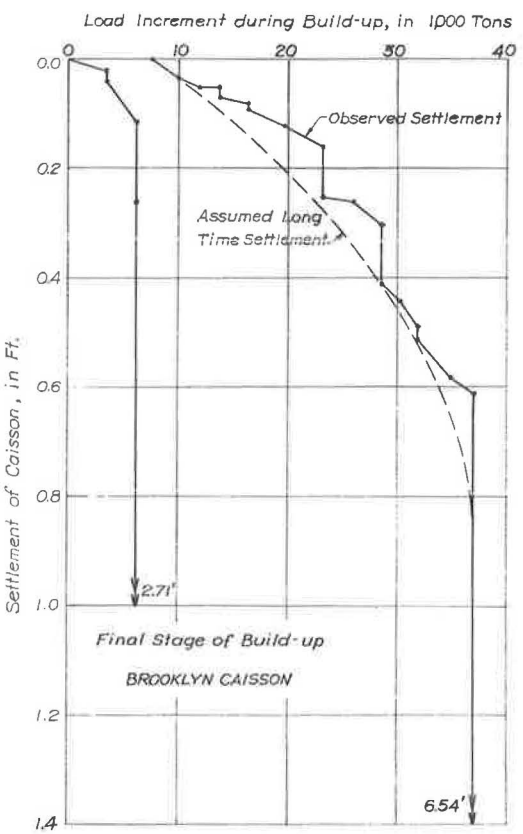

Figure 8. Settlement of caisson during final stage of buildup.

At the beginning of the final stage of sinking (Fig. 9), a rapid subsidence occurred when 14,000 cu yd of soil had been removed. The states of equilibrium were identified as Sequences 6 and 7 for the conditions at the beginning and the end of the rapid subsidence. The physical condition of these sequences is given in Table 1. The ultimate bearing capacity of a spread footing on clay can be expressed by:

$$qA = (cN_c + \gamma D_f)A \qquad (1)$$

in which c and γ are the shearing strength

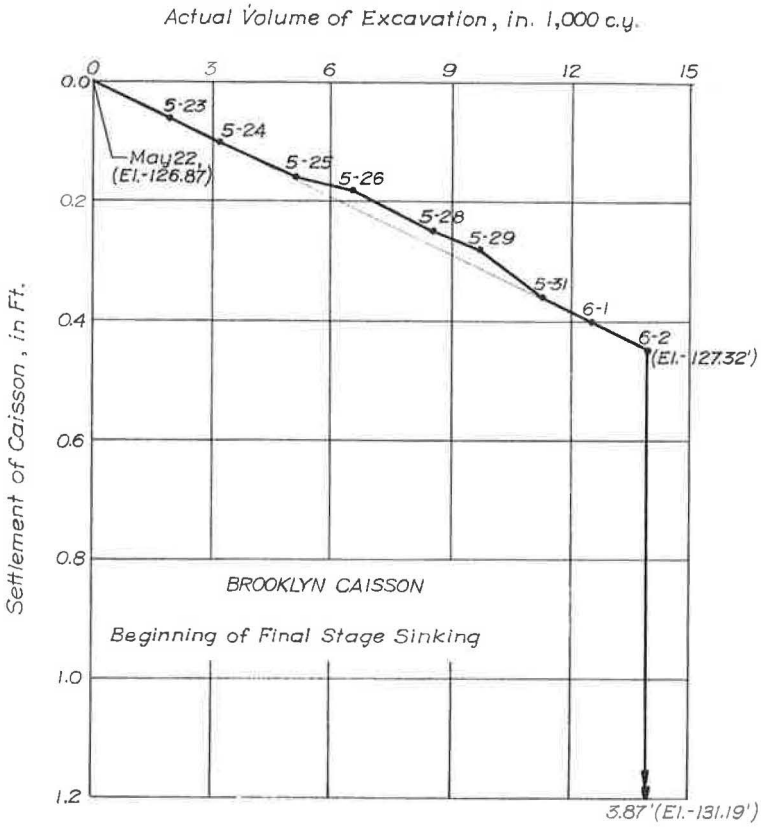

Figure 9. Settlement of caisson at beginning of sinking stage.

TABLE 1

CONDITION OF CAISSON DURING FINAL BUILDUP

Sequence	Cutting Edge Elev. (ft)	W (kips)	S (sq ft)	$\bar{P}_0$ (ksf)	A (sq ft)
1[a]	-116.64	155,220	77,460	3.79	2,010
2[b]	-116.90	168,580	77,640	3.80	2,100
3[b]	-119.61	166,210	79,570	3.88	3,010
4[c]	-120.27	229,170	80,040	3.91	3,230
5[c]	-126.81	223,450	84,710	4.12	6,640
6[d]	-127.35	227,640	85,020	4.13	4,170
7[d]	-131.19	224,210	87,800	4.26	5,470

[a]Condition on April 6 at end of third stage sinking.
[b]Taking place on April 18 at first rapid subsidence during the final buildup.
[c]Condition on May 17 at the second rapid subsidence.
[d]Initial subsidence on June 2 at beginning of final stage sinking.

and unit weight of clay soil, D_f is the depth of subcharge, A is the footing area, N_c is the bearing capacity factor of clay, and q is the unit bearing capacity. The depth of surcharge above the bottom of the cutting edge was 3 ft for Sequences 1, 2, and 7, 10 ft for Sequences 3 and 4, and 24 ft for Sequences 5 and 6. The value of γD_f is not significant in Eq. 1. Slight variations in the depth of surcharge have no appreciable effect on the analysis of the ultimate bearing capacity.

The skin friction on the caisson surface is developed when the caisson movement is sufficient to develop the shear strength of the surrounding soil mass. The intensity of the skin friction is proportional to the frictional coefficient of soil and the normal stress on the vertical surface of the caisson wall. The normal stress, in this case, is equivalent to the horizontal earth pressure. The total skin friction on the caisson surface can be expressed by the term $SK\bar{P}_o \tan\delta$, in which S is the embedded area of the caisson surface, δ is the angle of wall friction, $\bar{P}_o$ is the average overburden pressure, and K is the coefficient of earth pressure during the sinking of the caisson. As the effective weight of the caisson, W, is supported by the resistances of soil, condition of equilibrium is given by

$$W = qA + SK\bar{P}_o \tan\delta \tag{2}$$

In Table 1, the values of W, A, S and $\bar{P}_o$ were compiled for Sequences 1 through 7. The relation between q and K $\tan\delta$, in accordance with Eq. 2, is shown graphically in Figure 10.

At Sequences 1, 3, 5 and 7, the shearing strength of soil was sufficiently mobilized to resist the rapid subsidence of the caisson. The "freezing" action of the soil did not prevail. There was no lubrication system used before Sequence 7. Both Sequences 1 and 7

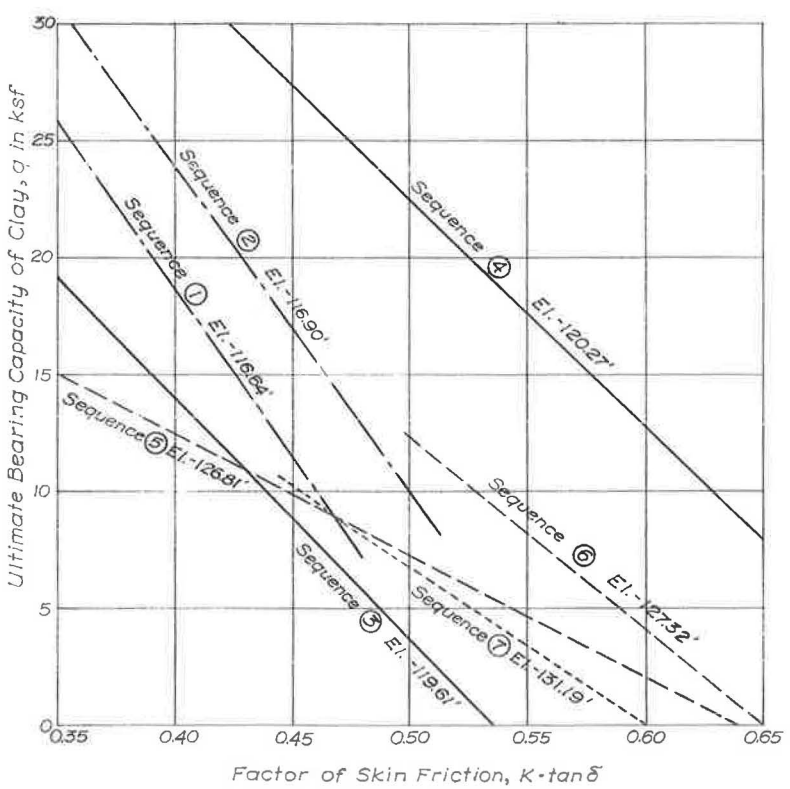

Figure 10. Graphic presentation on equilibrium of sinking caisson.

represented the condition of equilibrium immediately following a rapid subsidence. By equating the equilibrium condition for Sequences 1 and 7, it was possible to use the graphical method (Fig. 10) to determine that the unit bearing capacity would be 9.1 ksf. The corresponding bearing capacity factor of clay, N_c, would be 5.9 after adjusting the term γD_f and assuming the shearing strength of clay to be one-half of its unconfined compressive strength which had an average value of 1.5 tsf. A similar analysis would give the unit bearing capacity of 11.1 ksf and the N_c value of 6.5 for Sequences 3 and 5, another pair of identical equilibrium conditions. The theoretical values of N_c, according to Terzaghi and Peck (6), are 5.7 for continuous footing and 7.4 for individual ones. These are in close agreement with the values obtained here.

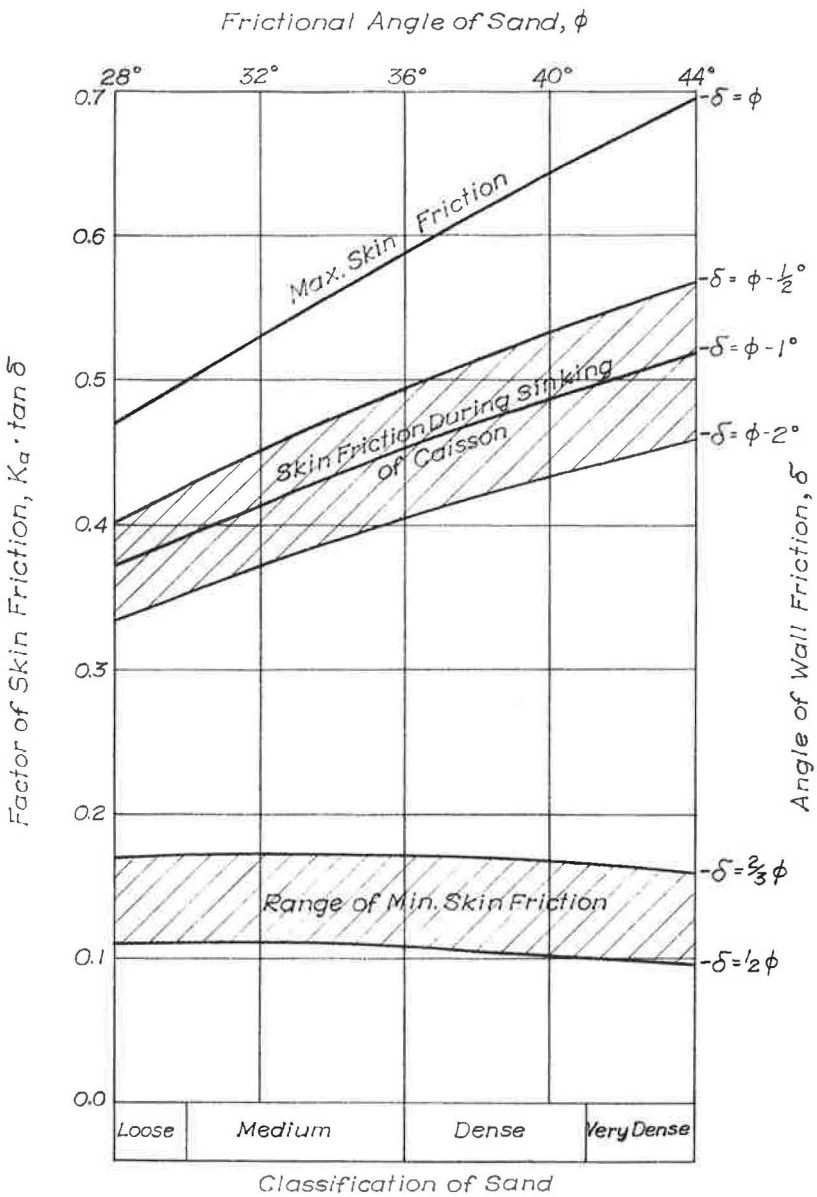

Figure 11. Variation of sinking resistance to change of wall friction.

The factor of skin friction, K tanδ, as given by the equation of equilibrium was 0.466 for Sequences 1 and 7 and 0.430 for Sequences 3 and 5. By assuming the angle of wall friction to be the same as the frictional angle of soil, estimated to be 36° for a 30-blow sand (4), the K-value would range from 0.59 to 0.64. During the sinking of a caisson, the normal stress on its vertical surface was much smaller than the overburden pressure. The sand tended to expand along its sliding surface. The increase of void ratio of sand at lower confining pressure is known in soil engineering as dilatancy. A dense sand could expand 2 or 3 percent by volume which is equivalent to a reduction of frictional angle of 1° or 2°.

In analyzing the relative movement at sinking a caisson, the surrounding soil can be considered to move upward along the caisson. The angle of wall friction would be a negative value in the general earth pressure equation derived by Coulomb (8). In Figure 11, the theoretical factor of skin friction has been computed, assuming that every part of the contacted soil mass is on the verge of failure and the normal stress on the vertical caisson surface is equivalent to the value given by Coulomb's active earth pressure. It is noted that the factor of skin friction would be reduced more than 20 percent from its maximum value when the angle of wall friction is only 1° less than the angle of soil friction. The dilatancy of sand would have a significant effect on the sinking of the caisson during Sequences 1, 3, 5 and 7.

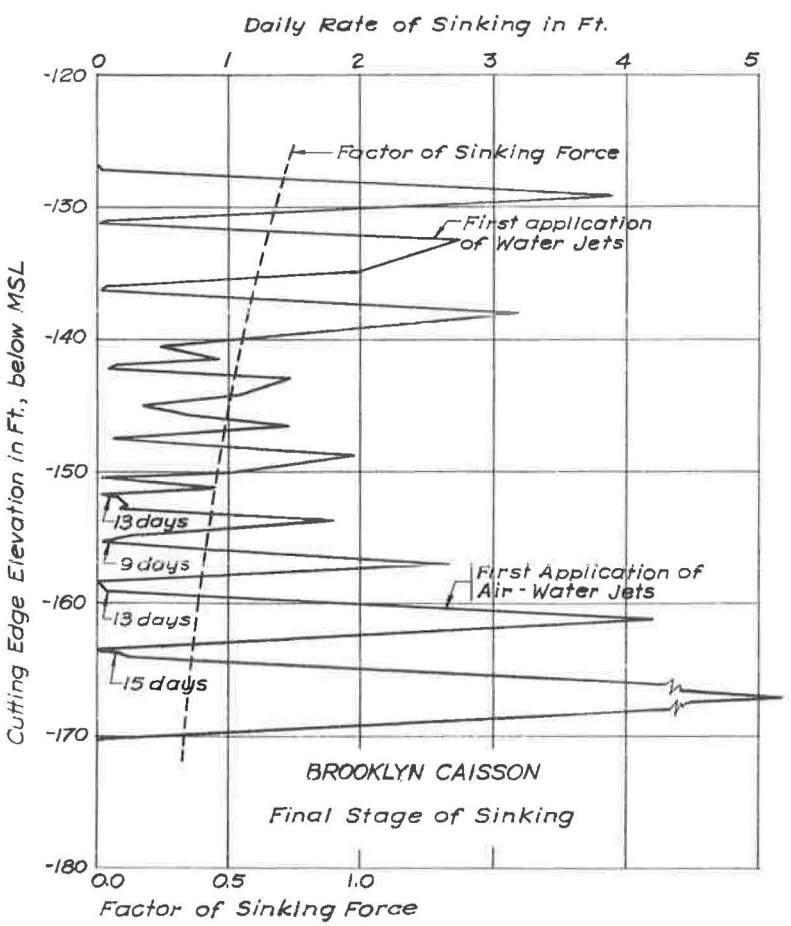

Figure 12. Rate of sinking and efficiency of lubrication.

Efficiency of Lubrication

During the sinking operation, the daily rate of subsidence was compared with the factor of sinking force, assumed to be the effective weight of the caisson per unit area of skin surface divided by the average overburden pressure. The relationship between the daily rate of sinking and the factor of sinking force was plotted on Figure 12. When the factor of sinking force was 0.65, the caisson would not move under its own weight. Water jets were introduced in the 2-in. pipe nozzles, spaced 12 to 15 ft apart and installed in the lower part of the peripheral walls. The excessive water tended to cause the expansion of sand and to reduce the skin friction. As the surface of the caisson represented the least resistance and the shortest passage for the water stream, the effect of the water jetting was confined to the surface of sliding. At cutting edge elevation of -158 ft, the bottom of the caisson was undermined to a depth more than 8 ft below the cutting edge and the factor of sinking force was 0.40. The caisson failed to subside under the influence of water jettings. A combination of air and water jetting was adopted for improving the sinking condition. The compressed air introduced into the same jetting system tended to expand and cause the breakdown of the original soil structure. In some instances, air bubbles were traced about 100 ft away from the nozzle where the compressed air was applied. Prolonged air jetting was avoided to prevent any secondary effect on the foundation. Due to the fast expansion of the compressed air, the breaking strength of the surrounding soil would be equivalent to the value of the consolidated quick shear tests which ranges from one-half to two-thirds of that of the slow shear tests. By assuming the angle of wall friction to be of the same value as that for the quick shear tests, the theoretical factor of skin friction ranges from 0.10 to 0.17 (Fig. 11). Handman (9) has observed that the actual factor of skin friction ranged from 0.12 to 0.14.

Effect of Freezing

"Freezing," in a strict sense, is not a proper engineering term. It is commonly used by field engineers to identify the condition when the resistance to driving a pile increases significantly after its installation. As observed on driving of piles (10), the increase of resistance is related to the adjustment of pore-water pressure and the thixotropic effect of fine-grained soils. The magnitude of freezing increases with increasing degree of disturbance at the pile installation and, to a lesser extent, with the duration after construction. No significant freezing effect has been observed for piles driven in soils coarser than fine sand. As the subsoil through which the caisson was installed consisted predominantly of medium sand and fine gravel, there would be no appreciable time lag of adjusting pore-water pressure. Moreover, the clay soil at the cutting edge was not disturbed and the freezing action would be negligible. However, as shown in Figure 10, the factor of skin friction for Sequences 2, 4 and 6 was appreciably higher than that for Sequences 1, 3 and 5 if the ultimate bearing capacity of clay was considered a constant. There were also indications that the skin friction increased at a rate of 1.09, 1.18 and 1.43 when the intermission between rapid subsidences was 12, 16 and 29 days, respectively (Table 1, Fig. 10).

When the movement of the caisson was temporarily ceased after the rapid subsidence at Sequences 1, 3 and 5, the sand along the caisson surface underwent a new process of reconsolidation. If sufficient time was available, the sand regained its original shearing strength. At the very beginning of the new subsidence, the angle of wall friction was of the same magnitude as the frictional angle of the soil mass. The frictional resistance against sinking of the caisson was maximum. According to Coulomb's active earth pressure, the theoretical factor of skin friction ranges from 0.60 to 0.65 for driving a caisson through dense sand. The actual sinking record of the Brooklyn caisson indicated a similar range of sinking force, i.e., from 0.65 to 0.70 at the beginning of sinking (Fig. 12). The slightly higher factor of sinking force was caused by the presence of a very small bearing support at the cutting edge.

CONCLUSIONS

1. The observed bearing capacity factor of normally loaded clay at the cutting edge is in close agreement with the theoretical value given by Terzaghi and Peck.
2. The skin friction on the caisson can be expressed by Coulomb's active earth pressure.
3. The effective weight of the caisson should always exceed the anticipated sinking resistance without the excessive use of a lubricating system. A factor of skin friction of 0.40 should be considered the practical minimum, if a built-in jetting system is installed to overcome any excessive skin friction.

ACKNOWLEDGMENT

The bridge project is under the sponsorship and administration of the Triborough Bridge and Tunnel Authority. The work described herein was carried out between 1954 and 1961 under the general direction of Captain Emil H. Praeger, who was retained as a consultant on foundation design by O. H. Ammann of Ammann-Whitney, the principal engineer for the design and supervision of the entire bridge project. The writer wishes to extend his appreciation to John Kenny and Earl Larson for their cooperation during the caisson construction.

REFERENCES

1. Everything About the Narrows Bridge is Big, Bigger or Biggest. Eng. News-Record, June 29, 1961.
2. Veatch, A. C. Outline of the Geology of Long Island Sound. U. S. Geological Survey, Prof. Paper No. 44, 1906.
3. Earth Manual. p. 314. U. S. Bureau of Reclamation, 1960.
4. Peck, Hanson, and Thronburn. Foundation Engineering. p. 222. New York, John Wiley and Sons, 1953.
5. Hoffman, J. F. Wellpoints Dewater Sites for Narrows Bridge Piers. Civil Eng., Vol. 30, No. 10, pp. 71-73, 1960.
6. Terzaghi and Peck. Soil Mechanics in Engineering Practice. pp. 167, 172, 489-490. New York, John Wiley and Sons, 1948.
7. Henry, F. D. C. The Design and Construction of Engineering Foundation. pp. 323-335. New York, McGraw-Hill, 1956.
8. Tschebotarioff, G. P. Soil Mechanics, Foundations and Earth Structures. pp. 242-252. New York, McGraw-Hill, 1951.
9. Handman, F. W. A. The Lower Zambezi Bridge. Jour. Inst. Civil Eng., Vol. 4, pp. 342-347, 1936-1937.
10. Yang, Nai-Chen. Redriving Characteristics of Piles. Proc. ASCE, Vol. 82, No. 1026, 1956.